Charge Transfer Dynamics in Perovskites Crystals-Graphene Heterostructures for Light-harvesting Applications

A Dissertation Submitted to the Department of Chemistry, Quaid-i-Azam University, Islamabad, Pakistan, in the Partial Fulfilment of the Requirements for the Degree of Doctor of Philosophy

in

Chemistry

by

Maria Mukhtar

Department of Chemistry,

Quaid-i-Azam University,

Islamabad, Pakistan

2024


بسم الله الرحمن الرحيم

Declaration

I **Maria Mukhtar**, Ph.D. scholar in the Department of Chemistry, Quaid-i-Azam University, Islamabad, Pakistan, hereby solemnly declare that my Ph.D. dissertation titled "**Charge transfer dynamics in perovskites crystals-graphene heterostructures for light-harvesting applications**" is the research work that I have performed under the supervision of Professor Dr. Azhar Iqbal and previously has not been submitted for any other degree or professional qualification except as specified, from Quaid-i-Azam University, Islamabad or anywhere else.

Signature: _____

Date: _____

Dedicated to my loving parents, siblings, family, friends, and my honorable teachers

Acknowledgements

All praises to Allah, the Almighty, who is the Lord of immense universe, on whom we depend for sustenance and guidance. All respect for His last Prophet Hazrat Muhammad (Sallallaho Alaihe Wa-alehe Wasallam), who gave my conscience the essence of belief in Allah and His last messenger.

It is a genuine pleasure to express my deep sense of thanks and gratitude to my mentor, philosopher and guider, Prof. Dr. Azhar Iqbal. His dedication, keen interest and above all his overwhelming attitude to help his students had been solely and mainly responsible for completing my work. His timely advice, meticulous scrutiny, scholarly advice, and scientific approach have helped me to accomplish my PhD studies. I owe a deep sense of gratitude to Prof. Dr. Zareen Akhtar (The Chairperson of Chemistry Department) and Dr. Hazrat Hussain (Head of the Physical Section). I expand my thanks to all the staff of the Chemistry Department for their assistance and kindness. I am highly thankful for financial support of Higher Education Commission (HEC) Pakistan through the research grants6976/Federal/NRPU/R&D/HEC/2017 and 20-3071/NRPU/R&D/HEC/13. I acknowledge Turkish Burslari Fellowship of The Scientific and Technological Research Council of Turkey for conducting a part of PhD research in Solar energy institute of Ege University. I would also like to show my genuine appreciation to Prof. Dr. Sule Erten Ela and Cagdas Yavuz for lending me a helping hand whenever needed. I am grateful to HEC, Pakistan for providing me financial support under International Research Support Initiative Program (IRSIP) to proceed for a part of my PhD research in University of Bath, UK. A special thanks to Prof. Petra group for providing me friendly, healthy, caring and helping lab environment. I would also like to thanks my Phd colleagues, M. Mubeen Butt, Adnan khalid, Poshmal Sumreen and Mamoona Tabassum and M.phil lab mates for their support and positive input, especially whose cheerful attitude gave me lots of encouragement. Many thanks to Kaya Davies and Mathew Pilot for guiding me about solar devices. I am also thankful to prof. Frank Markin and Anwar Ul Hamide for assisting in analysis. I am sincerely thankful to my beloved parents, Mukhtar Hussain and Naseem Akhter (Late) without their cooperation I would not have been able to achieve anything. I would also like to appreciate the efforts of my family members, my friends, my teachers, and all others who support me in any way.

Maria Mukhtar

Table of Contents

List of Figures ..... **vi**

List of Tables ..... **x**

List of Abbreviations ..... **xi**

List of Publications from this Thesis ..... **xiii**

Abstract ..... **xiv**

1. Introduction **1**

1.1 Graphene **1**

1.1.1 Derivatives of graphene 2

1.1.2 Synthesis of Graphene-Based Nanomaterials 3

1.1.2.1 Mechanical exfoliation by graphite *3*

1.1.2.2 Epitaxial Growth from Thermal Deposition of SiC *4*

1.1.2.3 Chemical vapor deposition (CVD) *4*

1.1.2.4 Solution-Based Exfoliation from Graphite Oxide and Graphite *4*

1.1.2.5 Bottom-Up Organic Synthesis Methods *5*

1.1.3 Electronic and Optical Properties of Graphene-Based Nanomaterials 6

1.1.3.1 Electronic Properties *6*

1.1.3.2 Optical properties *7*

1.1.4 Optical and optoelectronic applications of graphene-based nanomaterials ..7

1.1.4.1 Transparent conductive electrodes *8*

1.1.4.2 Phototransistor and photodetector *8*

1.1.4.3 Photovoltaic and Light Emitting Devices *9*

1.1.4.4 Saturable absorber for ultrafast lasers *9*

1.1.4.5 Photocatalytic applications *10*

1.2 Perovskites **11**

1.2.1 Synthesis methods of perovskites NCs 12

1.2.1.1 Solvothermal synthesis *12*

1.2.1.2 Colloidal synthesis *13*

1.2.1.3 Hot injection synthesis *13*

1.2.1.4 Microwave-assisted synthesis *13*

1.2.1.5 Gas-phase synthesis *13*

1.2.2 Optical and optoelectronic properties of perovskites NCs 13

1.2.2.1 Tunable Bandgap: *13*
1.2.2.2 High Absorption Coefficient *13*
1.2.2.3 High Quantum Yield *14*
1.2.2.4 Long Carrier Lifetime *14*
1.2.2.5 High Stability *14*
1.2.3 Applications of perovskites NCs 14
1.2.4 Photovoltaics applications of perovskites NCs 15
1.3 Heterojunction/Heterostructure and Charge Transfer 17
1.4 Carbon based perovskites solar cells 18
1.5 Photoelectrochemical water splitting 19
1.6 Review Literature 20
1.7 Aims and Objectives of the present work 23
2. Experimental 24
2.1 Materials and Methods used 24
2.1.1 Chemicals and reagent 24
2.1.2 Synthesis of $CsPbBr_3$ NCs 25
2.1.3 Preparation of graphene (Gr) 25
2.1.4 Preparation of functionalize graphene 26
2.1.5 Preparation of $CsPbBr_3$ NCs/Alanine functionalized graphene (N-Gr) heterostructures 26
2.1.6 Synthesis of formamidinium lead bromide ($FAPbBr_3$) NCs 27
2.1.7 Preparation of $FAPbBr_3$ NCs/Graphene (Gr) heterostructures 27
2.1.8 Formation of $FAPbBr_3$ NCs/Functionalized graphene heterostructures 27
2.1.9 Preparation of solar cells containing $FAPbBr_3$ perovskites as light absorber and commercial carbon paste 28
2.2 Characterization Methods 29
2.2.1 Powder X-ray Diffraction 29
2.2.2 Fourier transform infrared spectra (FTIR) 29
2.2.3 X-ray photoelectron spectroscopy (XPS) 29
2.2.4 Scanning Electron Microscope (SEM) 29
2.2.5 Transmission Electron Microscopic (TEM) coupled with EDS 29
2.2.6 UV-Vis Spectroscopy 29
2.2.7 Photoluminescence (PL) Measurements 29

2.2.8 Band edges estimation 30
2.2.9 J-V measurements of the solar devices 30
2.2.10 Electrochemical Measurements for water splitting 30
2.2.11 Electrochemical Impedance Spectroscopy (EIS)……..….31

3. Results and Discussion 32

3.1 Photon-induced Electron Transfer in Ligand Stabilized Monoclinic $CsPbBr_3$ and Alanine Functionalized Graphene Heterostructures 32

3.1.1 Characterization of functionalized graphene 33
3.1.1.1 Powder XRD analysis of graphene oxide (GO) and alanine functionalized graphene (N-Gr) 33
3.1.1.2 FTIR analysis of GO and alanine functionalized graphene (N-Gr) 33
3.1.1.3 UV-Vis spectroscopy 34
3.1.1.4 Raman analysis of GO and N-Gr 35
3.1.2 Characterization of $CsPbBr_3$ NCs 36
3.1.2.1 Structural, morphological, and chemical analysis of the NCs 36
3.1.2.2 UV-Vis absorption and PL analysis of NCs 42
3.1.2.3 PL decay kinetics analysis of NCs 44
3.1.3 PL quenching studies of NCs/N-Gr heterostructures 47
3.1.4 Cyclic voltametric (CV) analysis of NCs and N-Gr 50
3.1.5 Summary 54

3.2 Photoexcited Electron Transfer in Hydrophobic Fluorescent $FAPbBr_3$ Perovskite Nanocrystals and Graphene Heterostructures 55

3.2.1 Crystal structure and morphological analysis of $FAPbBr_3$ NCs 56
3.2.2 Characterization of Graphene oxide (GO) and Graphene (Gr) 57
3.2.2.1 Fourier-Transform Infrared (FTIR) analysis of GO and Gr 57
3.2.2.2 Powder X-ray Diffraction (XRD) Analysis of GO and Gr 58
3.2.2.3 Raman Analysis of GO and Gr 58
3.2.3 Characterization of $FAPbBr_3$/Gr heterostructures 60
3.2.3.1 FTIR analysis of $FAPbBr_3$ NCs and $FAPbBr_3$/Gr heterostructures 60
3.2.3.2 Powder XRD, TEM and HRTEM analysis of $FAPbBr_3$/Gr heterostructures 61
3.2.4 PL quenching and CT dynamics in $FAPbBr_3$ NCs/Gr heterostructures 63
3.2.5 Electrochemical measurements 67

3.2.6 Summary 71

3.3 Tuning the Charge Transfer Efficiency by Functionalizing Ligands in $FAPbBr_3$ Nanocrystals and Graphene Heterostructures 72

3.3.1 Characterization of functionalized graphene 73

3.3.1.1 SEM and EDX analysis of functionalized graphene 74

3.3.1.2 XRD analysis of functionalized graphene 76

3.3.1.3 FTIR analysis of functionalized graphene 77

3.3.1.4 Raman analysis of functionalized graphene 78

3.3.1.5 UV-Vis analysis of functionalized graphene 79

3.3.2 Characterization of $FAPbBr_3$ NCs/functionalized graphene heterostructures….. 80

3.3.2.1 TEM and HRTEM analysis of NCs/functionalized graphene heterostructures 80

3.3.2.2 XRD analysis of NCs/functionalized graphene heterostructures 82

3.3.2.3 FTIR analysis of NCs/functionalized graphene heterostructures ... 82

3.3.3 Fluorescence quenching of $FAPbBr_3$ NCs by functionalized graphene 83

3.3.4 Electrochemical Measurements 87

3.3.5 Summary 90

3.4 Low temperature processed $FAPbBr_3$ perovskites based solar devices and their water splitting application 91

3.4.1 Characterization of $FAPbBr_3$ perovskites based solar device 92

3.4.2 Photoelectrochemical water oxidation studies 98

3.4.3 Summary 102

4. Conclusion 103

5. Recommendations/Future perspective 104

6. References 105

List of Figures

Figure 1.1 Schematic demonstration of graphene as mother of different kinds of carbon-based materials. 1

Figure 1.2 Derivatives of graphene. 3

Figure 1.3 Synthesis methods for graphene-based nanomaterials. A) Mechanical exfoliation from graphite by tape against SiO_2 /Si substrate. B) High vacuum decomposition from atomic terraces on SiC wafer. C) Chemical vapor decomposition of gas or solid carbon source. 6

Figure 1.4 A. Graphene-based nanomaterials in optical and optoelectronic applications. The dynamic combination of unique structure and electronic/optical properties of graphene have encouraged many new optical and optoelectronic possibilities. B. transparent electrodes, C. Phototransistors, E, Photovoltaic device D. Biological sensors F. Ultrafast laser based on graphene saturable absorber g. Photocatalysis. 11

Figure 1.5 Perovskite crystalline structure ABX_3. 12

Figure 1.6 Applications of perovskites NCs. 15

Figure 1.7 Properties of perovskites making it a suitable candidate for photovoltaic. 16

Figure 1.8 Schematic representation of charge transfer across type I, type II, and type III heterostructure formed by combining of two semiconductor materials. 18

Figure 1.9 Device architecture of carbon-based perovskites solar cells. 19

Figure 2.1 0.1 mg/ml dispersion of GO, GO-Ala, GO-Tyr, and GO-Cys in toluene...28

Figure 3.1.1 (a) XRD pattern, (b) FTIR, (c) UV-Vis absorption and (d) Raman spectra of GO and N-Gr. 35

Figure 3.1.2 (a) XRD pattern, (b-c) SEM micrographs and (d) High-resolution TEM micrograph of 0.5 mM MAA capped $CsPbBr_3$ NCs (inset showing the SAED pattern of NCs). 37

Figure 3.1.3 (a) XRD patterns, (b) FTIR spectra (c) EDX spectrum of 0.5 mM MAA functionalized $CsPbBr_3$ NCs. 38

Figure 3.1.4 XPS analysis (a) Survey spectrum of $CsPbBr_3$ NCs, (b) Cs 3d spectrum, (c) Br 3d spectrum, (d) Pb 4f spectrum, (e) S 2p spectrum and (f) O 1s spectrum. Solid red lines indicate the experimental data and black filled circles represent the best fits. 41

Figure 3.1.5 Absorption and normalized PL spectra of $CsPbBr_3$ NCs synthesized using various conc. of MAA.....43
Figure 3.1.6 Absorption and normalized PL spectrum and (b) Tauc plot of $CsPbBr_3$ NCs without MAA. 43
Figure 3.1.7 Schematic representation displaying the decrease in the particle size with increase in amount of MAA capping ligand (b) Tauc plot (c) PL decay kinetics of $CsPbBr_3$ NCs containing various MAA concentrations.....46
Figure 3.1.8 PL spectra of $CsPbBr_3$ NCs (0.5 mM MAA) and $CsPbBr_3$ NCs/N-Gr heterostructures in toluene solvent containing various amounts of N-Gr, inset. Stern-Volmer plot, (b) UV-Vis absorption spectrum of N-Gr in water (black line) and PL spectrum of NCs in toluene.....48
Figure 3.1.9 PL spectrum of N-Gr.....48
Figure 3.1.10 (a-b) PL and decay kinetics spectra of $CsPbBr_3$ NCs (0.5 mM MAA) and $CsPbBr_3$ NCs/N-Gr heterostructures (c-d) PL and decay kinetics spectra of $CsPbBr_3$ and $CsPbBr_3$/Gr heterostructures.....50
Figure 3.1.11 (a) CVs of NCs (b) Tauc plot of N-Gr (c) ln α vs. hv plot of N-Gr (d) CVs of N-Gr in 50 mM $TBAPF_6$ in toluene: acetonitrile (4:1) solution.....51
Figure 3.1.12 (a) Band edges of N-Gr and estimated by CV And (b) schematic diagram showing the anchoring of MAA functionalized $CsPbBr_3$ NCs with N-Gr matrix through different terminal functional groups of N-Gr, because of which the phenomenon of charge transfer takes place.....53
Figure 3.2.1 (a) XRD pattern, (b) TEM micrograph with inset bars graph displaying the size distribution, (c) High-resolution TEM image and (d) SAED pattern of $FAPbBr_3$ NCs.....57
Figure 3.2.2 (a) FTIR spectra of GO and Gr and (b) XRD patterns of GO and Gr (c) Raman spectra of GO and Gr. 59
Figure 3.2.3 FTIR spectra of $FAPbBr_3$ NCs and $FAPbBr_3$ NCs/Gr heterostructure..60
Figure 3.2.4 (a). Powder XRD patterns of $FAPbBr_3$ NCs and NCs/Gr heterostructure, (b) TEM and (c) HRTEM images of the $FAPbBr_3$ NCs/Gr heterostructure. 62
Figure 3.2.5 (a) UV-Vis absorption and PL spectra of 1 g/L solution of $FAPbBr_3$ NCs, (b) UV-Vis absorption spectra of 1 g/L solution of $FAPbBr_3$ NCs and $FAPbBr_3$ NCs/Gr heterostructures in toluene solvent with different amount of Gr, (c) PL spectra of $FAPbBr_3$ NCs and $FAPbBr_3$ NCs/Gr heterostructures in toluene solvent containing

different amounts of Gr, and (d) PL spectrum of NCs in toluene solvent and UV-Vis absorption spectrum of Gr in water. *64*
Figure 3.2.6 Steady state PL spectrum of Gr. *65*
Figure 3.2.7 Stern-Volmer plot, (b) PL kinetics of 1 g/L solution of $FAPbBr_3$ NCs and $FAPbBr_3$ NCs/Gr heterostructures in toluene solvent with different amounts of Gr. *67*
Figure 3.2.8 (a) Tauc plot of Gr. (b) Tauc plot of $FAPbBr_3$ NCs. (d) CV of Gr. (e) CV of $FAPbBr_3$ NCs with supporting electrolyte of $TBAPF_6$ (50 mM) in toluene:acetonitrile (4:1) solution. *69*
Figure 3.2.9 (a). ln α vs. hν plot of Gr, (b) Electrochemical Impedance spectroscopy (EIS) analysis of $FAPbBr_3$ NCs and $FAPbBr_3$ NCs/Gr heterostructures. *70*
Figure 3.2.10 (a) Diagrammatic representation of band edges of NCs and Gr, (b) Schematic representation of CT dynamics in $FAPbBr_3$ NCs/Gr heterostructures. *71*
Figure 3.3.1 Schematic of surface decoration of Alanine, Tyrosine, and Cysteine (amino acid) on GO. *73*
Figure 3.3.2 (a-d) SEM micrographs of surface decorated graphene (a) GO, (b) GO-Tyr, (c) GO-Ala, and GO-Cys. *75*
Figure 3.3.3 (a) XRD patterns of surface decorated graphene, i.e., GO, GO-Tyr, GO-Ala, and GO-Cys. (b): FTIR spectra of GO, GO-Ala, GO-Tyr, and GO-Cys. *77*
Figure 3.3.4 (a) Raman and (b) UV-Vis absorption spectra of GO, GO-Tyr, GO-Ala, and GO-Cys. *79*
Figure 3.3.5 TEM and HRTEM images of the (a, b) $FAPbBr_3$ NCs/GO, (c, d) $FAPbBr_3$ NCs/GO-Ala, (e, f) $FAPbBr_3$ NCs/GO-Cys, and (g, h) $FAPbBr_3$ NCs/GO-Tyr heterostructures. *81*
Figure 3.3.6 (a) Powder XRD patterns of $FAPbBr_3$ NCs and NCs/functionalized graphene (NCs/GO, NCs/ GO-Ala, NCs/GO-Tyr, and NCs/GO-Cys) heterostructures, (b) FTIR spectra of $FAPbBr_3$ NCs and NCs/functionalized graphene (GO, GO-Ala, GO-Cys, and GO-Tyr) heterostructures. *83*
Figure 3.3.7 (a) PL spectra and (b) PL decay kinetics of $FAPbBr_3$ NCs and $FAPbBr_3$ NCs/functionalized graphene (GO, GO-Ala, GO-Tyr, GO-Cys) heterostructures, (c) PL spectra of GO, GO-Cys, GO-Ala, and GO-Tyr indicating the non-emissive nature of these compounds, (d) PL spectrum of $FAPbBr_3$ NCs in toluene solvent and UV-Vis absorption spectra of GO, GO-Cys, GO-Ala, and GO-Tyr in water. *84*
Figure 3.3.8 (a) PL spectra of different amino acids (a) Alanine, (b) Cysteine, and (c) Tyrosine in the solution of $FAPbBr_3$ NCs in toluene, (d) Different amino acids (Alanine,

Cysteine, and Tyrosine) in the solution of NCs in toluene, d(a) Before stirring and d(b) After a stirring of half an hour.....85
Figure 3.3.9 CV of $FAPbBr_3$ NCs with supporting electrolyte of $TBAPF_6$ (50 mM) in toluene:acetonitrile (4:1) solution. 88
Figure 3.3.10 (a) CV of GO, (b) GO-Tyr, (c) GO-Cys, and (d) GO-Ala with supporting electrolyte of $TBAPF_6$ (50 mM) in toluene:acetonitrile (4:1) solution.....88
Figure 3.3.11 (a-d) Band edges estimation of $FAPbBr_3$ NCs and functionalized graphene, i.e., GO GO-Cys, GO-Ala, and GO-Tyr) by cyclic voltammetry analysis..89
Figure 3.4.1 (a) XRD patterns of the FTO/TiO_2, $PbBr_2$, and $FAPbBr_3$ film grown on FTO/TiO_2/$PbBr_2$ substrate, The FTO/TiO_2 peaks are shown by diamond marker. 92
Figure 3.4.2 (a-d) SEM micrographs of $FAPbBr_3$ grown on FTO/TiO2 substrate at different resolution.....93
Figure 3.4.3 Cross sectional SEM micrographs of $FAPbBr_3$ based carbon device, (a) from center, and (b) from edge of device.....93
Figure 3.4.4 (a) J-V curve and (b) IPCE curves of perovskite device.....95
Figure 3.4.5 (a) Absorption spectrum and (b) Tauc plot of $FAPbBr_3$ film.....97
Figure 3.4.6 (a) PL spectra and (b) Decay kinetics of $FAPbBr_3$ film, TiO_2/$FAPbBr_3$ and TiO_2/$FAPbBr_3$/carbon.....98
Figure 3.4.7 (a) LSV of the photoanode in dark and light at 50 mV/s (b) LSV of photoanaode in light with and without catalyst attached to the GS-160 at 50 mV/s (c) CV of the photoanodein dark and light at 50 mV/s. (d) Chronoamperometry measurements of photoanodes from 0 to 1.4 V with reference to RHE. (The voltage was successively increased 0.2 V every 5 minutes).....100
Figure 3.4.8 (a) EQE of the (a) TiO_2/$FAPbBr_3$/m-carbon in solar device configuration, and TiO_2/$FAPbBr_3$/m-carbon/GS-160 in three electrode configurations in 0.1 $MKNO_3$ at 2.5 pH. (b) TiO_2/$FAPbBr_3$/m-carbon/GS-160 in three electrode configurations in 0.1 $MKNO_3$ at 2.5 pH at various applied voltages Vs. Ag/AgCl. 101
Figure 3.4.9 (a) red trace, Chronoamperometry measurement of photoanode TiO_2/$FApbBr_3$/m-carbon/GS-160/Ir-WOC recorded at an applied potential of 1.23 V Vs. RHE in 0.1 M KNO_3 at pH 2.5 under 1 sun solar irradiation (AM 1.5G, 100 $mWcm^{-2}$), blue trace, Chronoamperometry measurements to detect O_2 production. (The nitrogen is purged for up to 20 minutes to remove the O_2 signal coming from air after that the O_2 produced inside system is detected), and (b) Moles of oxygen generated because of water oxidation, calculated by using the Faraday's law of electrolysis..102

List of Tables

Table 2.1 List of chemicals/reagent/materials used. 24

Table 3.1.1 Observed vibrational modes in GO and N-Gr.....34

Table 3.1.2 Percentage of elements observed in EDX and XPS analysis.....42

Table 3.1.3 Optical properties of MAA functionalized $CsPbBr_3$ perovskites NCs. 44

Table 3.1.4 The PL decay kinetics parameters of $CsPbBr_3$ NCs. 46

Table 3.2.1 The FTIR analysis of Gr and GO.....58

Table 3.2.2 The PL decay parameters of $FAPbBr_3$ NCs and $FAPbBr_3$ NCs/Gr heterostructures with their respective k_{CT} values. 67

Table 3.3.1 EDX analysis and percentage elemental composition of functionalized graphene. 75

Table 3.3.2 Observed vibrational modes in functionalized graphene. 78

Table 3.3.3 The PL decay parameters and respective k_{CT} and E_{CT} 87

Table 3.4.1 Device characterization parameters of solar devices.....95

Table 3.4.2 A comparison of devices reported in literature with the present fabricated device. 96

List of Abbreviations

Abbreviation	Description
Ala	Alanine
Cys	Cysteine
CB	Conduction band
CT	Charge transfer
CV	Cyclic voltammetry
EDX	Energy-dispersive X-ray
FTIR	Fourier-transfer infrared
FWHM	Full width at half maximum
Gr	Graphene
GO	Graphene oxide
GO-Ala	Alanine functionalized graphene oxide
GO-Cys	Cysteine modified graphene oxide
GO-Tyr	Tyrosine modified graphene oxide
HOMO	Highest occupied molecular orbital
HRTEM	High resolution transmission electron microscopy
JCPDS	Joint committee of powder diffraction standards
K_{SV}	Stern-Volmer's constant
K_{CT}	Rate of charge transfer
LUMO	Lowest un-occupied molecular orbital
MAA	Mercapto acetic acid
NCs	Nanocrystals
PL	Photoluminescence
QDs	Quantum dots
PLQY	Photoluminescence Quantum yield
PXRD	Powder x-ray diffraction
SEM	Scanning electron microscopy
SSPL	Steady-state photoluminescence
TCSPC	Time-correlated single-photon counting
TEM	Transmission electron microscopy
TRPL	Time-resolved photoluminescence
Tyr	Tyrosine

UV	Ultraviolet
VB	Valence band
XRD	X-ray diffraction

List of Publications from this Thesis

1. **Mukhtar, M**., Bibi, S., Ela, S.E., Yavuz, C., Mubeen, M., Sumreen, P., Khalid, M.A., Ul-Hamid, A. and Iqbal, A*., Photon-induced electron transfer in ligand-stabilized monoclinic $CsPbBr_3$ and alanine-functionalized graphene heterostructures. *The Journal of Physical Chemistry C*, 126 (**2022**) 15298. **(IF=4.177)**
2. **Mukhtar, M**., Mubeen, M., Ul-Hamid, A., Ela, S.E. and Iqbal, A.***,** Tuning charge transfer efficiency by functionalizing ligands in $FAPbBr_3$ nanocrystals and graphene heterostructures. *Physical Chemistry Chemical Physics* 25 (**2023**) 17410. **(IF=3.676)**
3. **Mukhtar, M**., Mubeen, M., Khalid, M.A., Sumreen, P., Ul-Hamid, A. Ela, S.E., and Iqbal, A.*, Photoexcited electron transfer in hydrophobic fluorescent $FAPbBr_3$ perovskite nanocrystals and graphene heterostructures. *Journal of Materials Research* (**2023**) DOI: 10.1557/s43578-023-01255-8. **(IF=3.00)**
4. **Mukhtar, M**., Iqbal, A.*, Cameron, P.*, Low temperature processed $FAPbBr_3$ perovskites based solar devices and their water splitting applications. **(***Manuscript in preparation***)**.

Abstract

In the field of catalysis, optoelectronics, and energy applications heterostructures of halide perovskites and graphene are developing as favorable materials. In these heterojunctions it is significant to get insight about the understanding that governs the charge transfer dynamics between the participant of heterojunction because it directly influences the output of the optoelectronic devices. In this work, the heterojunction of halide perovskites crystals with un-functionalized and functionalized graphene are described. For this purpose, mercaptoacetic acid (MAA) functionalized $CsPbBr_3$ nanocrystals (NCs), $FAPbBr_3$ NCs, bare graphene, and amino acids (Alanine, Tyrosine and Cysteine) functionalized graphene are synthesized. In the heterostructure of mercaptoacetic acid (MAA) functionalized $CsPbBr_3$ NCs and alanine functionalized graphene, the surface functionalization supports an efficient attachment of the NCs with the graphene. The use of MAA as functionalizing ligand not only passivates the surface of NCs, but it also presents the possibility of band gap tuning of NCs and further coupling with the alanine functionalized graphene. By combining the alanine functionalized graphene, the photoluminescence (PL) quenching of the NCs has been observed. The PL quenching occurs because of the photoexcited electron transfer from the $CsPbBr_3$ NCs to the alanine functionalized graphene via type I band alignment.

In the heterostructures of $FAPbBr_3$ NCs and graphene, PL quenching of $FAPbBr_3$ NCs with successive addition of graphene is observed. The electron transfer from NCs to graphene takes place because of formation of type-I band alignment between them. In the heterostructures of $FAPbBr_3$ NCs and amino acid functionalized graphene, the comparative effect of different functional group moieties on charge transfer dynamics is investigated. These studies suggest that the PL quenching ability is strongly dependent on the functional group and extent of charge transfer from perovskite NCs to graphene and can greatly be improved by choosing a suitable quencher for NCs. The hole and electron accepting ability of graphene can also be tuned by varying the type of the surface moieties of the graphene. The perovskites forms type II band alignment with functionalize graphene, as a result the hole transfer takes place from perovskites to functionalize graphene. Such heterostructures possessing facile charge transfer could make efficient commercial antenna systems for solar cells and optoelectronic devices. Lastly, the fluorine doped tin oxide (FTO)/titanium dioxide (TiO_2)/$FAPbBr_3$/graphite paste based solar device is fabricated possessing 6.43% power conversion efficiency

with an open circuit potential of 1.47 V and external quantum efficiency of about 65%. The FTO/TiO_2/$FAPbBr_3$/Carbon/graphite sheet/water oxidation catalyst photoanode is fabricated and photoelectrochemical (PEC) water oxidation is studied. The large band gap $FAPbBr_3$ carbon based solar devices are environmentally stable, possessing high open circuit potential of about 1.47 V, higher than the thermodynamic potential of water oxidation of 1.23 V making them suitable for PEC water oxidation agent.

1. Introduction

The introduction section briefly describes about the graphene, perovskites materials, their properties, and applications. It also briefly describes the heterostructure, carbon based perovskites solar cell and photoelectrochemical water splitting.

1.1 Graphene

Graphene is a two dimensional material compiled of a monolayer atom of carbon assembled in a hexagonal lattice. It is considered among the strongest and most conductive materials proven to exist, with extraordinary thermal, electrical, and mechanical properties.[1-3] Graphene was first secluded and studied in detail in 2004 by Andre Geim and Konstantin Novoselov at the University of Manchester, who were presented the Nobel Prize in 2010.[4] Graphene can be deemed as the precursor of numerous carbon derivatives containing C60, CNTs, and graphite (figure 1.1). The exceptional assets of graphene make it a suitable candidate for variety of applications, such as sensors, electronics, biomedical devices, and energy storage.[7-12] For example, its high electrical conductivity and large surface area make it ideal for use in transistors, while its high strength and flexibility make it a promising material for use in flexible electronics and wearables. Graphene also has potential for use in water filtration and desalination because of high surface area and ability to selectively allow certain molecules to pass through. Additionally, graphene-based materials have shown promise in a range of biomedical applications, such as drug delivery and tissue engineering.

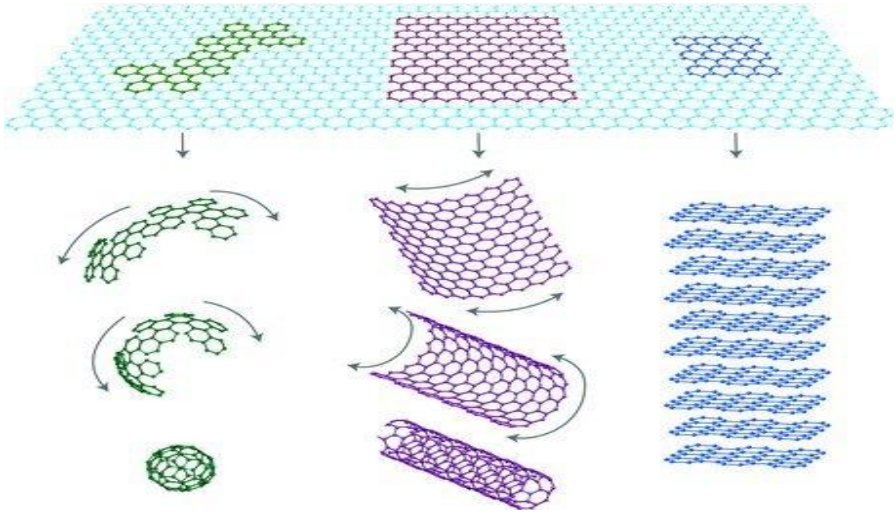

Figure 1.1 Schematic demonstration of graphene as mother of different kinds of carbon-based materials.[11]

1.1.1 Derivatives of graphene

Graphene derivatives are materials that are derived from graphene by modifying its chemical or physical properties. These derivatives can have different forms, such as graphene oxide (GO), reduced graphene oxide (rGO), graphene quantum dots (GQDs), and graphene nanoribbons (GNRs).[13]

GO is graphene that has been oxidized to contain oxygen-containing moieties, which makes it more hydrophilic and easier to disperse in solvents. Reduced graphene oxide is obtained from GO by removing some of the oxygen moieties and restoring the sp^2 carbon-carbon bonds, resulting in a material with improved electrical conductivity compared to GO.[14-18]

GQDs are tiny fragments of graphene with dimensions typically less than 10 nm. They exhibit quantum confinement effects due to their small size, which gives rise to unique optical and electronic properties, making them attractive for applications such as bioimaging and photovoltaics.[18, 19]

GNRs are narrow strips of graphene with width less than 10 nm and can be made with varying widths, edge types, and electronic properties, depending on the synthesis method. They have potential for use in electronics, as their electronic properties can be tuned by controlling their width and edge structure.[20, 21]

Other derivatives of graphene include functionalized graphene, which has been modified with chemical or biological functional groups to tailor its properties for specific applications, and graphene-based composites, which incorporate graphene into other materials to enhance their mechanical, thermal, and electrical properties. Overall, the diverse range of graphene derivatives opens many possibilities for novel applications in various fields.[22]

Few derivatives of graphene are presented in figure 1.2.

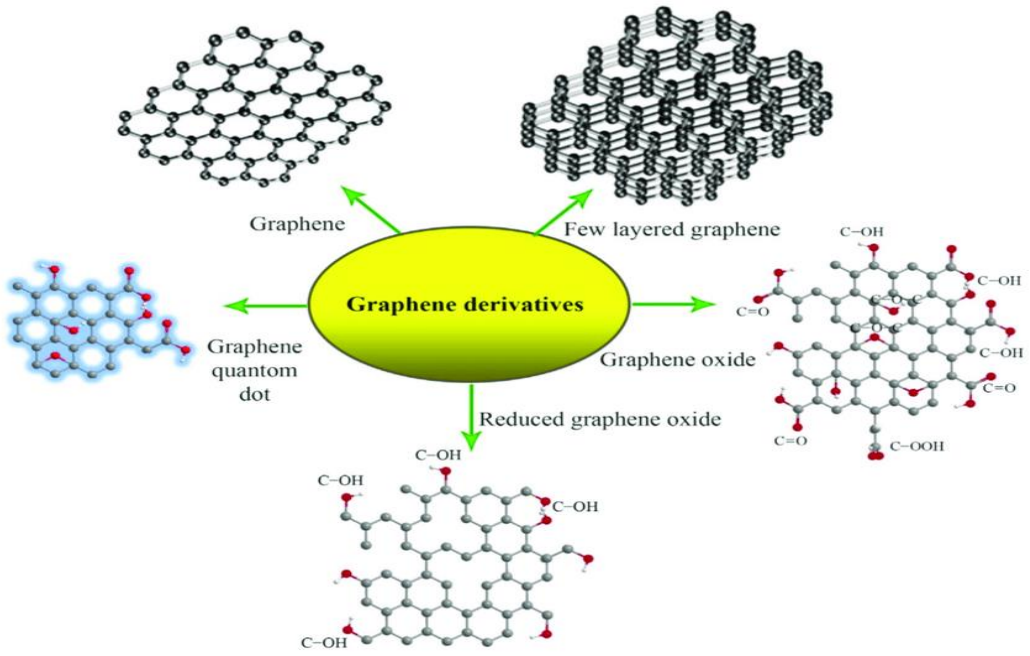

Figure 1.2 Derivatives of graphene.[23]

1.1.2 Synthesis of graphene-based nanomaterials

Generally, graphene is synthesized by two common methods, those are bottom-up and top-down approach. The separation of layers of graphite by structural breakdown known as the top-down approach. In the meantime, starting from atomic level to build up graphene structure is termed as the bottom-up technique.[24-37]

1.1.2.1 Mechanical exfoliation by graphite

One of the most well-known and simple methods for synthesizing graphene is through mechanical exfoliation of graphite. The process of mechanical exfoliation involves using adhesive tape to repeatedly remove layers of graphite. The resulting thin layers of graphite are called graphene flakes, which can then be transferred onto a substrate for further analysis. The process is simple but requires a high level of precision and skill to achieve high quality graphene flakes. The quality of the graphene flakes can be influenced by some factors, such as the starting graphite material, the type of tape used, the pressure applied during peeling, and the number of times the tape is applied.[4, 31]

1.1.2.2 Epitaxial growth from thermal deposition of SiC

This process involves depositing a thin layer of graphene on a substrate of SiC. The growth of graphene on SiC substrates can be achieved by annealing the substrate in a vacuum and exposing it to a hydrocarbon gas, like methane. As a result of reaction between SiC substrate and carbon of methane, the layer of graphene is formed. Epitaxial growth from thermal deposition of SiC offers several advantages. It allows to generate large-area films with high quality and controllable thickness. Additionally, the process is scalable, making it suitable for industrial production.[24, 25]

1.1.2.3 Chemical vapor deposition (CVD)

CVD is extensively utilized for synthesizing graphene-based materials, containing graphene films, graphene nanoribbons, and graphene quantum dots. The process involves the decay of hydrocarbon gases, like methane or ethylene, on a heated substratum to obtain a thin layer of graphene. In CVD process, the substrate is typically made of silicon dioxide, nickel, and copper is heated to high temperatures of 800 °C to 1000 °C under vacuum. The hydrocarbon gas is then introduced into the chamber, where it decomposes to form graphene. The CVD procedure can also be used to synthesize graphene on a variety of substrates, including silicon carbide, silicon, and sapphire. This flexibility allows for the integration of graphene with existing semiconductor technology and the creation of new applications in electronics, photonics, and sensors.[29-32]

1.1.2.4 Solution-based exfoliation from graphite oxide and graphite

It is a versatile method for the synthesis of graphene-based materials. In this process, the layered structure of graphite oxide or graphite is separated into individual graphene sheets using a liquid solvent and sonication process. The exfoliation process of GO involves the reduction of oxygen-containing moieties on the surface of the material, resulting in the restoration of graphene-like properties. This process can be attained through various methods, including chemical treatment, thermal reduction, or a combination of both. On the other hand, graphite can be exfoliated through sonication in a suitable solvent, which weakens the interlayer van der Waals forces and separates the graphite layers. The choice of solvent is critical in the exfoliation process, and various solvents have been used, including water, ethanol, acetone, and N-methylpyrrolidone (NMP). The resulting graphene-based materials obtained through

solution-based exfoliation can be further functionalized to shape their properties for special applications.[33, 34]

1.1.2.5 Bottom-up organic synthesis methods

It can also be utilized to synthesize graphene-based materials with specific properties and functionalities. Here are some common approaches.[33-37]

Graphene Nanoribbons (GNRs): GNRs can be synthesized through bottom-up organic synthesis methods, such as molecular self-assembly or on-surface synthesis. For example, GNRs can be synthesized by polymerizing a suitable precursor molecule, such as a graphene nanoribbon monomer, using a metal surface as a template.

Graphene Quantum Dots (GQDs): GQDs can be synthesized through bottom-up organic synthesis methods, such as the hydrothermal synthesis of graphene oxide proceed by successive reduction, or by the oxidation of graphene and successive fragmentation.

Graphene-based Nanocomposites: Bottom-up organic synthesis methods can be used to synthesize graphene-based nanocomposites by covalently attaching functional groups to graphene and then incorporating it into a polymer matrix.

Graphene-based Supramolecular Assemblies: Supramolecular assemblies of graphene and other molecules can be formed through non-covalent connections such as hydrogen bonding, π-π stacking, and electrostatic interactions. These assemblies can have exceptional properties like high conductivity, selective gas adsorption, and self-healing capabilities.

Figure 1.3 summarize the synthesis methods of graphene.

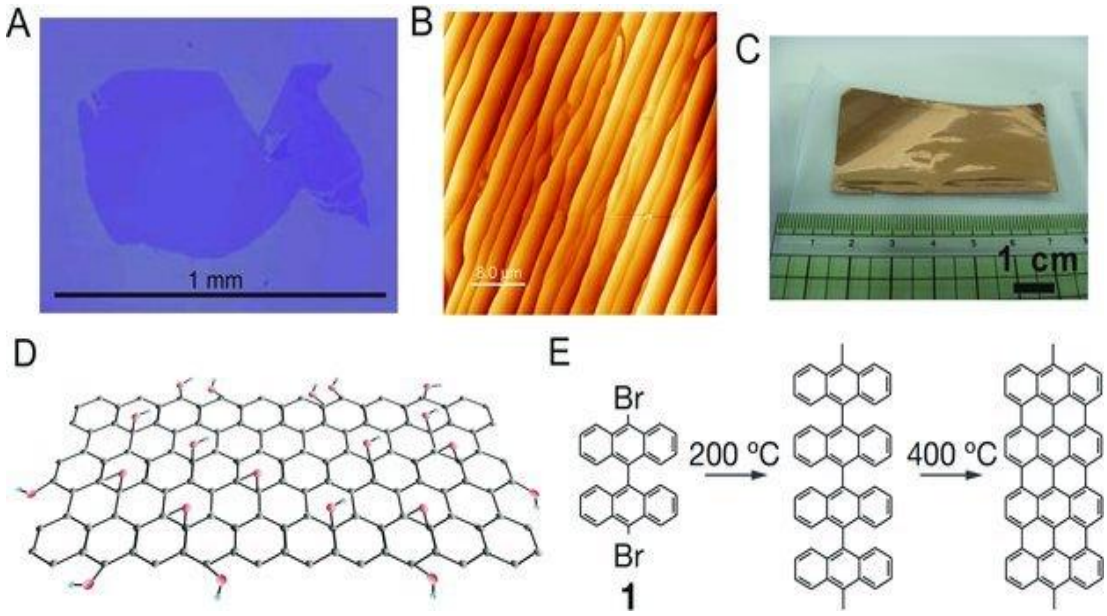

Figure 1.3 Synthesis methods for graphene-based nanomaterials. A) Mechanical exfoliation from graphite by tape against SiO_2 /Si substrate, B) High vacuum decomposition from atomic terraces on SiC wafer, C) Chemical vapor decomposition of gas or solid carbon source, D) Reduced graphene oxide by exfoliating graphite oxide following by the chemical or thermal reduction, E) Bottom-up synthesis of graphene from organic molecules with benzene rings.[37]

1.1.3 Electronic and optical properties of graphene-based nanomaterials

1.1.3.1 Electronic properties

Graphene is acknowledged for its special electronic properties, which are because of its unique structure. Here are some of the electronic properties of graphene and its derivatives given below.[38-44]

High Electron Mobility: Graphene has a high electron mobility, which is a measure of how easily electrons can move through a material. This property makes it perfect for usage in electronic devices, like transistors, where fast and efficient electron transport is necessary.[37, 39]

Zero Bandgap: Graphene has a zero bandgap, which means that it does not have a range of energies where electrons are unable to exist. This property makes it unsuitable for digital electronics, but useful for applications where a continuous spectrum of electron energies is desired, such as in photonics.[39]

Dirac Fermions: Graphene has an electronic structure that is described by Dirac fermions, which behave like massless particles that move at the speed of light. This

unique property results in several interesting facts, such as unusual quantum Hall effect and Klein tunneling.

Tunable Electronic Properties: The electronic properties of graphene can be tuned by applying an electric field or by introducing defects, such as vacancies or dopants. This property makes it possible to tailor the electronic properties of graphene for specific applications.[43]

Properties of derivatives: Graphene derivatives, such as GO and rGO, have electronic properties that are different from pure graphene. For example, graphene oxide has a bandgap, which makes it useful for digital electronics, while reduced graphene oxide has reduced electron mobility due to the introduction of defects during the reduction process.

1.1.3.2 Optical properties

Graphene unique structure gives rise to a variety of interesting optical properties.[45-54]

Transparency: Graphene is transparent to visible light, allowing it to be utilized in applications like transparent conductive films, touch screens, and solar cells.

Absorption: Graphene absorbs light in the ultraviolet, visible, and near-infrared regions of the electromagnetic spectrum. The absorption can be adjusted by adjusting the number of graphene layers or by doping the material with other atoms.

Reflection: Graphene has a low reflection coefficient, which makes it useful for antireflection coatings and optical devices.

Refraction: Graphene has a very high refractive index, which means that it can bend light at sharp angles. This property can be used in applications such as lenses and waveguides.

Plasmons: Graphene supports collective oscillations of electrons known as plasmons. Plasmons in graphene can be tuned by varying the doping level, which makes them useful for sensing and optical switching applications.

Nonlinear optics: Graphene exhibits strong nonlinear optical properties, which means that it can change the frequency and intensity of light when exposed to high-intensity laser light. This property makes it useful for applications such as frequency doubling, harmonic generation, and mode-locking.

1.1.4 Optical and optoelectronic applications of graphene-based nanomaterials

Some of the applications of graphene-based nanomaterials are described below.

1.1.4.1 Transparent conductive electrodes

Graphene is a promising material for transparent conductive electrodes because of its exceptional properties such as high electrical conductivity, high transparency, and mechanical flexibility. The high electrical conductivity of graphene arises from its high electron mobility and high carrier density, which allows for efficient charge transport. Moreover, graphene is highly transparent due to its low absorbance of light across a broad spectrum of wavelengths. This makes it an ideal material for use in transparent conductive electrodes in various optoelectronic devices, such as solar cells, touch screens, and displays. In addition to its electrical and optical properties, graphene is also mechanically flexible, which enables its use in flexible and stretchable devices. This flexibility is due to the strong covalent bonding between carbon atoms in the graphene lattice, which allows the material to withstand deformation without breaking.[55-59]

1.1.4.2 Phototransistor and photodetector

Photodetectors are devices that detect light by converting it into an electrical signal. Graphene-based photodetectors can be designed to have high sensitivity, high response speed, and low noise. One of the most used graphene-based photodetectors is the graphene photodetector, which is composed of a graphene layer and a metal electrode. When light hits the graphene layer, it generates electron-hole pairs, which are then collected by the metal electrode, resulting in an electrical signal.[59]

Phototransistors, on the other hand, are devices that can amplify a small electrical signal generated by a photodetector. Graphene-based phototransistors can be proposed to have high gain, high responsivity, and low noise. One type of graphene-based phototransistor is the graphene field-effect transistor (GFET), which consists of a graphene channel between two metal electrodes and a gate electrode separated from the graphene channel by a dielectric layer. When light hits the graphene channel, it generates electron-hole pairs, which change the conductivity of the graphene channel. By applying a voltage to the gate electrode, the conductivity of the graphene channel can be further modulated, resulting in an amplified electrical signal.[60]

Graphene-based materials have several advantages over traditional photodetectors and phototransistors, such as high sensitivity, high response speed, and low noise. Furthermore, graphene-based materials can be easily integrated with other electronic

components, making them a promising candidate for various optoelectronic applications.

1.1.4.3 Photovoltaic and light emitting devices

Graphene has presented great potential in photovoltaic and light emitting devices because of its exceptional properties like high carrier mobility, high electrical conductivity, high surface area, and excellent optical properties. Here are some examples of graphene-based materials in these devices.[61-69]

Graphene-based solar cells: Graphene can be utilized as a transparent conductive electrode in solar cells, replacing traditional indium tin oxide (ITO) electrodes that are expensive and brittle. Graphene-based solar cells have shown improved efficiency and stability compared to ITO-based solar cells due to graphene's excellent mechanical flexibility, high electrical conductivity, and high transparency. Moreover, graphene can also be used as a nanomaterial to boost the light absorption of solar cells, which can further improve their efficiency.

Graphene-based light-emitting diodes (LEDs): Graphene can also be utilized as a transparent electrode in LEDs, replacing ITO electrodes. Graphene-based LEDs have shown improved efficiency and transparency compared to ITO-based LEDs. Moreover, graphene can also be used as a nanomaterial to enhance the light extraction efficiency of LEDs, which can further improve their brightness and efficiency.

Graphene-based perovskite solar cells: Perovskite solar cells have shown great potential in achieving high efficiency and low-cost solar energy conversion. Graphene can be used as a hole transport layer in perovskite solar cells, replacing traditional organic hole transport materials that are unstable and have limited stability. Graphene-based perovskite solar cells have shown improved stability and efficiency compared to traditional perovskite solar cells.

1.1.4.4 Saturable absorber for ultrafast lasers

In an ultrafast laser, the saturable absorber is a material that can quickly and reversibly change its optical properties in response to the intensity of the laser pulse. This allows the laser to produce short, high-intensity pulses, which are useful in a wide range of applications such as material processing, medicine, and spectroscopy.

Graphene-based materials have several advantages as saturable absorbers in ultrafast lasers. Firstly, they have a broad absorption bandwidth that covers a wide range of wavelengths, making them suitable for use with different types of lasers. Secondly,

they have a high nonlinear optical response, which means that they can quickly and efficiently absorb laser pulses with high intensity. Third, they have a fast recovery time, allowing them to quickly return to their original state after absorbing a laser pulse.[70, 71]

1.1.4.5 Photocatalytic applications

Graphene-based materials have been widely explored for their potential photocatalytic applications because of exceptional properties like high surface area, high electrical conductivity, and excellent chemical stability. Photocatalysis is a process where a catalyst is activated by light to initiate a chemical reaction.

Some of the potential photocatalytic applications of graphene-based materials are,[72-84]

Water purification: Graphene-based materials have been studied as photocatalysts for the elimination of pollutants like organic dyes, heavy metals, and bacteria from water.

Solar energy conversion: Graphene-based materials have been used in the progress of solar cells and other devices for solar energy conversion. The high electrical conductivity of graphene-based materials makes them ideal for use in electrodes, and their light absorption properties can be used to enhance the efficiency of solar cells.

Air purification: The high surface area and strong light absorption properties of graphene-based materials can be used to remove pollutants such as volatile organic compounds (VOCs) and nitrogen oxides (NOx) from the air.

CO_2 reduction: Graphene-based materials have been studied for their potential use as photocatalysts for CO_2 reduction that convert CO_2 into useful chemicals such as methanol and methane.

Some of the applications of graphene-based nanomaterials are summarize in figure 1.4.

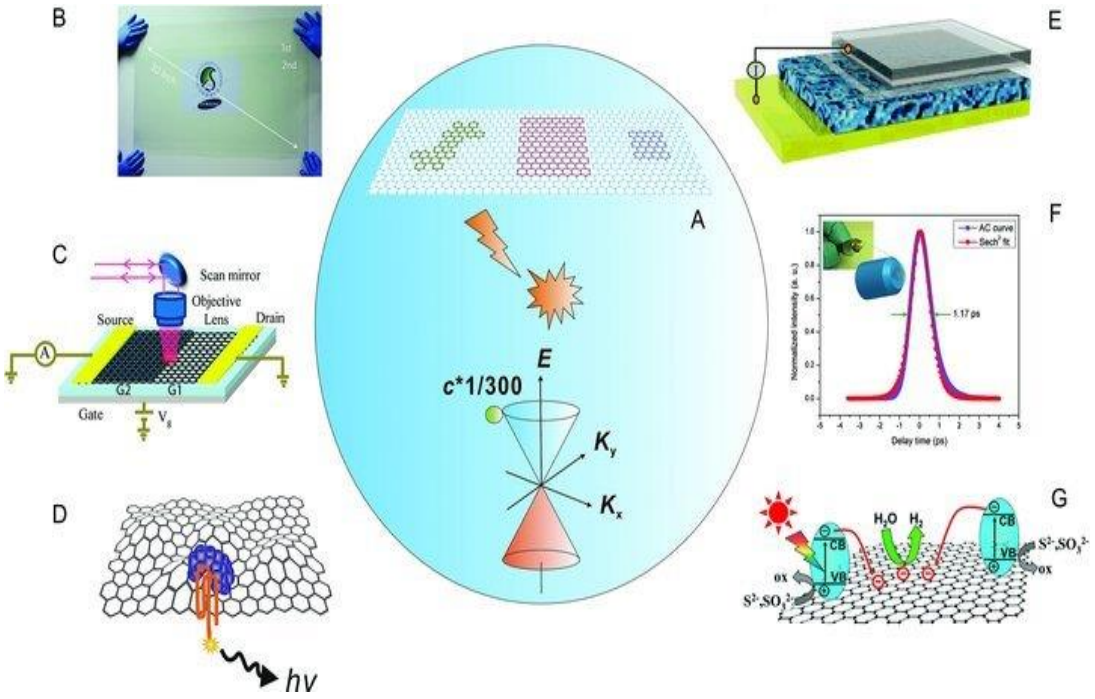

Figure 1.4 A. Graphene-based nanomaterials in optical and optoelectronic applications. The dynamic combination of unique structure and electronic/optical properties of graphene have encouraged many new optical and optoelectronic possibilities. B. transparent electrodes, C. Phototransistors, D. Biological sensors, E. Photovoltaic device, F. Ultrafast laser based on graphene saturable absorber, G. Photocatalysis.[37]

1.2 Perovskites

Perovskites are materials with a definite crystal structure that has the chemical formula ABX_3, where A and B are cations and X is an anion. The perovskite crystal structure is characterized by a cubic unit cell with the A cations located at the corners, the X anions located at the center of the cell, and the B cations located at the center of each face. Halide perovskites possessed a chemical formula of ABX_3 (figure 1.5), where A is a monovalent cation (e.g., Cs^+, Rb^+, $CH_3NH_3^+$ (MA^+) or $HC(NH_2)_2^+$ (FA^+)), B is a bivalent metal cation (e.g., Pb^{2+}, Sn^{2+}) and X is a halide anion (typically Cl^-, Br^-, I^- or their mixtures). The structure of these perovskites is very flexible, which accounts for the tunable optical and electrical properties of these materials in a wide range.[85]

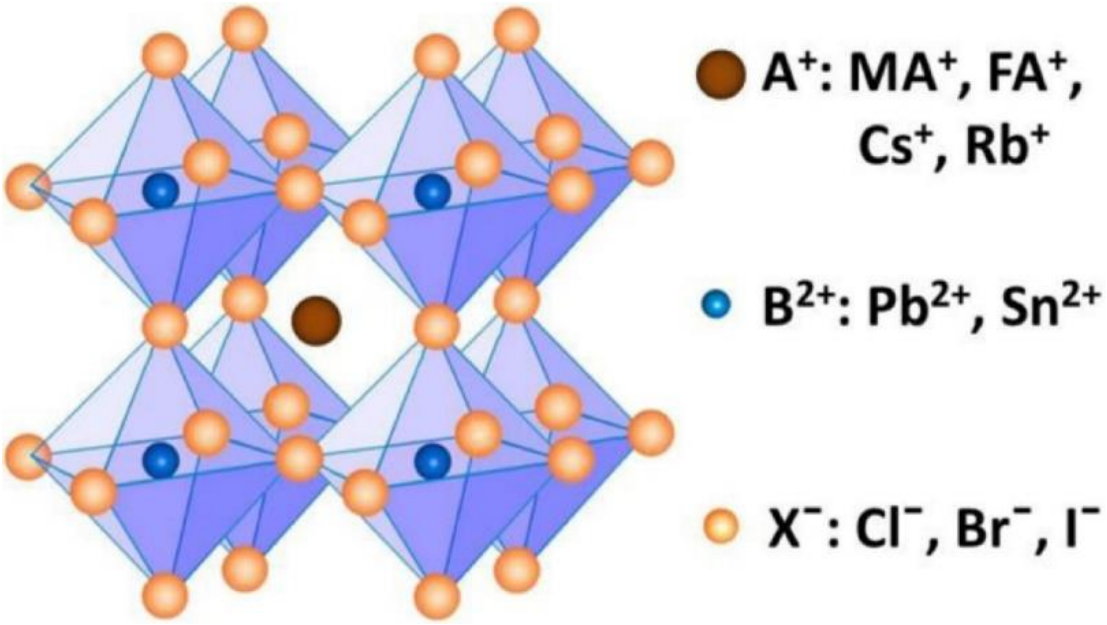

Figure 1.5 Perovskite crystalline structure ABX_3.[85]

Perovskite nanocrystals (NCs), also known as quantum dots (QDs), are tiny crystalline particles with dimensions on the order of a few nanometers (10^9 meters). These nanocrystals have exclusive optical and electronic properties because of quantum confinement effects, which arise when the size of a material is reduced to a scale where the motion of electrons is restricted.[86] Perovskites NCs exhibit high photoluminescence quantum yields, narrow emission linewidths, and tunable emission wavelengths, making them attractive for use in a range of applications such as light-emitting diodes (LEDs), lasers, photovoltaics, and biological imaging.[87-96]

1.2.1 Synthesis methods of perovskites NCs

They can be synthesized using different synthesis procedure, including solution-based techniques such as hot-injection and ligand-assisted reprecipitation, and gas-phase methods such as chemical vapor deposition (CVD). Here are some of the common synthesis methods for perovskite nanocrystals described below.[87-96]

1.2.1.1 Solvothermal synthesis

In solvothermal synthesis, a mixture of precursor salts and solvents is heated in a sealed vessel at high temperature and pressure. This method is often used to synthesize high-quality perovskite NCs with controlled size and shape.

1.2.1.2 Colloidal synthesis

Colloidal synthesis is a popular method. In this method, the precursors materials are dispersed in a solvent, and a reducing agent is added to initiate the reaction. The size and shape of the NCs can be managed by adjusting the reaction setting such as solvent composition, temperature, and concentration of the precursors.

1.2.1.3 Hot injection synthesis

Hot injection synthesis involves injecting a solution of precursor salts into a high-temperature solution containing a reducing agent. The rapid mixing of the solutions initiates the nucleation and growth of perovskite NCs. This method is often used to synthesize perovskite NCs with narrow size distribution and high quantum yield.

1.2.1.4 Microwave-assisted synthesis

In microwave-assisted synthesis, a mixture of precursor salts and solvent is heated using microwave irradiation. The high energy input from the microwaves can accelerate the reaction rate and lead to the formation of perovskite NCs in a short time.

1.2.1.5 Gas-phase synthesis

Gas-phase synthesis involves the reaction of precursor gases in a high-temperature furnace to form perovskite NCs. This method is often used to synthesize large quantities of NCs with controlled size and composition.

1.2.2 Optical and optoelectronic properties of perovskites NCs

Some of the optical and optoelectronic properties of perovskite NCs are given below.

1.2.2.1 Tunable bandgap:

Perovskite NCs have tunable bandgap that can be easily controlled by varying the size, composition, and morphology of the NCs. This property makes perovskite NCs suitable for various optoelectronic applications, such as solar cells, LEDs, and photodetectors.

1.2.2.2 High absorption coefficient

Perovskite NCs have a high absorption coefficient, which means they can efficiently convert photons into electrical charge carriers. This property is crucial for solar cell applications, where the goal is to maximize the amount of light absorbed and converted into electrical energy.

1.2.2.3 High quantum yield

Perovskite NCs have a high quantum yield, which means they can efficiently emit light when excited by an external source. This property is essential for LED applications, where the goal is to maximize the amount of light emitted for a given amount of electrical power input.

1.2.2.4 Long carrier lifetime

Perovskite NCs have a relatively long carrier lifetime, which means they can sustain charge separation for an extended period. This property is beneficial for photovoltaic applications, where the goal is to maximize the efficiency of charge collection and conversion into electrical energy.

1.2.2.5 High Stability

Perovskite NCs have shown significant improvements in stability in recent years, making them more suitable for commercial applications. This stability is crucial for optoelectronic devices, which require long-term performance and durability.

1.2.3 Applications of perovskites NCs

Perovskite NCs have a wide range of potential applications due to their unique optical and electronic properties. Some of the most promising applications are described below.

Lighting: Perovskite NCs can be used in the production of high-quality lighting sources, such as LEDs and quantum dots. They have high photoluminescence quantum yields, which means they can efficiently convert electrical energy into light.

Solar cells: Perovskite NCs have been used to fabricate high-performance solar cells with efficiencies exceeding 25%. They have the potential to replace traditional silicon-based solar cells due to their lower cost and easier manufacturing process.

Sensors: Perovskite NCs can be used as sensing materials for the detection of gases, biomolecules, and other analytes. They have high surface-to-volume ratios, which makes them highly sensitive to changes in their environment.

Photodetectors: Perovskite NCs can be used to fabricate highly sensitive photodetectors for a range of applications, including medical imaging and security systems.

Optoelectronics: Perovskite NCs have been used to fabricate a range of optoelectronic devices, including lasers, optical switches, and waveguides. They have the potential to

revolutionize the field of optoelectronics due to their unique properties and ease of fabrication. Some of the most promising applications are described in figure 1.6.

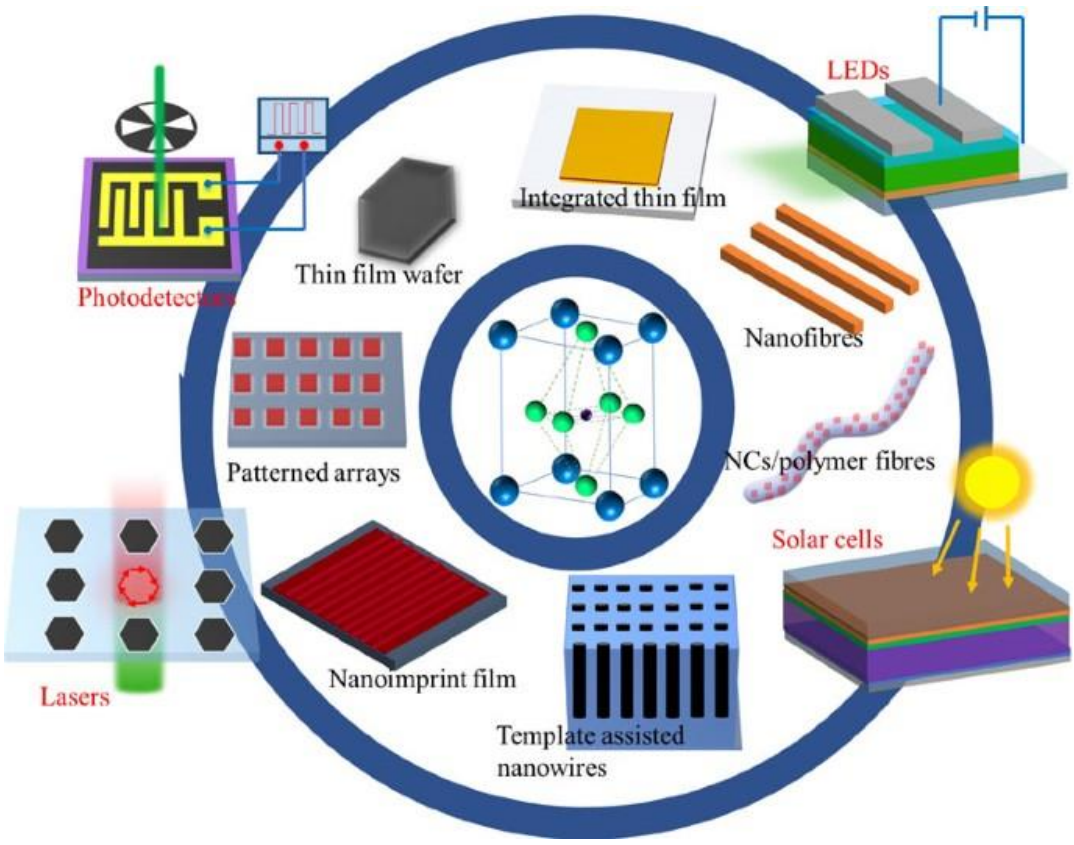

Figure 1.6 Applications of perovskites NCs. [97]

1.2.4 Photovoltaics applications of perovskites NCs

Perovskite NCs have shown great potential for use in photovoltaic (PV) applications due to their unique properties, such as high optical absorption coefficients, long carrier diffusion lengths, tunable bandgaps etc. as summarize in figure 1.7. Some of the potential applications of perovskite NCs in PV are described below.[98]

Figure 1.7 Properties of perovskites making it a suitable candidate for photovoltaic.[99]

Solar cells: Perovskite NCs can be used in the fabrication of highly efficient solar cells. The perovskite NCs can be used as a light-absorbing layer in the solar cells, which converts the sunlight into electricity. These solar cells have shown efficiencies exceeding 25%, which is comparable to traditional silicon-based solar cells.

Tandem solar cells: Perovskite NCs can also be used in tandem solar cells. Tandem solar cells are a combination of two or more solar cells with different bandgaps, which allows them to harvest a broader range of the solar spectrum. Perovskite NCs can be used as a top cell in the tandem solar cells due to their high optical absorption coefficients and tunable bandgaps.

Luminescent solar concentrators (LSCs): Perovskite NCs can be used in LSCs, which are devices that concentrate sunlight onto small solar cells using a waveguide. The perovskite NCs are used as the luminescent material in the LSCs, which absorbs the sunlight and emits it at a longer wavelength, increasing the efficiency of the solar cells.

Solar fuel generation: Perovskite NCs can also be used in the generation of solar fuels such as hydrogen or methanol. The perovskite NCs can be used as a photocatalyst,

which absorbs the sunlight and catalyzes the chemical reactions that produce the solar fuels.

1.3 Heterojunction/Heterostructure and charge transfer

Combining two semiconductors' materials possessing unlike band gaps to create heterojunction has been included in important research areas for scientists to pay an attention in this research area, as resulting heterostructures possess exceptional interfacial properties at nano-scale domain; those are remarkably diverse as compared to bulk materials. The creation of close interfacial interaction at interface of heterostructures result in the generation of electric field at interface due to right band alignment and separation/movement of charges is significantly valuable for optoelectronic applications. Therefore, combining the semiconductors can facilitate the improved light absorption in broad UV-Vis region, efficient charge separation because of the prolonged lifetime via inhibited recombination of charges (electrons and holes) and outstanding photostability because of charge splitting at the interface of heterojunction, which avoid the charge gathering.[100,101] The heterojunction can be classified into three classes subjected on the band gap offsets of the two combining materials (say A and B).[102]

Type I (Straddling gap)

Type II (Staggered gap)

Type III (Broken type)

Type I

In this type of heterojunction, the valence band (VB) of species A is comparatively more positive than species B and conduction band (CB) is comparatively more negative as compared to the species B. As a result, the charge carriers generated as light shines on the semiconductors, can go across their respective potential that is electrons move down the potential (from CB of species A to VB of species B) and holes move up the potential (from VB of species A to the VB of species B). In such type of heterojunction, the charge carriers collect on one semiconducting material.

Type II

In this type of heterostructure, the band edges of two materials are arranged in such a way, the VB of species B is less positive as compared to species A and CB of species B is more negative as compared to the species A. As a result, the electron transfer from species B to species A and holes transfer from species A to species B. In

such type of heterojunction, the charge carriers are separated effectively at the interface of heterojunction.

Type III

In this type of heterostructure, the band edges of two materials are arranged in such to show broken up alignment. The charge carriers can be transferred in these heterojunctions in the same way as in type II. Figure 1.8 represents schematically the three types of heterojunctions created by combining two semiconducting species.

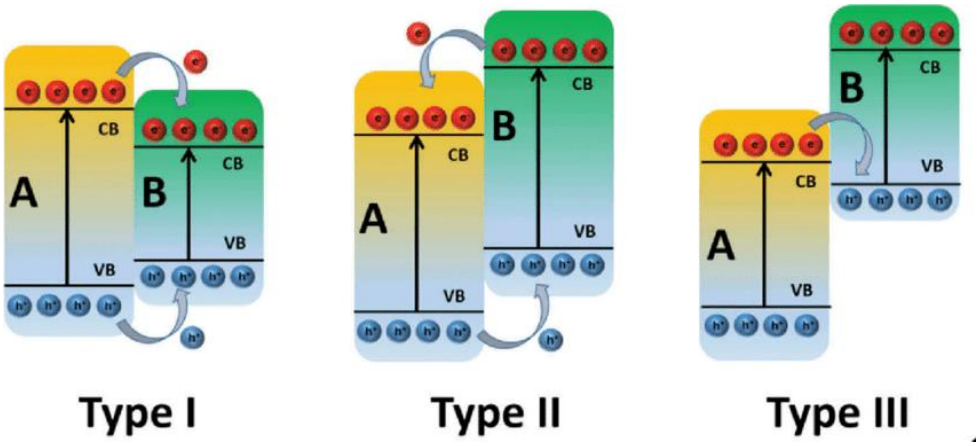

Figure 1.8 Schematic representation of charge transfer across type I, type II, and type III heterostructure formed by combining two semiconductor materials.[103]

1.4 Carbon based perovskites solar cells

Solar cells that utilize carbon as a counter electrode are known as carbon-based counter electrode solar cells. In traditional solar cells, the counter electrode is typically made of expensive materials such as platinum (Pt) or indium tin oxide (ITO). Carbon-based counter electrodes offer a more cost-effective and sustainable alternative.[104,105] Carbon-based counter electrodes can be fabricated using various carbon materials, including carbon nanotubes, graphene, carbon black, and conductive polymers. These materials possess good electrical conductivity and can catalyze the redox reactions that occur during the operation of a solar cell.[104]

Carbon-based counter electrodes offer several advantages over traditional materials. They are abundant, low-cost, and environmentally friendly. Moreover, they can be easily synthesized and integrated into solar cell devices.

However, it is important to note that the efficiency and performance of carbon-based counter electrode solar cells may not always match those of platinum or ITO-

based counterparts. Researchers are actively working to improve the catalytic activity and stability of carbon-based materials to enhance their performance in solar cell applications.[106] Typical architecture of carbon-based perovskites solar cell is displayed in figure 1.9.

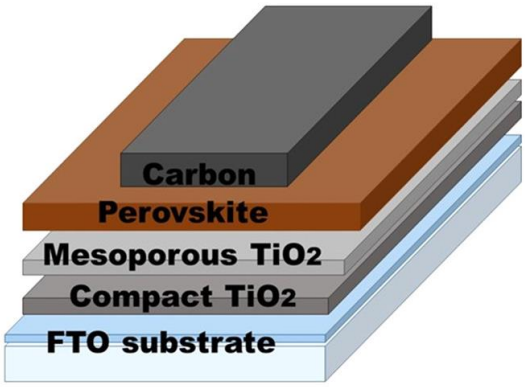

Figure 1.9 Device architecture of carbon-based perovskites solar cells.[107]

1.5 Photoelectrochemical water splitting

Photoelectrochemical (PEC) water splitting is a process that utilizes solar energy to split water molecules into hydrogen and oxygen through electrochemical reactions. It involves the use of a photoelectrochemical cell, which consists of a photoelectrode, an electrolyte, reference, and a counter electrode.

The photoelectrode is a semiconductor material that absorbs sunlight and generates electron-hole pairs. Typically, materials like metal oxides, such as titanium dioxide (TiO_2)[108]or bismuth vanadate ($BiVO_4$),[109] are used as photoelectrodes. These materials have suitable bandgaps to absorb solar energy and facilitate the water splitting process.

When sunlight is absorbed by the photoelectrode, electrons are excited from the valence band to the conduction band, leaving behind positively charged holes. The separated electrons and holes participate in electrochemical reactions at the surface of the photoelectrode.

The photoelectrode is in contact with an electrolyte, which usually consists of an aqueous solution containing ions. The electrolyte helps transport the charge carriers (electrons and ions) and facilitates the redox reactions involved in water splitting.[110]

At the photoelectrode, the excited electrons participate in the reduction reaction, which occurs at the interface between the photoelectrode and the electrolyte. This reaction involves the reduction of water molecules to produce hydrogen ions (H^+) and electrons (e^-):

$$2H_2O + 2e^- \longrightarrow 2H^+ + 2OH^-$$

The generated hydrogen ions can subsequently combine to form hydrogen gas (H_2) at a separate electrode known as the cathode. Meanwhile, the holes generated in the photoelectrode participate in the oxidation reaction, which takes place at the counter electrode. Typically, a metal or conductive material, such as platinum or carbon, is used as the counter electrode. At the counter electrode, the oxidation of water occurs, resulting in the production of oxygen gas (O_2):

$$2H_2O \longrightarrow O_2 + 4H^+ + 4e^-$$

The overall process of PEC water splitting converts sunlight into chemical energy stored in the form of hydrogen fuel, which can be used as a clean and renewable energy source.[111,112]

PEC water splitting is an area of active research, with ongoing efforts to improve the efficiency, stability, and scalability of the process. Researchers are exploring various materials, nanostructures, and catalysts to enhance the performance of photoelectrodes and electrolytes, aiming to achieve higher solar-to-hydrogen conversion efficiencies and long-term stability.

1.6 Review literature

Addressing elementary photophysical properties of perovskites NCs in combination with other materials in the form of heterostructures calls for investigation and is predictable to further the applications of perovskites NCs in multidimensional energy related fields. Designing perovskites heterostructures with other multidimensional materials can have several distinctive advantages like, providing stability towards polar solvents, surface defects passivation by direct interacting with vacancies, permitting type I or quasi-type II band alignment to increase charge recombination or effective charge separation.[113-115] Among these interests, charge separation and charge-transfer studies in perovskite-based electron donor–acceptor structures gain great momentum, which is due to their potential application in modern technology. For example, Hongzheng chen group introduced a perovskites/CdS based heterojunction and observed the charge transfer that occur in perovskites/CdS

heterostructures. This novel introduced heterostructure is utilized to fabricate a planar heterostructures perovskites solar cells with CdS as an electron transport layer.[116] Grätzel and co-workers revealed ultrafast electron transfer from photoexcited perovskite to mesoporous titanium dioxide, leading to efficient charge separation.[117] In a subsequent report, Soltani and co-workers pinpointed the time scale and mechanism of electron transfer from perovskite to an organic acceptor molecule.[118] Perovskites NCs have been explored in electron transfer to classical acceptors such as benzoquinone,[119] phenothiazine and perylene.[120, 121] Recent studies by the research groups of Huang and Sargent show improved stability and photocurrent response for solar cells based on C_{60}-layered perovskites, which are attributed to passivation of surface defects and removal of grain boundaries in perovskites by C_{60}.[122] Hence, there studies open a new door to improve the device efficiency by passivating the grain boundaries. Qiyi Fang and colleagues reported the ultrafast charge transfer in perovskites nanowire and 2D transition metal dichalcogenide heterostructures.[123] Muduli et al. reported that the electron transfer from perovskites to few layers black phosphorus sheets is the phenomenon responsible for the photoluminescence quenching of perovskites observed in perovskites/black phosphorus heterostructures.[124] Pan et al. successfully grew the perovskites NCs on Mxene nanosheets. They observed the charge transfer in this heterostructure and utilized this nanocomposite for enhanced photoelectric detection and photocatalytic reduction of CO_2.[125] Similarly, Ou et al. reported that amino group of the ligand is responsible for the anchoring of the perovskites QDs on porous g-C_3N_4 and facilitates charge transfer. They used this heterojunction for photocatalytic reduction of CO_2.[126] Ravi and co-workers obtained $CsPbBr_3$/ZnS core-shell type NCs and observed that introduction of ZnS in perovskites NCs enhanced its luminescence lifetime and water stability.[127] Liu et al. utilized nCdS with perovskites QDs to produced core-shell NCs and reported that CdS involved in self-passivation of QDs.[128] Brumberg et al. explored that, besides other factors, dimensionality of a material is also a factor that effect the rate of electron transfer in perovskites-CdSe nanoparticles.[129] Wang et al. introduced $CsPbBr_3$/PbSe heterostructure NCs and obtained high efficiency solar cells.[130] Rathore et al. introduced the heterostructure of $CsPbBr_3$ attached with nitrogen doped carbon dots and explain the charge transfer phenomenon in this heterojunction in detail.[60]

Recently, graphene attachment with perovskites systems is gaining significant attention owing to its excellent physical and chemical properties such as high electrical

conductivity,[131] excellent transparency,[132] ambipolar charge transport and superior chemical and heat stability.[133, 134] It finds applications in variety of fields, such as, optoelectronic, energy generation, energy storage devices and sensors etc.[135-138] For example, Zhongwei Wu group fabricated the planar heterojunction perovskite solar cells employing graphene as hole conducting layer.[139] Zhange et al. observed the phase stability of γ-$CsPbI_3$ perovskite NCs by interface effect using iodine modified graphene oxide.[140] Park et al. reported the enhanced photoluminescence quantum yield of $MAPbBr_3$ nanocrystals by defect passivation using graphene.[141] Pu et al. claims the enhancing effects of reduced graphene oxide on photoluminescence of $CsPbBr_3$ perovskite QDs.[142] Tang et al. introduced the $CsPbBr_3$/Reduced Graphene Oxide nanocomposites and studied their enhanced photoelectric detection application.[143] Xu and co-workers utilized perovskites/graphene oxide composite for photocatalytic reduction of CO_2.[144] Mishra and co-workers studied the photo-induced charge transfer in perovskites NCs-quinone assemblies and studied its impact on conduction current.[145] Biswas et al. explored the role of short chain acids as surface ligands in photoinduced charge transfer dynamics from perovskites NCs.[146] Cohen et al. studied the heterostructures of polymers hosting the perovskites NCs.[147] The group of Prashant V. Kamat are actively working on charge transfer phenomenon in multidimensional perovskites heterostructures. His group also recently reported the electron transfer in perovskites-rhodamine light harvesting assemblies.[148]

Hence, till now, there are many perovskites based multidimensional heterojunctions possessing effective charge separation are reported and utilized in various, optoelectronic applications.

1.7 Aims and objectives of the present work

Depletion of fossil fuels with growing human population, increase the more interest of the researcher to put efforts to advent the new ways to overcome these energy crises by utilizing the natural sources especially sunlight. In this regard, solar cells based on perovskites materials are becoming an emerging star day by day. The environmental instability of the perovskites devices is a major hurdle in the practicability of these devices. Generating H_2 fuel by water splitting is also becoming an important emerging research field of the modern era to replace the other depleting sources of energy.

Keeping in view, the present research work is focused to attach environment friendly and stable graphene with perovskites and to study the detailed effects of graphene on the charge transfer dynamics of the perovskites that also affects the overall efficiency of the devices besides other factors. Also, to fabricate the perovskites based solar device and to study its applications in photoelectrochemical (PEC) water splitting for H_2 fuel generation.

The specific objectives of the proposed work follow as:

- Synthesis of perovskite NCs
- Synthesis and functionalization of graphene materials
- Fabrication of perovskite nanocrystals-graphene heterostructures
- Assessment of charge transfer in perovskite nanocrystals-graphene heterostructures
- Fabrication of solar cell device and PEC water splitting studies of the solar device

2. Experimental

In this section, the materials used in the present work, synthesis methods used for graphene, functionalized graphene, perovskites and their heterostructures are described with the procedure of $FAPbBr_3$ perovskites solar device. As well as the characterization techniques employed for the characterization of samples are also described.

2.1 Materials and methods used

2.1.1 Chemicals and reagent

All the materials were used as purchased without any further purification and processing.

Table 2.1 List of chemicals/reagent/materials used.

Reagent/Material	Percentage purity	Supplier
Fluorine-doped Tin oxide (FTO) glass (TEC 7) with 2 mm thickness and 7 Ω/cm^2 resistance	-	Sigma-Aldrich
Zn powder	-	Sigma-Aldrich
Titamium diisopropoxide(bisacetylacetonate)	75 wt% in IPA	Sigma-Aldrich
30 NR-D titania (TiO_2) paste	-	Greatcell Solar
Bis(trifluoromethane)sulfonimide lithium	99.99%	Sigma-Aldrich
N, N-dimethylformamide	99.98%	Sigma Aldrich
Mercaptoacetic acid (MAA)	98%	Across organics
Formamidinium bromide (FABr)	-	Greatcell Solar
Isopropanol (IPA)	99.99%	Sigma Aldrich
Lead bromide	98%	BDH chemicals
Cesium bromide	99%	Sigma Aldrich
Graphite powder	≥ 99%	DAE JUNG
Low temperature carbon paste	-	Dycotec
Hydrochloric acid (HCl)	99.8%	Sigma Aldrich
hydrogen peroxide (H_2O_2)	99 %	Sigma Aldrich
Potassium manganese oxide ($KMnO_4$)	99 %	Sigma Aldrich

Sodium nitrate ($NaNO_3$)	99 %	Sigma Aldrich),
Tetrabutylammonium hexefluorophosphate ($TBAPF_6$)	98 %	Sigma Aldrich
Sulphuric acid (H_2SO_4)	98 %	Sigma Aldrich
Absolute ethanol	99.9 %	Sigma Aldrich
Acetonitrile	99.7 %	Sigma Aldrich
Alanine	98%	Sigma Aldrich
Cysteine	99%	Sigma Aldrich
Tyrosine	98.9%	Sigma Aldrich
Toluene	99.99%	Sigma Aldrich
Formamidinium acetate (FAAc)	99 %	Sigma Aldrich
Hydrazine hydrate	99 %,	Sigma Aldrich
1-Propanol	≥ 98%,	Fluka
Oleyl amine (OAm)	99.9 %,	Sigma Aldrich
Oleic acid (OA)	99.9 %,	Sigma Aldrich
Hexane	99.7%	Sigma Aldrich

2.1.2 Synthesis of $CsPbBr_3$ NCs

To prepare the precursors solution of lead halides, Cesium bromide, CsBr (0.1 mM) and lead bromide, $PbBr_2$ (0.1 mM) were dissolved in N, N-dimethylformamide. Then various concentrations of MAA (0.25 mM, 0.5 mM, 0.75 mM, 1 mM) were added under continuous stirring. Afterward, 200 µL of the reactant salt solution was inserted into 10 mL of toluene resulting in the formation of green emitting $CsPbBr_3$ perovskite NCs. To understand the effect of MAA on the properties of $CsPbBr_3$ perovskite NCs, $CsPbBr_3$ perovskite was also prepared by adapting the same procedure except the addition of MAA.

2.1.3 Preparation of graphene (Gr)

Graphite powder was used to prepare graphene oxide (GO) by employing modified Hummer's method.[149] Briefly, 0.5 g of graphite powder, 0.25 g of $NaNO_3$ and 1.5 g of $KMnO_4$ were mixed in 12 mL of H_2SO_4 (98%) by maintaining the temperature at 0 ^oC using an ice bath under continuous stirring. Later, the reaction blend was maintained at 100 ^oC for 1.5 hours. Afterwards plenty of deionized (DI) water and H_2O_2

(2 mL) was added to the reaction mixture. The obtained GO solution was washed several times with DI water and 10 % HCl solution to remove metal ions and dried at 60 ^{o}C for overnight. We employed double reduction approach to completely transform GO to graphene (Gr). The obtained GO powder was reduced to Gr twice by using an appropriate amount of hydrazine at 50 ^{o}C overnight to transform reduced GO sheets to Gr sheets.[150] Briefly, 3 mg/mL of GO in water was sonicated for 3 hours. Then 1 μL of hydrazine hydrate was added while stirring in an oil bath at 80 ^{o}C. The reaction was left for 12 hours to complete and at the end of this time a black powder was obtained. After cooling, the Gr was separated and washed with distilled water. The obtained black suspension was centrifuged at 3000 rpm for 1 hour to remove unexfoliate Gr sheets. The black powder of graphene sheet was dried at 60 ^{o}C overnight in an oven. For steady-state photoluminescence (PL) and time-resolved PL measurements, the Gr was spread in toluene and sonicated for half an hour to obtain a homogeneous solution of Gr sheets.

2.1.4 Preparation of functionalized graphene

The functionalization of graphene was achieved by using previously reported method.[151] 0.1 g of GO powder was mixed in 10 ml of DI water followed by the addition of 0.3 g of amino acid (alanine or cysteine or tyrosine) under continuous stirring. After that, an equimolar amount of NaOH in 10 ml DI water was dissolved and added to the reaction mixture. The reaction mixture was kept on stirring overnight at room temperature. The obtained colloidal mixture was treated with ethanol and precipitate of the product is obtained by centrifugation that was washed with water/ ethanol solution (to remove excess NaOH) until the neutral precipitate was obtained. The product was dried at 60 ^{o}C for overnight in vacuum oven.

2.1.5 Preparation of $CsPbBr_3$ NCs/Alanine functionalized graphene (N-Gr) heterostructures

For the formation of heterostructures, the sample of 0.5 mM MAA capped $CsPbBr_3$ NCs owning better optoelectronic properties was selected. The solutions of 0.5 mM MAA capped $CsPbBr_3$ NCs (1 g/L) and N-Gr (1 g/L) was prepared in toluene. To prepare $CsPbBr_3$ NCs/N-Gr heterostructures, various amounts of N-Gr (10 mg/mL to 60 mg/mL) were added to the solution of $CsPbBr_3$ NCs and mixture was sonicated for 30 minutes at room temperature to facilitate the attachment of N-Gr to $CsPbBr_3$ NCs. The PL of the above-mentioned solution was carried out, while for time-resolved

photoluminescence (TRPL) studies, a thin film of N-Gr first drops casted on quartz slides, dried and above this layer, a thin layer of NCs were drop casted, dried, and then used for TRPL analysis.

2.1.6 Synthesis of formamidinium lead bromide ($FAPbBr_3$) NCs

A facile synthesis procedure was adopted for the synthesis of $FAPbBr_3$ NCs.[152] Briefly, 1 mL of lead bromide precursor solution was prepared by taking 185 mg/mL of lead bromide in a vial and adding 1- propanol, oleylamine and oleic acid in a ratio of 1:1:1 by volume. The lead bromide precursor solution was heated to 80 ^oC under continuous stirring. In the meantime, 18 mg of formamidinium acetate (FAAc) was dissolved in 3 mL of 1-propanol, after mixing 6 mL of hexane was added to the resulting solution and stirred for a few minutes. 0.9 mL of lead bromide precursor solution was injected quickly into the FAAc precursor solution and green emitting $FAPbBr_3$ NCs were obtained within a few seconds. The obtained product was centrifuged at 3000 rpm for 2 min to separate the large, aggregated particles and supernatant was preserved. For the separation of the NCs, the solution was washed 3 times with toluene/acetonitrile (9:1) solution and centrifuged at 6000 rpm for 5 min for the collection of solid $FAPbBr_3$ NCs. The obtained product was dried at 60 ^oC overnight in oven for further use.

2.1.7 Preparation of $FAPbBr_3$ NCs/Graphene (Gr) heterostructures

The solutions of $FAPbBr_3$ NCs (1 g/L) and Gr (1 g/L) were prepared in toluene. To prepare $FAPbBr_3$ NCs/Gr heterostructures, various amounts of graphene solution (100 μL-700 μL) were added to 5 mL solution of $FAPbBr_3$ NCs and the mixture was sonicated for 30 minutes at room temperature to facilitate the attachment of graphene to $FAPbBr_3$ NCs.

2.1.8 Formation of $FAPbBr_3$ NCs/Functionalized graphene heterostructures

1 mg of graphene oxide (GO), Cysteine functionalize graphene oxide (GO-Cys), Tyrosine functionalize graphene oxide (GO-Tyr), and alanine functionalize graphene oxide (GO-Ala) were dispersed in 10 mL of toluene (Figure 2.1) and mixed each 1 ml of dispersion with 5 mL of 1 mg $FAPbBr_3$ NCs in toluene solution and kept on stirring for half an hour at 40 ^oC. The ensuing $FAPbBr_3$ NCs/Functionalized graphene heterostructures were used for further studies. To conduct the control experiment, the 1 mg of alanine, cysteine, tyrosine, was also dissolved in toluene, being polar in nature, amino acids are not dissolved in anhydrous toluene even after a stirring/sonication of

half an hour. Then, 0.1 mg of each amino acid were directly added to the solution of NCs and left on stirring for half an hour under same conditions.

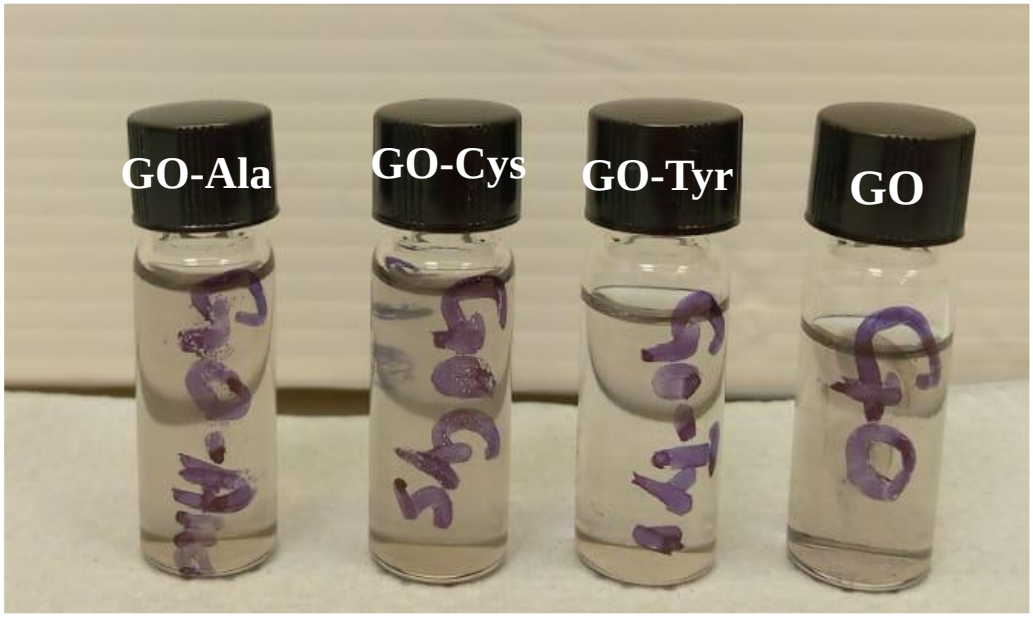

Figure 2.1 0.1 mg/ml dispersion of GO, GO-Ala, GO-Tyr, and GO-Cys in toluene.

2.1.9 Preparation of solar cells devices containing $FAPbBr_3$ perovskites as light absorber and commercial carbon paste

The fluorine-doped tin oxide (FTO) substrates (7 ohm per square) were etched with 2 M HCl and Zn dust to attain the desired pattern. Then, the FTO substrates were cleaned serially with Hellmanex solution, deionized water, acetone, IPA, and ethanol in ultrasonication bath, dried with N_2 gas. Then, the TiO_2 blocking layer (bl-TiO_2) was placed on the preheated FTO at 500 °C for 10 min by chromatography spray of titanium diisopropoxide(bisacetylacetonate) solution (549 µL in 10 ml ethanol) and then heated at 500 ^oC for 15 min. Consequently, after cooling, the mesoporous TiO_2 layer (mp-TiO_2) was deposited with a commercial TiO_2 paste in ethanol (weight ratio=1:3.5) at 5,000 rpm for 30 s, and the TiO_2 film was annealed out for 5 min at 100 ^oC and for 30 min at 450 ^oC. After cooling, the m-TiO_2 was doped with lithium using a solution of bis(trifluoromethane)sulfonimide lithium in acetonitrile (20 mg/mL). 150 µL of the solution was spin coated onto the substrates at 3000 rpm for 20 s, and again annealed at 450 °C for 30 min. The perovskites layer was deposited on the substrate by two step deposition method. 1 M $PbBr_2$ solution in DMF was heated to 70 ^oC for half an hour and the glass substrate are also annealed at same temperature for 10 minutes. The $PbBr_2$

layer was spin coated at 2500 rpm for 30 seconds and the film was annealed at 90 ^{o}C for 45 minutes. Afterward, the processed cell was dipped in 50 mM FABr solution in IPA at 60 ^{o}C for 10 minutes. After removing from the solution, the substrate was annealed at 80 ^{o}C for 10 min. The carbon layer was deposited by doctor blading directly on the top of perovskites layer and dried at 70 ^{o}C for 10 min. The silver conductive paint was painted on to the cells to create contact.

2.2 Characterization Methods

The common method used to characterize the sample and devices are outlined below.

2.2.1 Powder X-ray Diffraction

The crystal structure of the materials was analyzed by using X-ray diffraction (XRD) using PANalytical X-ray diffractometer at 45 kV and 40 mA with CuKa (λ=1.54 Å) radiation.

2.2.2 Fourier transform infrared spectra (FTIR)

FTIR study was conducted to investigate the chemical structure of the materials by using BRUKER TEsNSOR-II spectrometer.

2.2.3 X-ray photoelectron spectroscopy (XPS)

XPS analysis was carried out using spectrometer (Thermo Scientific, K-alpha) equipped with monochromatic Al K alpha source operated at 20 mA and 15 kV.

2.2.4 Scanning Electron Microscope (SEM)

SEM was carried out using Thermo Scientific Apreo S microscope.

2.2.5 Transmission Electron Microscopic (TEM) coupled with EDS

The analysis was carried out using TEM, JEOL JEM-2100F high resolution TEM (HRTEM).

2.2.6 UV-Vis Spectroscopy

UV-Vis absorption spectra of the materials were investigated by using UV-Vis Shimadzu 1601 Spectrophotometer.

2.2.7 Photoluminescence (PL) Measurements

Photoluminescence (PL) spectra and kinetics were examined with the help of PicoQuant Fluo Time FT-300 steady-state and time-resolved fluorescence spectrometer that works on time-correlated single photon counting (TCSPC) principle. The samples

were dispersed in toluene and excited with pulsed LED excitation source at 306 nm and the PL was collected at ambient conditions. The PL and TRPL studies of $FAPbBr_3$ perovskite solar cells device was conducted under same condition except using laser excitation source of 400 nm. Absolute PLQYs were collected on a spectrofluorometer (FS5, Edinburgh, UK) equipped with a 15 cm integrating sphere and Xenon lamp as a source of light.

2.2.8 Band edges estimation

Cyclic Voltammetry (CV) was carried out to find band edges by electrochemical workstation (CH166B). The CV was performed in three electrode system using platinum as counter electrode, glassy carbon as a working electrode, and reference of silver wire in non-aqueous acetonitrile: toluene (4:1) solution in $TBAPF_6$ supporting electrolyte. The electrochemistry and UV-Vis were used to work out the band energies of the graphene, its derivatives, and the perovskites. The method used works well if electrons are excited from the HOMO to the LUMO in the UV-Vis and the excited state is not at higher energy.

2.2.9 J-V measurements of the solar devices

The J-V data of the perovskites-carbon paste-based devices was collected by using the solar simulator of Class AAA, equipped with HMI Lamp (200 W/ 70 V) under 1 sun light intensity AM 1.5, and a potentiostat Keithley 2601. Incident photon to current efficiency (IPCE) measurement were performed with the light source passing through a monochromator. Calibration was performed using a Bentham GaAs reference photodiode (818-UV-L) and this reference photodiode was used to assist the calculation of the IPCE of the measured device. The IPCE values were calculated by taking the current percent of the device to the photodiode.

2.2.10 Electrochemical Measurements for water splitting

The electrochemical measurements were made using a three-electrode electrochemical system comprising Pt wire as counter and Ag/AgCl as the reference electrode, respectively. Cyclic voltammetry (CV), Linear Sweep Voltammetry (LSV), Chronoamperometry, and open circuit measurements (OCP) of the $FTO|TiO_2|FAPbBr_3|Carbon|$graphite sheet modified with water oxidation catalyst (GSWOC) photoelectrodes by using Ivium potentiostat under simulated solar irradiation of AM 1.5 G with a 100 W Xe lamp light source. CVs and LSVs were

accomplished at a scan rate of 50 mV s^{-1}. The electrolyte medium comprised 0.1 M KNO_3 solution, adjusted to pH 2.5 using HNO_3. The Open Circuit Potential (OCP) was measured by setting the 0 current flowing through the system. The photo-voltage was calculated by subtracting the OCP value measured in the dark from the OCP value measured under 1 sun illumination (AM 1.5 G filtered, 100 mW cm^{-2}).

2.2.11 Electrochemical Impedance spectroscopy (EIS)

EIS of NCs and NCs-Gr heterostructures in solution were measured by CH1660B electrochemistry setup. The EIS spectra were recorded at a frequency range from 0.1 Hz to 100 kHz under similar conditions to CV measurements.

3. Results and Discussion

This section of the thesis is comprised of four sub-sections. The first three sub-section describe the characterization and charge transfer studies of different heterostructures containing inorganic and organic-inorganic perovskites coupled with graphene and functionalized graphene. While sub-section 4 describes the fabrication and photoelectrochemical water oxidation studies of $FAPbBr_3$ based solar cell.

3.1 Photon-induced Electron Transfer in Ligand Stabilized Monoclinic $CsPbBr_3$ and Alanine Functionalized Graphene Heterostructures

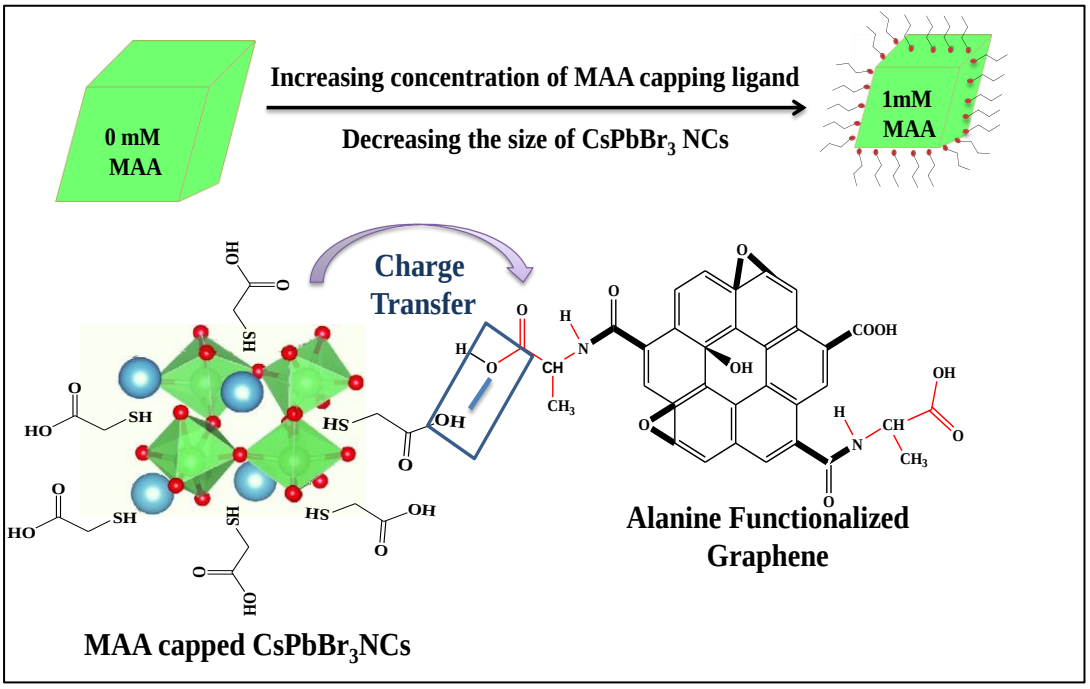

This section presents the heterostructures that consist of mercaptoacetic acid (MAA) functionalized $CsPbBr_3$ NCs and alanine functionalized graphene (N-Gr). The surface functionalization of the $CsPbBr_3$ NCs and graphene enables an effective attachment of the NCs and the graphene. The use of MAA as functionalizing ligand not only passivates the surface of NCs, but it also provides the possibility of tuning the size of NCs and further coupling with the alanine functionalized graphene. By varying the amount of MAA, it allows to synthesize the brightest $CsPbBr_3$ NCs with absolute photoluminescence quantum yield (PLQY) of 49% and emission spectral width of 25 nm. By combining the alanine functionalized graphene, the photoluminescence (PL)

quenching of the NCs has been observed. The photoexcited charge transfer from NCs to alanine functionalized graphene is responsible for the occurrence of PL quenching that is advocated by time resolved photoluminescence (TRPL) studies and cyclic voltammetry (CV) analysis. Our work provides a method to control the energetics and to analyze the types of charge transfer in functionalized perovskite NCs and graphene heterostructures and motivates to further research about the basic knowledge of charge transfer in functionalized donor-acceptor heterostructures.

3.1.1 Characterization of functionalized graphene

3.1.1.1 Powder XRD analysis of graphene oxide (GO) and alanine functionalized graphene (N-Gr)

The Powder XRD patterns of as-prepared GO and N-Gr are presented in figure 3.1.1(a). The transformation of graphite into GO display a peak positioning at $2\theta = 10.45^{\circ}$, consistent to the (011) plane of GO and it specifies the presence of oxygen containing moieties related to the inter-planer spacing d = 10.76 Å of GO.[154] Strangely, this peak vanished in the case of N-Gr, and a new broad peak positioned at $2\theta = 26.06^{\circ}$ appeared, corresponding to the (002) graphitic plane, signifying a high degree of reduction after treatment of alanine with GO due to the amino functionalization on the surface of GO. The shifting of peak in powder XRD patterns of N-Gr to a higher diffraction angle as compared to GO, represents a decrease in the inter-planar spacing to 3.37 Å, thus agreeing to Bragg's law ($2d \sin\theta = n\lambda$). The XRD pattern has shown that N-Gr adopted a specific crystal structure between those of GO and graphite. This can be related with the highly random arrangement of nitrogen-containing moieties of alanine on the surface of graphene sheets. It is important that the N-Gr XRD pattern reveals that the graphene sheets are in a significantly exfoliated form and do not assemble upon functionalization of alanine on GO.

3.1.1.2 FTIR analysis of GO and alanine functionalized graphene (N-Gr)

FTIR analysis was used to understand the bonding interactions in GO and alanine functionalized graphene. In GO spectrum, all the relevant signals of oxygen containing functional groups are observed, that confirms the successful transformation of graphite to GO. In the FTIR spectrum of the GO that is displayed in figure 3.1.1(b), strong absorption signals around 3300, 1718, 1500 cm^{-1} were observed because of the

vibration modes of –OH, C–O present in COOH and C–O–C (epoxy), correspondingly.[155] After functionalization of GO, the reduction in signals of the oxygen containing groups of GO confirms the functionalization of GO. The wide peak at 3300–3500 cm^{-1} can be assigned to the N–H stretching vibration of the amine groups with less intensity and symmetric peak shape. The band of N-Gr can be found at 1415 cm^{-1} is assigned to the –CN stretching vibrations. Moreover, the band appeared at 871 cm^{-1} can be assigned to the asymmetric stretching vibrations of the –NH moiety. These results suggest the successful functionalization of GO with alanine.[151, 152] In table 3.1.1 the observed peaks in FTIR spectra of GO and N-Gr are summarized.

Table 3.1.1 Observed vibrational modes in GO and N-Gr.

Mode of Vibration	**Observed Peak (cm^{-1})**
Stretching vibration of O-H and -NH group	3300
Stretching vibrations of C=O	1718
Bending vibrations of C=O	1017
Stretching vibration of C=O	1590
asymmetric $–NH_2$ stretching	871

3.1.1.3 UV-Vis spectroscopy

UV-Vis absorption studies were carried out to investigate the effect of functionalization on the optical properties of GO with alanine (figure 3.1.1(c)). In the absorption spectrum of GO, two absorption peaks centering at 230 nm and 291 nm are observed. The peak at 230 nm is ascribed to the π-π^* transition of carbon-carbon double bond and the other shoulder peak at 291 nm is assigned to π-π^* transition of the carbonyl group of GO, these agree with the literature.[157] The distinct absorption peaks disappear in the spectrum of alanine functionalized graphene and a broad range peak is observed. The difference in absorption spectrum indicates that the GO is functionalized and have various moieties on the surface i.e. -COOH, $-NH_2$, -OH. Presence of these functionalities not only shifts the absorption spectrum but also induce the peak broadening of N-Gr. These findings agree to the previous report.[158]

3.1.1.4 Raman analysis of GO and N-Gr

The Raman spectra of GO and N-Gr are displayed in figure 3.1.1(d). In the Raman spectrum of GO a peak centered at 1597 cm^{-1} is observed (G band) that corresponds to the E_{2g} phonon of the sp^2 hybridized carbon, and another peak centering at 1350 cm^{-1} (D band) results from the breathing mode of κ-point phonons of A_{1g} symmetry. In case of N-Gr the G-band is centered at 1605 cm^{-1} that is slightly shifted from the G band of GO. The ratio of the intensity of these bands (I_D/I_G) indicates the quality of the product. The I_D/I_G increases from 0.74 to 0.98. The difference represents that the defects increases while transformation from GO to N-Gr. Because presence of amino group on the surface of graphene reduces the symmetry and number of graphene layers.[159, 160] The intensity of peaks is greatly increased during transformation from GO to N-Gr indicating an improvement in the crystallinity during this process.

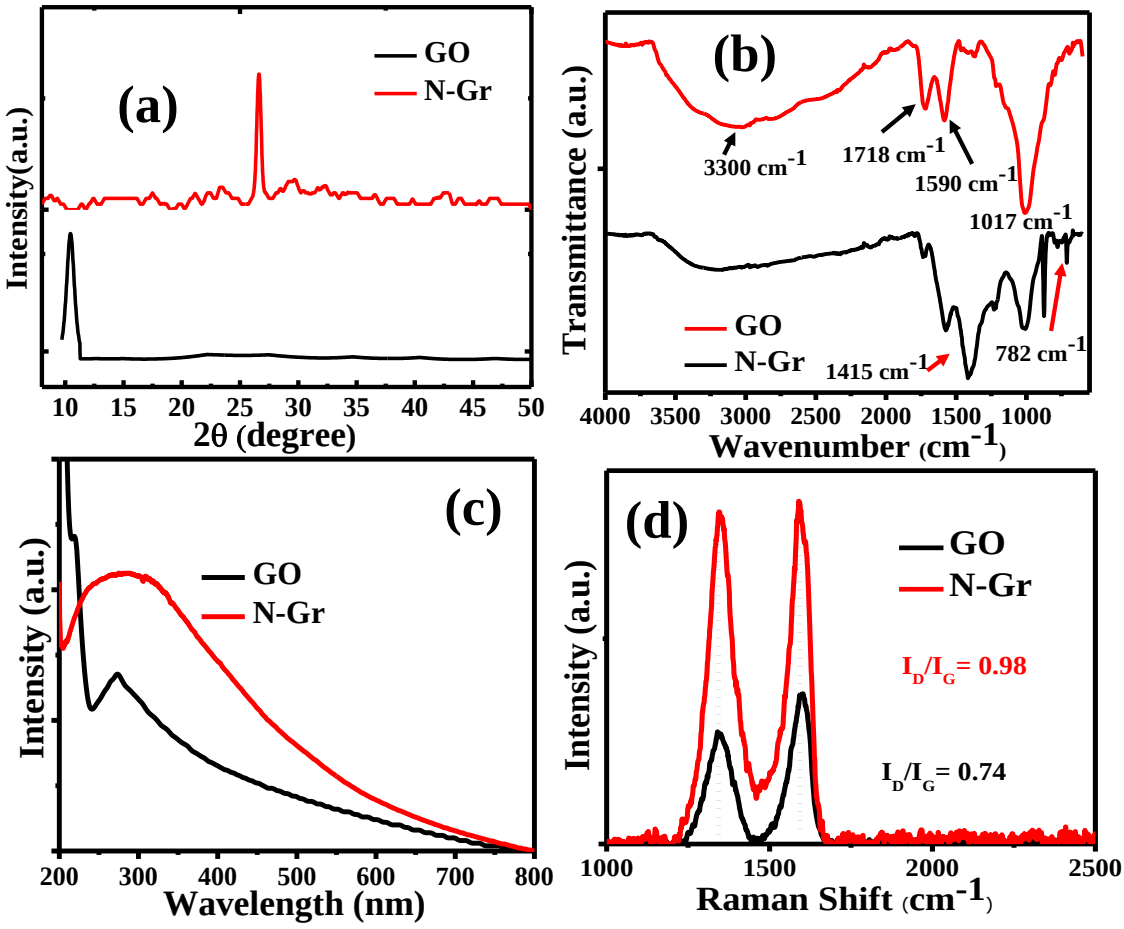

Figure 3.1.1 (a) XRD patterns, (b) FTIR, (c) UV-Vis absorption and (d) Raman spectra of GO and N-Gr.

3.1.2 Characterization of $CsPbBr_3$ NCs

3.1.2.1 Structural, morphological, and chemical analysis of the NCs

To discern the effect of MAA ligand concentration on the crystallinity of the $CsPbBr_3$ NCs, powder XRD analysis was employed. The XRD pattern of the synthesized 0.5 mM MAA functionalized $CsPbBr_3$ NCs along with reference card is displayed in figure 3.1.2 (a). The XRD patterns of the remaining samples containing MAA concentration 0.25 mM, 0.75 mM and 1 mM are presented in figure 3.1.3 (a). The XRD pattern of the NCs is well indexed and in agreement with the monoclinic crystal structure of the $CsPbBr_3$ NCs (standard ICSD card no. 00-018-0364).[161] The monoclinic phase of the NCs is a metastable phase whose formation can be controlled thermodynamically. The presence of MAA functionalizing ligand on the surface of NCs is responsible for the existence of monoclinic metastable phase at room temperature, which lowers the surface energy and facilitates the formation of monoclinic $CsPbBr_3$ NCs.[162] By comparative analysis of XRD patterns of NCs synthesized with increasing concentration of MAA reveals that the monoclinic phase is retained in all synthesized NCs but crystallite size decreases (XRD peaks become broader and less intense) indicating that the size of the NCs decreases with increasing concentration of capping ligand, figure 3.1.3 (a). The morphology, lattice structure and size of the synthesized perovskites NCs were analyzed by employing SEM, TEM, and HRTEM analysis. Figure 3.1.2 (b-c) display the SEM and TEM images of 0.5 mM MAA capped NCs. The SEM images represent the synthesized NCs are of homogeneous morphology. The HRTEM micrograph (figure 3.1.2 (d)) depicts the high crystallinity of monoclinic phase of $CsPbBr_3$ of NCs. It indicates the lattice fringes with spacing of 0.29 nm resulted from (111) crystal plane of monoclinic phase.[163] Selected area electron diffraction (SAED) also confirms the crystalline phase of synthesized NCs in addition to some defects that appear in the form of faint rings (inset of figure 3.1.2 (d)). The appearance of (200) crystalline plane in SAED also confirms the monoclinic crystalline phase of $CsPbBr_3$ NCs.[164] These results are in good agreement with the findings that are predicted by XRD.

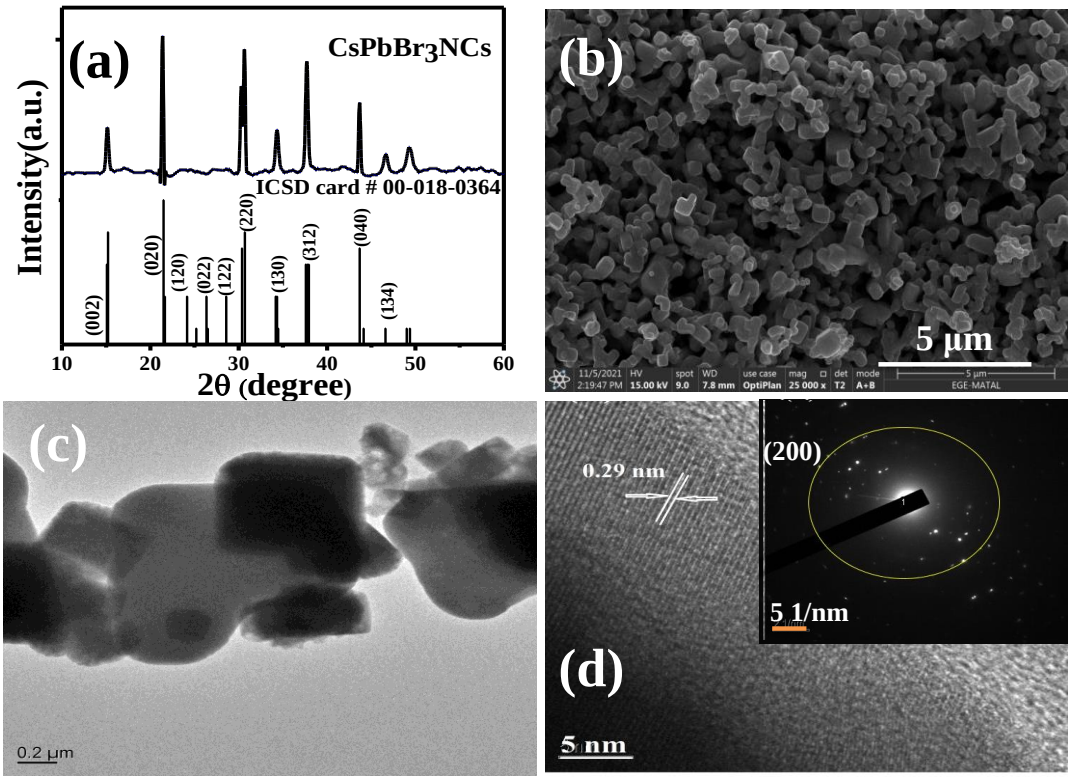

Figure 3.1.2 (a) XRD pattern, (b) SEM micrograph, (c) TEM micrograph, and (d) High-resolution TEM micrograph of 0.5 mM MAA capped $CsPbBr_3$ NCs (inset showing the SAED pattern of NCs).

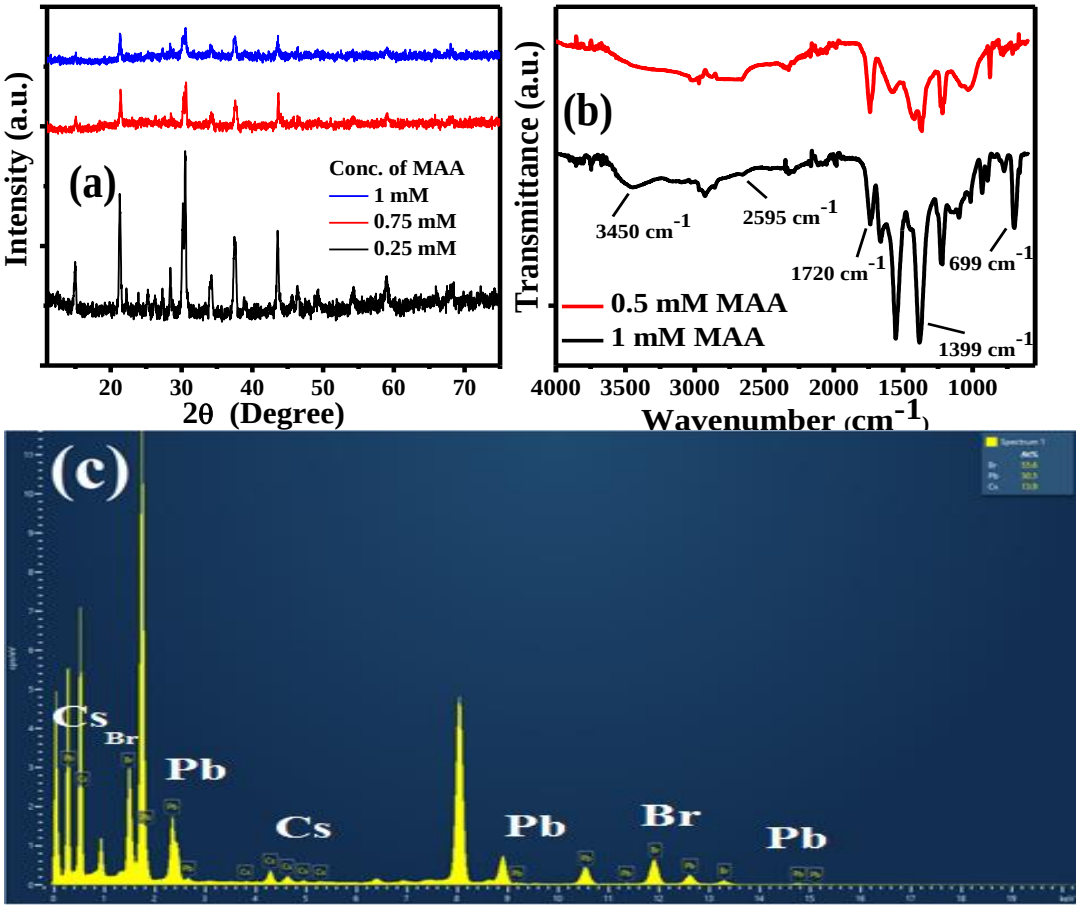

Figure 3.1.3 (a) XRD patterns, (b) FTIR spectra (c) EDX spectrum of 0.5 mM MAA functionalized $CsPbBr_3$ NCs.

Chemical composition of the MAA functionalized $CsPbBr_3$ NCs were analyzed by performing FTIR and XPS analysis. Figure (3.1.3 (b)) shows the FTIR spectrum of MAA functionalized $CsPbBr_3$ NCs. The FTIR analysis confirmed the stabilization of the NCs by thiol group of the MAA. A band feature occurring around ~700 cm^{-1} can be assigned to metal bromide vibrational mode of $CsPbBr_3$ NCs. A wide peak at 3450 cm^{-1} appeared due to stretching mode of O-H of MAA. The characteristics peaks occurring at 1720 cm^{-1}, 1651cm^{-1} and 1399 cm^{-1} can be attributed to C=O stretching and $–CH_2$ bending vibrational modes of MAA, respectively. The peaks in the range of 1000-1300 cm^{-1} can be ascribed to C-O stretching vibrational modes. Amongst the three functional moieties of MAA that may be involved in functionalizing the NCs i.e., O-H, S-H, and C=O, only the S-H peak in the range of 2569 cm^{-1} was shifted to 2595 cm^{-1} in the FTIR spectrum confirming the involvement of S-H group in the functionalized $CsPbBr_3$ NCs.[165, 166]

The EDX analysis of 0.5 mM MAA functionalized $CsPbBr_3$ NCs is presented in figure 3.1.3 (c). The analysis represents the peaks of main constituent elements present in the NCs and confirms the presence of Cs, Pb and Br in $CsPbBr_3$ NCs. For chemical states determination of the elements and to get insight into the role of MAA ligand, XPS spectra is recorded and displayed in figure 3.1.4. The XPS survey spectrum of the MAA functionalized NCs is displayed in figure 3.1.4 (a) and it confirms the presence of Cs, Pb, Br, S and O signals. The signals of Sulphur and Oxygen are derived from MAA capping ligand. The XPS spectrum of the Cs (Figure 3.1.4 (b)) displays two peaks of Cs $3d_{5/2}$ and Cs $3d_{3/2,}$ observed at 724.4 eV and 738.1 eV, respectively. These peaks originate from spin-orbit splitting and confirm the +1-valence state of the Cs in $CsPbBr_3$ NCs. For Br^- (Figure 3.1.4 (c)) two peaks are observed, the higher band energy region (observed at 70.28 eV) corresponds to $3d_{3/2}$ and lower band energy region (observed at 69.38 eV) corresponds to $3d_{5/2}$ states, respectively. The observed peak positions of Cs and Br agree with the previously reported results.[167,168] The Pb^{2+} (Figure 3.1.4 (d)) in $CsPbBr_3$ NCs exist with two chemical surroundings, the higher and the lower band energy region that can be assigned to the Pb-MAA and Pb-Br complexes respectively. Mi et al.[169] reported a detailed studies on the effect of S^{2-}coordination on the XPS spectrum of the Pb (4f). By comparing the XPS spectra of hybrid perovskites and S^- binding hybrid perovskite, it explains that the presence of Pb–S linkage slightly shifted the 4f peak of the Pb-element toward lower binding. Our findings are in well agreement with the findings reported by Mi et al.,[169] deducing that the combination of surface Pb atoms and S^{2-} ions are responsible for the shift of Pb 4f peak position. For instance, the $4f_{7/2}$ and $4f_{5/2}$ peaks for Pb-Br is observed at higher binding energies (139 eV & 144 eV) and for Pb-S both peaks of lead element are observed at lower binding energies (138.6 eV & 143.5 eV). The peak positions of S 2p (Figure 3.1.4 (e)) also supports this supposition. The XPS spectral response in the S 2p region (Figure 3.1.4 (e)) is a spin-orbit doublet with each component separated by 1.2 eV. Two S $2p_{3/2}$ and S $2p_{1/2}$ doublets are observed in core level XPS spectra of S. The S is present in two different chemical environments. The first duplet at 164.58 and 165.68 eV can be assigned to the S of MAA adsorbed to the surface of NCs, which are not fully coordinated with Pb. The second S 2p response in the observed spectra is located at 170.18 and 171.28 eV and it may be assigned to the fully coordinated S to the dangling Pb^{2+} coordination bond. Tchaplyguine et al.[170] studied the inside and outside chemical arrangement of metal-encapsulated PbS nanoparticles and observed that the shift towards higher energy i.e.,

from 169 to ~170 eV is due to S-rich surface of metal-S linkage of the NCs. Indeed, the MAA solution possesses large number of S^{2-} ions, which form a sulfur-rich surface around the $CsPbBr_3$ NCs, thus resulting the shifting of S 2p peak position to ~170 eV. From the above findings, it can be deduced that S^{2-} ions would attach to the NCs by coordinating the hanging Pb^{2+} bonds. For oxygen 1s (Figure 3.1.4 (f)) two peaks in XPS spectra are observed that can be attributed to the carboxylate moiety of the MAA. The observed peaks (deconvoluted blue and green traces) centering at 532.2 eV and 533.3 eV are designated to the C=O and C–O groups of MAA.[171]

Based on FTIR and XPS analysis, we can deduce that the S^{2-} of the MAA is involved in capping the NCs through -SH moiety of MAA as reported previously in the case of QDs.[172]

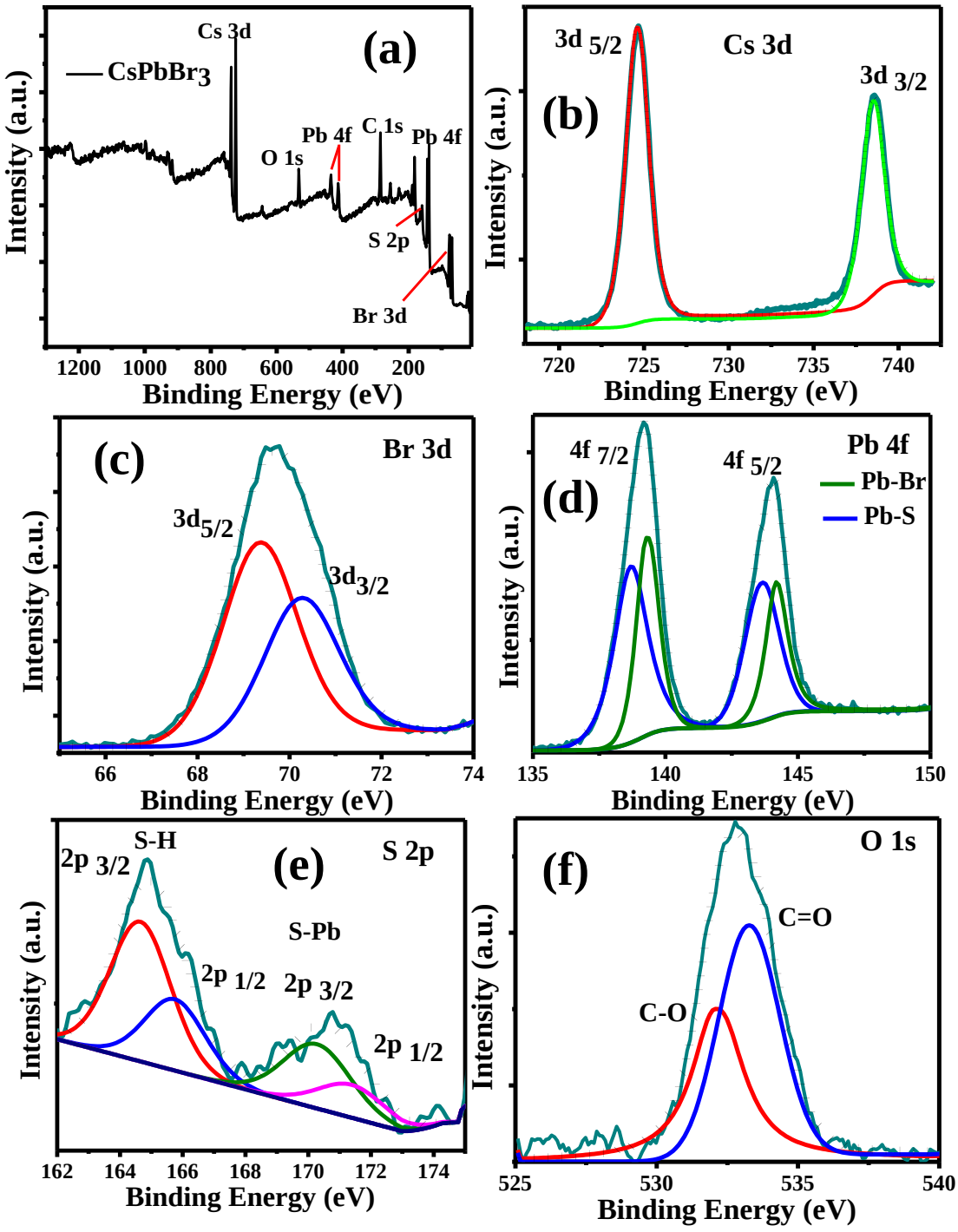

Figure 3.1.4 XPS analysis (a) Survey spectrum of $CsPbBr_3$ NCs, (b) Cs 3d spectrum, (c) Br 3d spectrum, (d) Pb 4f spectrum, (e) S 2p spectrum and (f) O 1s spectrum. Solid red lines indicate the experimental data and black filled circles represent the best fits.

The elemental composition obtained from EDX and XPS analysis of synthesized $CsPbBr_3$ NCs also confirms the atomic ratio of Cs:Pb:Br is 1:1:3 in as synthesized perovskites NCs, which was closed to the theoretical value as displayed in table 3.1.2.

Table 3.1.2 Percentage of elements observed in EDX and XPS analysis.

Element (%)	Cs	Pb	Br
EDX	20.21	19.91	59.88
XPS	20.10	20.80	59.10

3.1.2.2 UV-Vis absorption and PL analysis of NCs

The UV-Vis and PL spectra of the $CsPbBr_3$ perovskite NCs synthesized by using various concentrations of MAA functionalizing ligand are displayed in figure 3.1.5. To compare the effect of ligand on the optical properties of $CsPbBr_3$ perovskite NCs, $CsPbBr_3$ perovskite was also synthesized, and their absorption and PL spectra are displayed in figure 3.1.6 (a) and the respective tauc plot in figure 3.1.6 (b). The absorption edge of $CsPbBr_3$ perovskite appeared at 518 nm (2.39 eV) and the PL peak was centered at 529 (2.34 eV), respectively. For 0.25 mM, 0.5 mM, 0.75 mM, and 1 mM MAA concentrations, the absorption edges appeared at 498 nm (2.48 eV), 481 nm (2.57 eV), 467 nm (2.65 eV), and 454 nm (2.73 eV), respectively. With an increasing amount of MAA capping ligand, a blue shift in the absorption edge was observed that can be attributed to quantum confinement effect i.e., an increase of MAA concentration decreases the size of the NCs. The quantum confinement effect occurs if the size of the crystallites is comparable to or less than the exciton Bohr radius in the bulk material, as observed by Levchuk et al.,[173] in the $FAPbBr_3$ nanoplatelets. In our case, the TEM image suggests that the NCs exist in the form of nanoplatelets with a thickness comparable to the exciton Bohr's radius. Increasing the concentration of MAA decreases the thickness of nanoplatelets, which causes a blue shift in the absorbance and PL spectra. The PL spectra display Stokes-shifted peaks locating at 519 nm, 500 nm, 478 nm, and 465 nm for 0.25 mM, 0.5 mM, 0.75 mM, and 1 mM MAA concentrations, respectively, exhibiting the mirror images of absorption spectra.

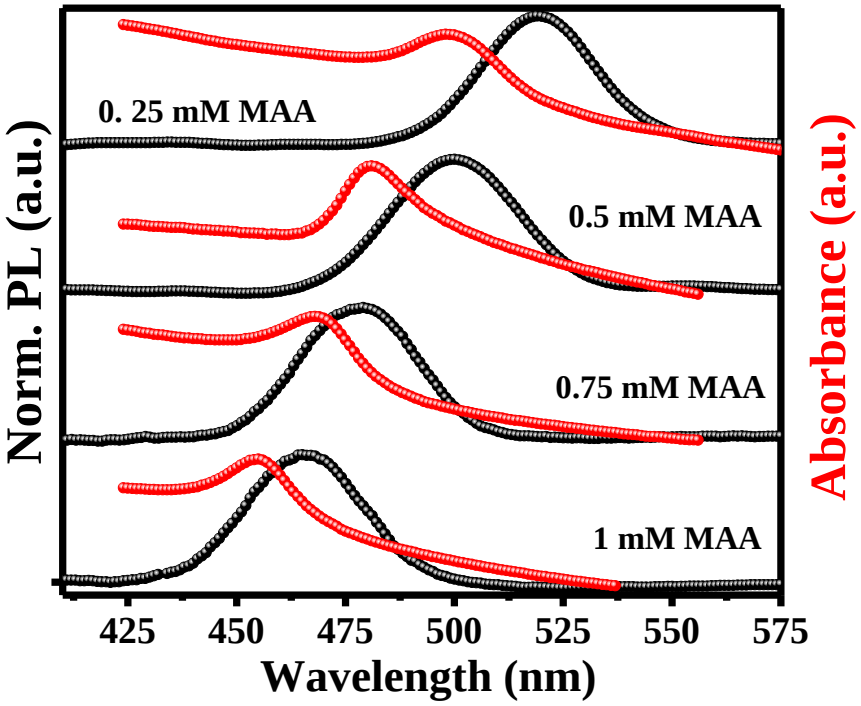

Figure 3.1.5 Absorption and normalized PL spectra of $CsPbBr_3$ NCs synthesized using various conc. of MAA.

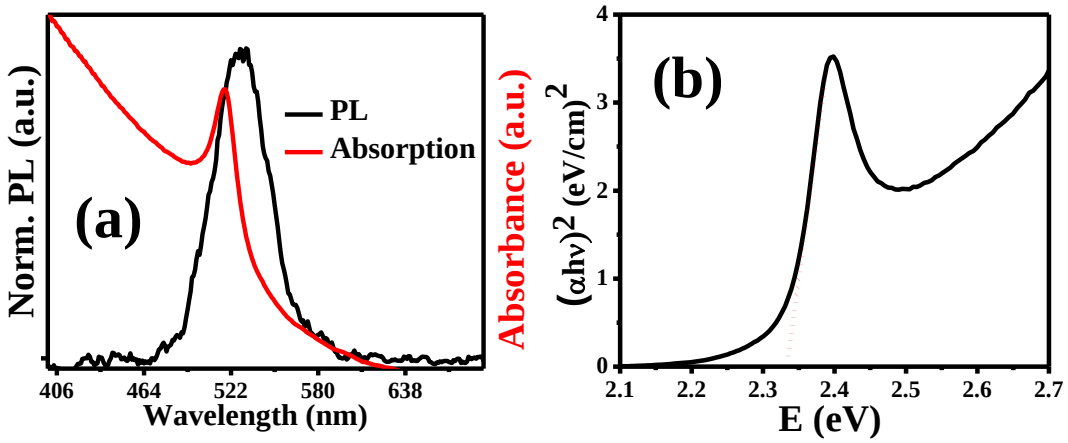

Figure 3.1.6 Absorption and normalized PL spectrum and (b) Tauc plot of $CsPbBr_3$ without MAA.

The absorption and PL of the NCs are varied from 2.48 to 2.73 eV and 2.38 to 2.66 eV, respectively. The MAA concentration dependent stokes-shift in the PL spectra of the NCs is observed because of the variable size of prepared NCs. The Stokes shifts in the PL spectra depend upon the phase, size and defects of the NCs. The values of full-width at half-maximum (FWHM) of PL peaks was also evaluated for NCs and tabulated at table 3.1.3. The FWHM of the PL peaks ranges from 24 to 32 nm depending upon size

distribution of NCs. The absolute photoluminescence quantum yields (PLQY) of synthesized perovskites are also estimated and tabulated in table 3.1.3. It is clearly seen that the PLQY greatly improved from 3.5% to 49% by the addition of MAA ligand during the synthesis of NCs as compared to the reference $CsPbBr_3$ perovskite that was synthesized in the absence of MAA. The optical absorption and the emission parameters of the synthesized NCs with variable amount of MAA are tabulated in table 3.1.3. By comparing these parameters, we can assess that 0.5 mM concentration of MAA delivers the brightest $CsPbBr_3$ NCs with narrow emission line width and high absolute PLQY. The higher concentration of functionalizing ligand enhances surface trap states that results in reduction of PL intensity and enhance peak broadening that is an indication of presence of trap states in the perovskite.

Table 3.1.3 Optical properties of MAA functionalized $CsPbBr_3$ perovskites NCs.

Conc. of MAA (mM)	**λ_{max} of absorption (nm)**	**λ_{max} of PL (nm)**	**FWHM (nm)**	**Absolute PLQY**
0	517	529	42	3.51
0.25	498	519	32	30.14
0.50	481	500	25	49.11
0.75	468	478	30	32.43
1.00	455	465	28	29.32

Figure 3.1.7 (a) shows the schematic illustration of the variation of size of monoclinic $CsPbBr_3$ NCs by increasing concentration of MAA ligand. Figure 3.1.7 (b) represents Tauc plots[173] of the $CsPbBr_3$ perovskite NCs. The $CsPbBr_3$ perovskite NCs synthesized with different MAA concentration possessed an optical bandgap of 2.38–2.62 eV, and their optical bandgap increased with increasing the concentration of MAA as compared to the reference sample.

3.1.2.3 PL decay kinetics analysis of NCs

To get insight into the role of MAA functionalization on the PL lifetime of the $CsPbBr_3$ perovskite NCs, PL kinetics analysis was performed at room temperature. The

PL lifetimes were extracted by fitting the experimental PL decay kinetics bi-exponential decay model, as given in equation (1).

$$\boldsymbol{A\,(t) = \; A_1\, e^{(-t/\tau 1)} \; + \; A_2\, e^{(-t/\tau 2)}} \qquad \textbf{(1)}$$

Where τ_1 *and* τ_2 are the fast and slow components of PL lifetime, and A_1 and A_2 are the weighting coefficients. The shorter PL lifetime component (τ_1) is associated with shallow trap-assisted recombination of the charge carrier, while the lifetime of longer decay component (τ_2) can be associated with recombination time of the charge carriers. The average PL decay time is calculated by using the relation displayed in equation (2).

$$\boldsymbol{\tau_{average} = \frac{A_1\,\tau_1 + A_2\,\tau_2}{A_1 + A_2}} \qquad \textbf{(2)}$$

The comparison of PL decay kinetics of plain $CsPbBr_3$ perovskite and functionalized with various concentrations of MAA capping ligand is displayed in figure 3.1.7 (c) and the data extracted from the decay kinetics by model fitting and $\boldsymbol{\tau_{average}}$ is tabulated in table 3.1.4. The $\tau_{average}$ values of all the functionalized NCs were greatly improved (2.38, 7.26, 3.5, 6.1 ns for 0.25, 0.5, 0.75, 1 m M MAA functionalized NCs) as compared to the reference $CsPbBr_3$ sample (1.37 ns) indicating that the MAA functionalizing ligand can effectively be used, for not only to tune the size of NCs but for also an effective passivation of the surface trapes states of the NCs. An excess amount of capping ligand (conc. > 0.5 mM) increases the number density of surface trap states and the photoexcited charge carrier are trapped in these traps [170] hence a decreased in average PL lifetime is observed.

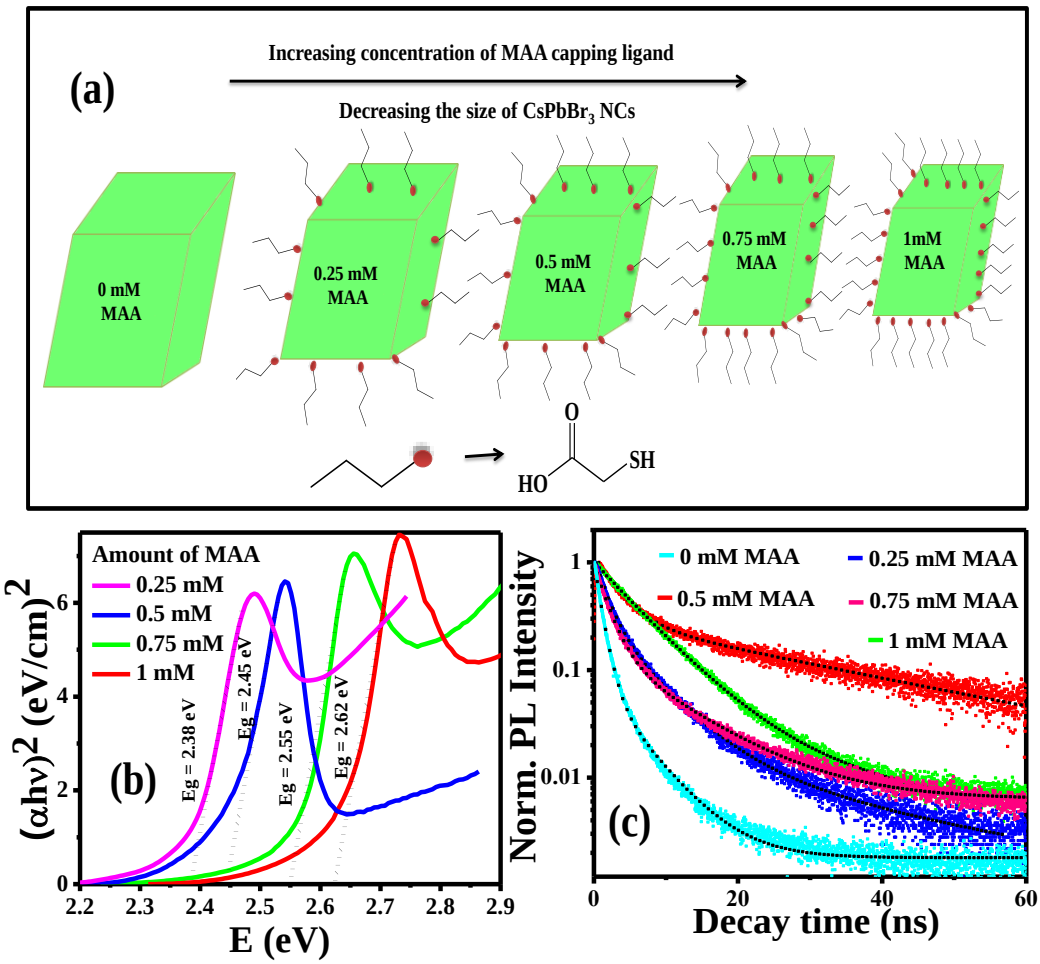

Figure 3.1.7 Schematic representation displaying the decrease in the particle size with increase in amount of MAA capping ligand (b) Tauc plot (c) PL decay kinetics of $CsPbBr_3$ NCs containing various MAA concentrations.

Table 3.1.4 The PL decay kinetics parameters of $CsPbBr_3$ NCs.

Conc. of MAA (mM)	A_1	τ_1 (ns)	A_2	τ_2 (ns)	Average PL time (ns)
0	0.90	0.90	0.10	5.64	1.37
0.25	0.84	1.49	0.16	6.8	2.38
0.5	0.79	3.32	0.21	21.80	7.26
0.75	0.70	2.90	0.30	4.95	3.5
1.00	0.83	2.98	0.17	21.47	6.1

3.1.3 PL quenching studies of NCs/N-Gr heterostructures

The steady-state PL of 0.5 mM MAA functionalized NCs using variable concentration of N-Gr heterostructures is conducted to study the effect of N-Gr on the PL of NCs as displayed in figure 3.1.8 (a). The concentration of 0.5 mM MAA capped $CsPbBr_3$ NCs is kept constant, and different amount of N-Gr (0-60 mg/mL) is added successively to prepare the heterostructures. The PL intensity gradually decreases as depicted in the figure 3.1.8 (a). These results indicate that the N-Gr can effectively act as a quencher of the excited state of the NCs. A reduction in PL intensity advocates that the interaction of NCs with N-Gr provides charge carriers an alternative pathway instead of recombination. The PL quenching is normally attributed to a non-radiative energy transfer or charge transfer (CT) from donor to acceptor. The overlap of the wave function of the donor and acceptor states is the prerequisite for charge (electron or hole) transfer between donor and acceptor. As a result of CT, the decrease in emission intensity of the donor and an increase emission intensity of acceptor is generally observed. The decrease in PL intensity of NCs is observed in our system, figure 3.1.8 (a), but because of the non-emissive nature of the N-Gr, no signal is obtained in the PL spectrum of N-Gr (Figure 3.1.9). These results demonstrate that the NCs act as donor in $CsPbBr_3$ NCs/N-Gr heterostructures. Due to poor overlap of the emission spectrum of the donor ($CsPbBr_3$ NCs) and absorption spectrum of the acceptor (N-Gr) (Figure 3.1.8 (b)), the possibility of energy transfer is minimum, advocating that the charge transfer from NCs to N-Gr is the major process that contribute to the PL quenching of the NCs.[175] Therefore, the photoinduced CT from photoexcited NCs to the N-Gr is the plausible mechanism for the PL quenching of the NCs.

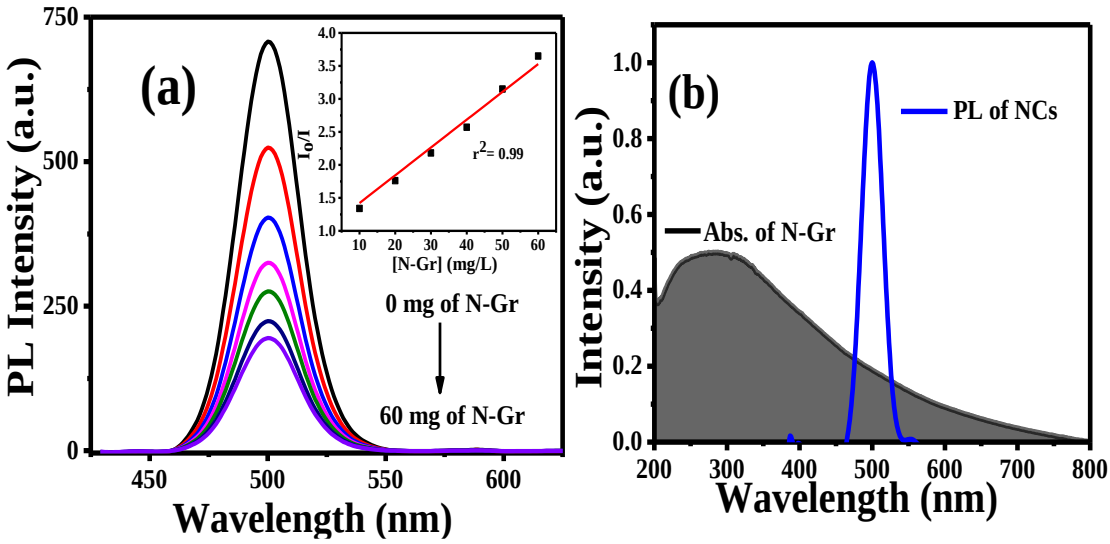

Figure 3.1.8 PL spectra of $CsPbBr_3$ NCs (0.5 mM MAA) and $CsPbBr_3$ NCs/N-Gr heterostructures in toluene solvent containing various amounts of N-Gr, inset. Stern-Volmer plot, (b) UV-Vis absorption spectrum of N-Gr in water (black line) and PL spectrum of NCs in toluene.

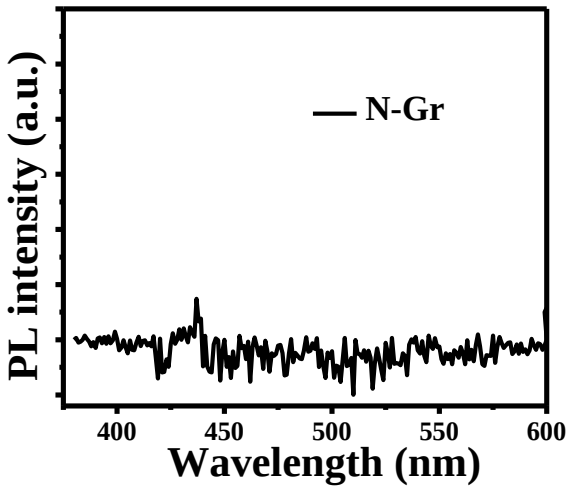

Figure 3.1.9 PL spectrum of N-Gr.

The PL quenching mechanism mainly includes dynamic quenching, static quenching, or combination of both. In static quenching, the PL intensity decreases because of complex formation between quencher and the fluorophore, which possesses little or no PL. In dynamic quenching, the reason for the reduction of PL intensity, is the collision that occurs between quencher and the fluorophore. There is an equal probability of occurrence of combined static and dynamic quenching. To confirm about

the operational static or dynamic PL quenching mode of $CsPbBr_3$ NCs and to get an information about the quenching ability of N-Gr, Stern-Volmer equation[176] (3) was applied.

$$\frac{I_0}{I} = 1 + K_{SV}[Q] \qquad (3)$$

Where I_0 and I represent the steady-state PL intensities of NCs in the absence and presence of N-Gr, respectively; [Q] represents the concentration of N-Gr; and Ksv represents the Stern-Volmer quenching constant. A linear Stern-Volmer plot is depicted in the inset of figure 3.1.8 (a). There is a small deviation from linearity in the Stern-Volmer plot indicating that the static and dynamic mode of quenching mechanisms are operative simultaneously that results in the reduction of PL intensity of NCs. From the slope of the Stern-Volmer plot, the of Ksv was estimated that is 4.5×10^{-2} L/mg for 0.5 m M MAA capped NCs.

To compare the effect of functionalization of NCs and Gr, two heterostructures were prepared in thin film form and their PL and TRPL studies were carried out. The PL and PL decay kinetics of the $CsPbBr_3$ NCs and $CsPbBr_3$ NCs/N-Gr heterostructures are displayed in Figure 3.1.10 (a-b) and the PL and PL decay kinetics of $CsPbBr_3$ perovskites and $CsPbBr_3$ NCs/Graphene ($CsPbBr_3$ NCs/Gr) heterostructures (non-functionalized heterostructures) are displayed in Figure 3.1.10 (c-d) These materials are tested in the form of thin films to check their applicability in optoelectronic devices. Comparatively, more PL quenching is observed in functionalized heterostructures than in non-functionalized one. The calculated $\boldsymbol{\tau}_{average}$ values of $CsPbBr_3$ NCs and $CsPbBr_3$ NCs /N-Gr heterostructures are 7.2 and 4.1 ns, respectively. Similarly, the calculated $\boldsymbol{\tau}_{average}$ values of $CsPbBr_3$ perovskites and $CsPbBr_3$ NCs /Gr heterostructures are 1.37 and 1.21 ns, respectively. With the help of τ_{DA} or $\boldsymbol{\tau}_{(\mathbf{CsPbBr_3+N-Gr})}$ (average PL life time of the donor NCs in the presence of quencher) and τ_D or $\boldsymbol{\tau}_{(\mathbf{CsPbBr_3})}$ (average PL life time of the donor NCs), the rate constant (k_{CT}) and efficiency of charge transfer (E_{CT}) process in both heterostructures is evaluated by using the equation. (4) and (5), respectively.

$$\boldsymbol{E_{CT} = 1 - \frac{\tau_{DA}}{\tau_D}} \qquad \mathbf{(4)}$$

$$\boldsymbol{k_{CT} = \frac{1}{\tau_{(CsPbBr_3+N-Gr)}} - \frac{1}{\tau_{(CsPbBr_3)}}} \qquad \mathbf{(5)}$$

In case of functionalized heterostructures, the k_{CT} and E_{CT} process of heterostructures is evaluated, that is 1.05×10^8 s^{-1} and 43%, respectively, while in non-functionalized

heterostructures, the k_{CT} and E_{CT} process heterostructures is evaluated, that is 9.60×10^7 s^{-1} and 11.67 %. From these results, it is proved that functionalization of NCs and Gr not only essential for the formation of heterostructures but also effective in enhancing charge transfer phenomenon.

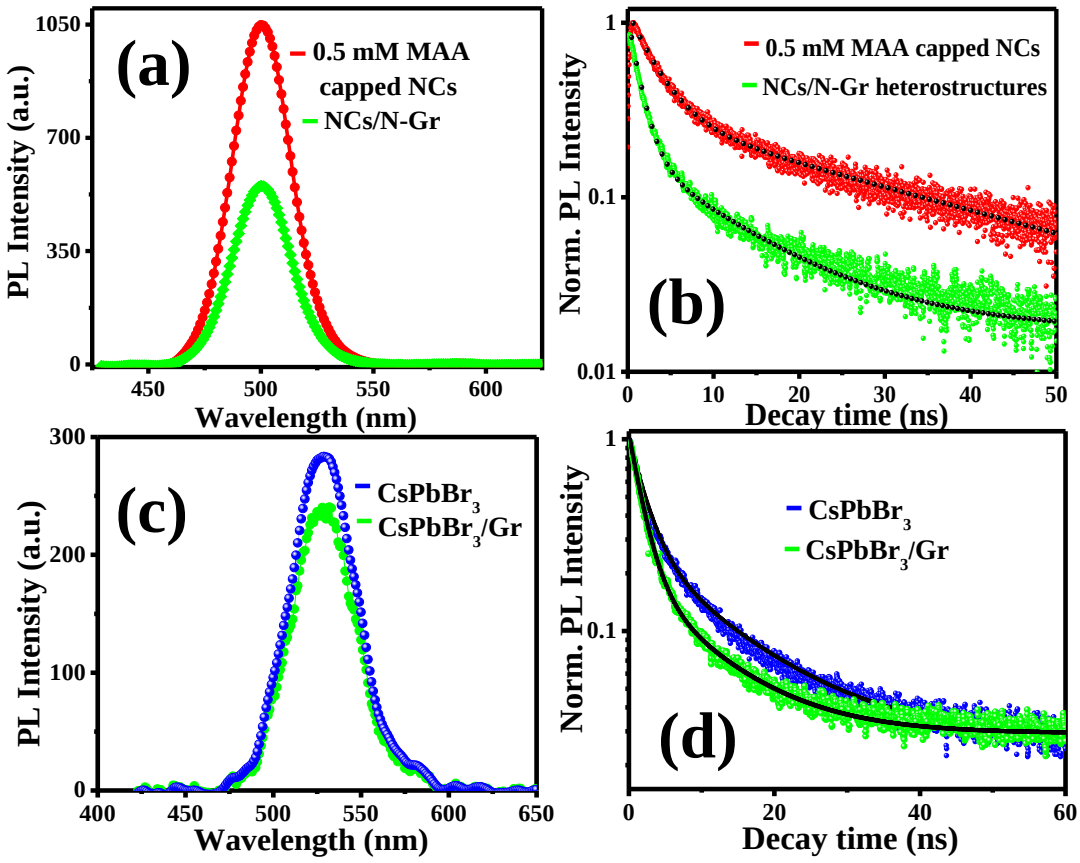

Figure 3.1.10 (a-b) PL and decay kinetics spectra of $CsPbBr_3$ NCs (0.5 mM MAA) and $CsPbBr_3$ NCs/N-Gr heterostructures (c-d) PL and decay kinetics spectra of $CsPbBr_3$ and $CsPbBr_3$/Gr heterostructures.

3.1.4 Cyclic voltametric (CV) analysis of NCs and N-Gr

We used CV for estimating the conduction band maximum (CBM) and the valence band minimum (VBM) of $CsPbBr_3$ NCs. For this purpose, CV was carried out in a mixture of acetonitrile:toluene (1:4 v/v) solvents in Ar gas atmosphere using three electrode system (glassy carbon as working electrode, platinum wire as counter electrode and silver/silver chloride as a reference electrode). Cyclic voltammograms (CVs) were recorded in identical conditions using a 50 mV/s scan rate. Figure 3.1.11(a) represents the CVs of MAA capped NCs. From the reduction onset potentials of NCs

(-0.57 V) obtained from CVs, the CBM and VBM were calculated by using the relation in equations given below.[177]

$$E\ (CB) = -e\ [\ E_{red}^{onset} + 4.4] \qquad (6)$$

$$E\ (VB) = E\ (CB) - E_{0\text{-}0} \qquad (7)$$

Where $E_{0\text{-}0}$ refers to the 0-0 energy that describes as the lowest energy transition, which can be determined from Tauc plot.

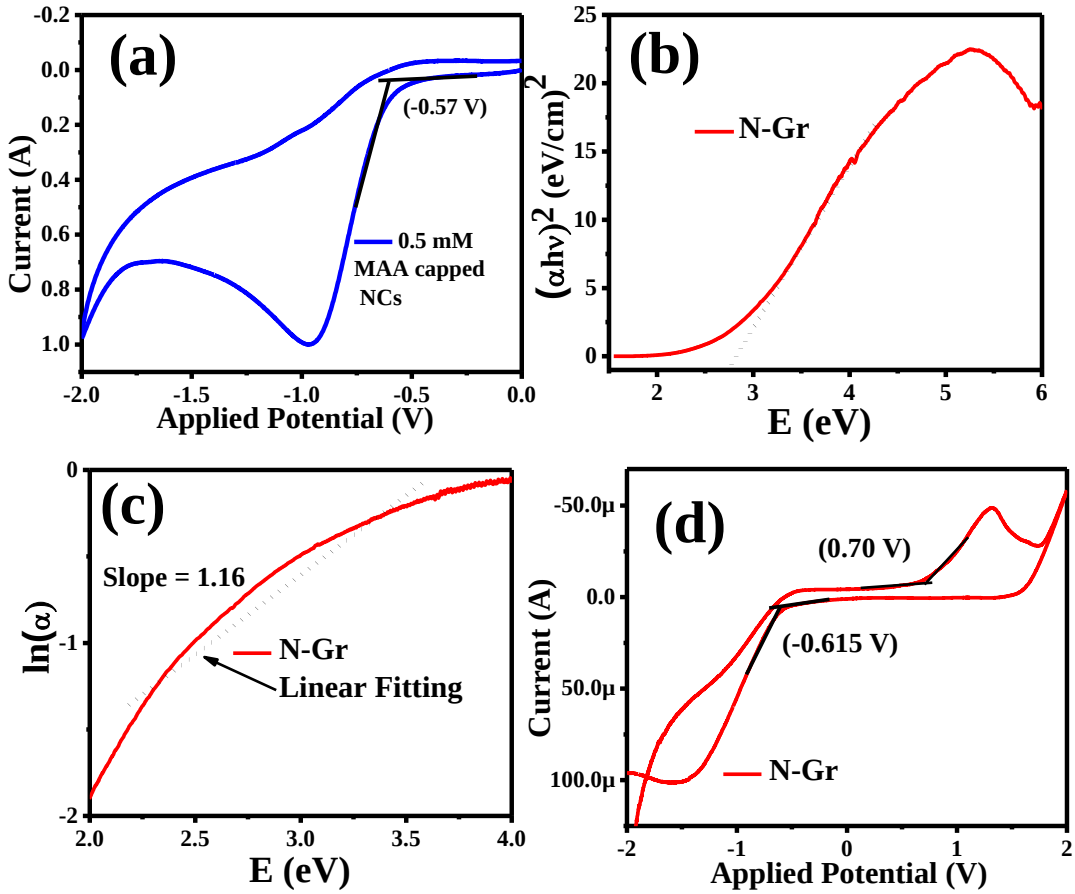

Figure 3.1.11 (a) CVs of NCs (b) Tauc plot of N-Gr (c) ln α vs. hυ plot of N-Gr (d) CVs of N-Gr in 50 mM TBAPF$_6$ in toluene: acetonitrile (4:1) solution.

The Tauc plot of N-Gr is shown in the Figure 3.1.11 (b). The broadening of band gap as indicated in the absorption spectrum of N-Gr is observed in N-Gr that results from sp^2 hybridization of atoms that induced localized states, the presence of band tail lies in the $E_{0\text{-}0=}$ E_{opt} can be conditional. The band broadening in the low energy tail of the absorption spectra is related to the Urbach tail (E_u) by the following equation: $\alpha = \alpha_0 \exp(h\upsilon/ E_u)$. The reciprocal of the slope attained by plotting a graph between ln α vs hυ (Figure 3.1.11(c)) gives the value of E_u that is 1.06 eV. The energy gap (E_g) between

highest occupied molecular orbital (HOMO) and lowest unoccupied molecular orbital (LUMO) of N-Gr can be determined by using an equation $E_{g} = E_{opt} - E_{u.}$ By using the aforementioned relation, the E_g of N-Gr is 1.7 eV. From the onset reduction potential and onset oxidation potential that are observed in the CVs (Figure 3.1.11 (d)) of N-Gr, the value of HOMO and LUMO of N-Gr can be estimated as given below.[178]

$$E_{HOMO} = -e(E_{Ox}^{onset}{}_{vs.NHE} + 4.75)\ (eV) \quad (8)$$

$$E_{LUMO} = -e\ (E_{Red}^{onset}{}_{,\ vs.\ NHE} + 4.75)\ (eV) \quad (9)$$

$$E_{NHE} = E_{Ag/AgCl} + 0.197 \quad (10)$$

The onset reduction and oxidation potentials of N-Gr were estimated to be -0.615 eV and 0.70 eV, respectively. The HOMO and LUMO level of N-Gr are located at -5.65 eV and -3.92 eV, respectively. The value of electrochemical band gap that is determined by the difference of HOMO and LUMO is 1.72 eV that agrees to the value of optical band gap of N-Gr that is 1.7 eV. The conduction band (CB) and valence band (VB) levels of NCs are located at -3.79 eV and -6.24 eV, respectively and the value of electrochemical band gap that is determined by the difference of CB and VB is 2.45 eV that is nearly in agreement to the value of optical band gap of NCs obtained from PL onset wavelength (480 nm) that is 2.57 eV. The positions of VB and CB of MAA functionalized NCs, and HOMO and LUMO of N-Gr are presented in the figure 3.1.12(a). The energy difference of HOMO and LUMO levels of N-Gr is less than the MAA functionalized NCs.

By analyzing the values of band edges of NCs and N-Gr, one can assess in the heterostructure the process of charge transfer can take place from NCs to N-Gr. The small difference, >kT of CB of NCs and LUMO orbital of N-Gr facilitates the electron transfer process from NCs to N-Gr faster. The large energy difference (~0.6 eV) in VB of NCs and HOMO level of N-Gr is making the hole transfer from NCs to N-Gr less favorable than the electron transfer. Thus, the CV measurements suggest that electron transfer process is the dominant process that account for PL quenching of the $CsPbBr_3$ NCs.

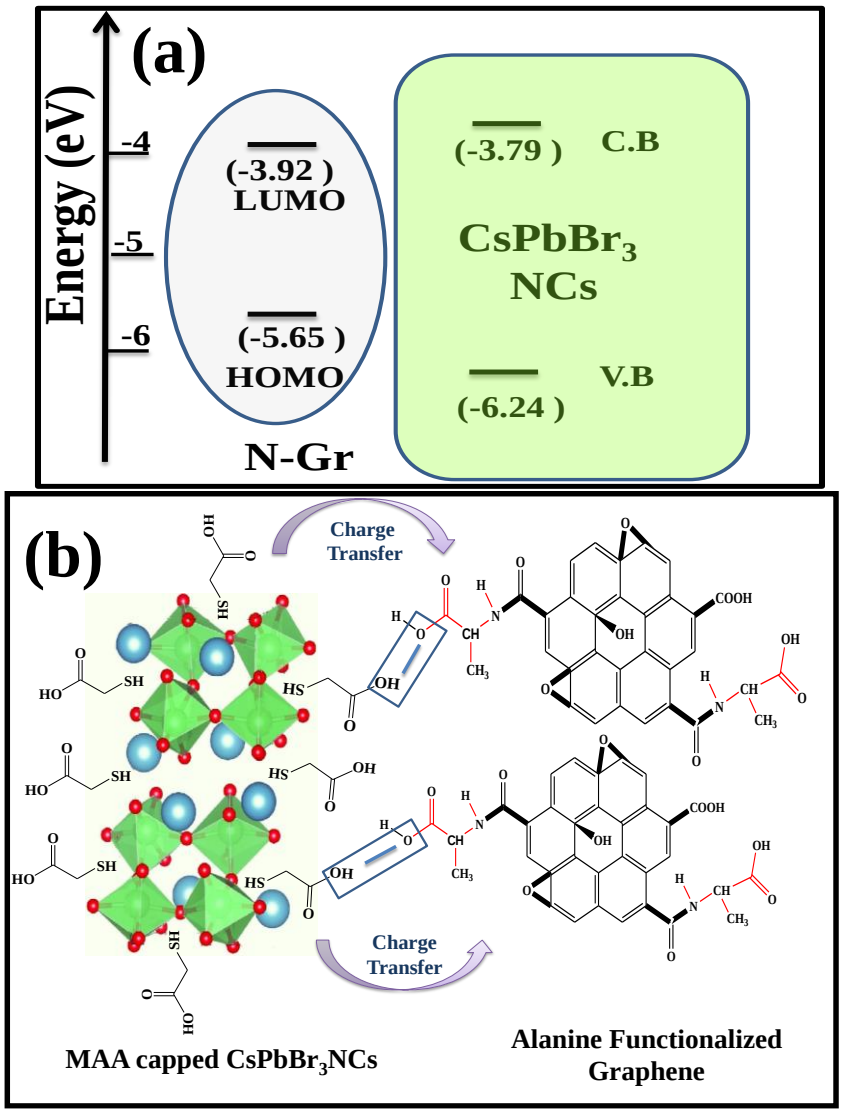

Figure 3.1.12 (a) Band edges of N-Gr and estimated by CV And (b) schematic diagram showing the anchoring of MAA functionalized $CsPbBr_3$ NCs with N-Gr matrix through different terminal functional groups of N-Gr, because of which the phenomenon of charge transfer takes place.

From these findings, we can simply describe the plausible mode of interaction between NCs and N-Gr to form heterostructures is the H-bonding as confirmed by FTIR of the heterostructures and depicted in Figure 3.1.13 (b). An absorption of photons of 306 nm generates excitons in $CsPbBr_3$ perovskites NCs, following their dissociation into free charges, the electrons and holes recombine through inter-band transitions radiatively in the absence of N-Gr that is observed in PL spectrum. When N-Gr interacts with perovskites, a potential is developed at the interface of $CsPbBr_3$ NCs/N-Gr that

leads to the spatial separation of charge carries at the interface, thus preventing the radiative recombination of photoinduced charge carriers. The photoinduced charge carriers are separated effectively at $CsPbBr_3$ NCs /N-Gr interface, thus facilitating the process of CT.[179] In our case, N-Gr develops hydrogen bonding with free tail (-COOH) of MAA with the $-NH_2$, -COOH, -OH, etc. functional moieties of N-Gr that leads to the attachment of N-Gr on the surface of perovskites NCs. These linkages not only prevent charge trapping but also provide a site for charge separation and facilitate the electron transfer from NCs to N-Gr.

3.1.5 Summary

The synthesis of various types of novel MAA functionalized $CsPbBr_3$ NCs advocated that the MAA ligand not only tuned the size of NCs but could also passivate the trapes states as illustrated by PLQY and TRPL studies. By optimizing the concentration of MAA, maximum 49% value of absolute PLQY was achieved. The –SH group of MAA was involved in the surface functionalization of NCs as demonstrated by XPS and FTIR analysis and –COOH group of MAA was responsible in developing linkage between the NCs and N-Gr through hydrogen bonding. In the heterostructures of $CsPbBr_3$/N-Gr, PL quenching of NCs was observed with the gradual addition of N-Gr which confirmed the quenching ability of N-Gr. The transfer of electron from CB of the NCs to the LUMO of the N-Gr was responsible for the PL quenching of NCs as supported by CV analysis. The estimated CT efficiency and k_{CT} were 43% and 10.5×10^7 s^{-1} respectively. This work provided vital understanding of the charge transfer phenomenon in the NCs/N-Gr heterostructures that could further stimulate the research of heterostructures comprising of halide perovskites NCs and multidimensional nanostructures.

3.2 Photoexcited Electron Transfer in Hydrophobic Fluorescent $FAPbBr_3$ Perovskite Nanocrystals and Graphene Heterostructures

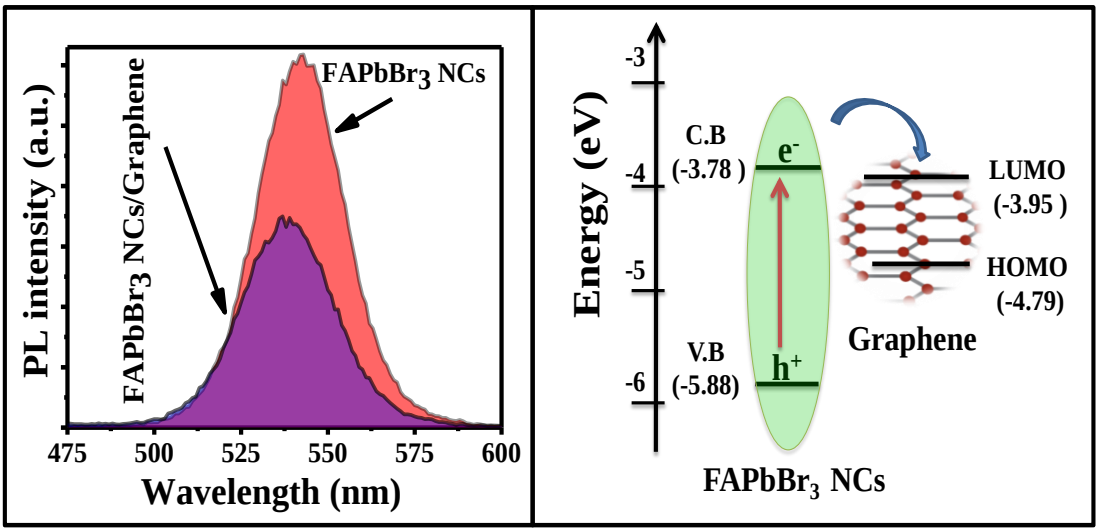

This section presents the fabrication of $FAPbBr_3$ nanocrystals (NCs) and graphene heterostructures and explore the charge transfer dynamics between the components of heterostructures that is a vital phenomenon affecting the overall efficiency of optoelectronic devices. The photoluminescence (PL) quenching of $FAPbBr_3$ NCs with successive addition of graphene confirms the quenching ability of graphene. The photoexcited electron transfer from the conduction band of the NCs to the lowest unoccupied molecular orbital of graphene is responsible for PL quenching that is supported by time-resolved photoluminescence (TRPL) and cyclic voltametric (CV) analysis. The electron transfer occurs via type-I electronic band alignment. A reduction of charge transfer resistance at the interface makes the electron transfer easier in heterostructures as assessed by electrochemical impedance spectroscopy (EIS) analysis. Such heterostructures exhibiting facile electron transfer could make efficient commercial antenna systems for optoelectronic devices.

3.2.1 Crystal structure and morphological analysis of $FAPbBr_3$ NCs

To obtain information regarding the crystal structure of the synthesized $FAPbBr_3$ NCs, powder XRD was utilized. The XRD pattern of prepared $FAPbBr_3$ NCs is presented in figure 3.2.1(a). The XRD pattern depicts the cubic crystal structure with a space group Pm-3m, number 222, similar to that is reported for the bulk crystals with a unit cell parameter of a = b = c = 5.99 Å but larger than that of $MAPbBr_3$ (5.92 Å). This difference arises due to the difference in the size of the methyl ammonium (MA) and formamidinium (FA) cation. The diffraction peaks are well indexed with the cubic XRD pattern and agree with the standard cubic structure of the bulk $FAPbBr_3$ (JCD 87-0158).[180] As indicated by the HRTEM images, the as-synthesized $FAPbBr_3$ NCs exist in broad size distribution, figure 3.2.1(b). The $FAPbBr_3$ NCs possess an average particle size of 8 nm (Figure 3.2.1(b), inset). The high-resolution TEM of $FAPbBr_3$ NCs confirms the high degree of crystallinity present in NCs with an average lattice fringe spacing of 0.279 nm and 0.216 nm (Figure 3.2.1(c)) that corresponds to the (200) and (211) hkl planes, respectively and are in good agreement with the XRD pattern confirming the cubic structure. Selected area electron diffraction (SAED) pattern also approves the cubic crystalline nature of NCs (Figure 3.2.1(d)). [181, 182] The SAED pattern further confirms that the sample is polycrystalline, as multiple bright spots originate from different Bragg's reflection planes. Since the sample areas which are under examination during SAED analysis are as small as several hundred nanometers in size compared to XRD, where sample areas are several millimeters in size. The planes that are not expressed in XRD can be seen in SAED analysis, for instance, the (222) plane is also observed with the (210) plane in the SAED pattern.

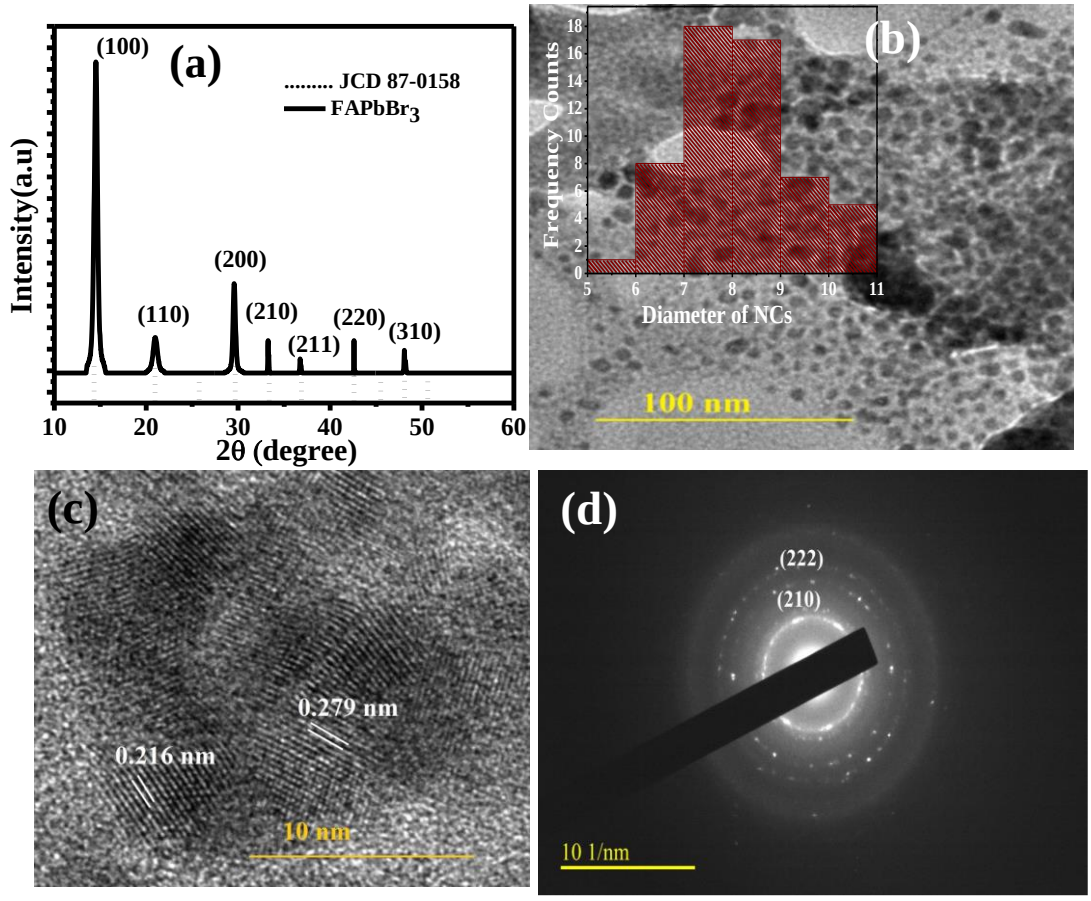

Figure 3.2.1 (a) XRD pattern, (b) TEM micrograph with inset bars graph displaying the size distribution, (c) High-resolution TEM image and (d) SAED pattern of $FAPbBr_3$ NCs.

3.2.2 Characterization of Graphene oxide (GO) and Graphene (Gr)

3.2.2.1 Fourier-Transform Infrared (FTIR) analysis of GO and Gr

The FTIR spectra of graphene oxide (GO) and graphene (Gr) are displayed in Figure 3.2.2(a). The FTIR spectrum depicts all relevant signals of oxygen containing functional groups in GO confirming the successful transformation of graphite to GO. The major observed peaks of Gr and GO are listed in table 3.2.1. The FTIR spectrum of Gr exhibits few signals that arise due to the variation of charges between carbon atoms. This slight difference results to a small induction in electric dipole, which gives a very clean spectrum of Gr as observed. It is clear from the spectrum that the peaks of oxygenated functional groups are diminished in Gr that confirms the complete reduction of GO to Gr.[183, 184]

Table 3.2.1 The FTIR analysis of Gr and GO.

Mode of Vibration	Observed Peak Position (cm^{-1})
Stretching vibration of O-H group	3300
Stretching vibration of surface absorbed CO_2	2100
Stretching vibration of C=C	1635, 1650
Stretching vibrations of C=O	1720
Stretching vibrations of C-O	1048

3.2.2.2 Powder X-ray Diffraction (XRD) Analysis of GO and Gr

Figure 3.2.2(b) represents the XRD pattern of Gr and GO. The graphene shows a peak at $2\Theta = 26.5^{o}$ that corresponds to the reflection of (002) plane, while in case of GO a single peak is observed at 10.2^{o} corresponding to (001) reflection plane of GO. In transformation from GO to Gr, a decrease in inter planar distance (d spacing) from 0.9 nm to 0.33 nm is observed. The decrease in d-spacing is attributed to the absence of oxygen containing functionalities in the Gr. This further confirms the formation of Gr from GO by eliminating hydroxyl, carbonyl and epoxy group and reformation of sp^2 channel on reduction.[183, 184]

3.2.2.3 Raman Analysis of GO and Gr

The synthesized GO and Gr are also analyzed by Raman spectra (Figure 3.2.2(c)) which permit for consideration of C=C and conjugation, that results in increase in intense peaks in Raman spectrum. In the Raman spectrum of GO a peak centered at 1605 cm^{-1} is observed (G band) that corresponds to the E_{2g} phonon of the sp^2 hybridized carbon, and another peak centered at 1350 cm^{-1} (D band) results from the breathing mode of κ-point phonons of A_{1g} symmetry. In case of graphene the G band is centered at 1597 cm^{-1} that is slightly shifted from G band of GO. The ratio of the intensity of these bands (I_D/I_G) indicates the quality of product. The I_D/I_G decreases from 0.80 to 0.66. The difference represents the less of defects results by the restoration of aromatic structures.[185]

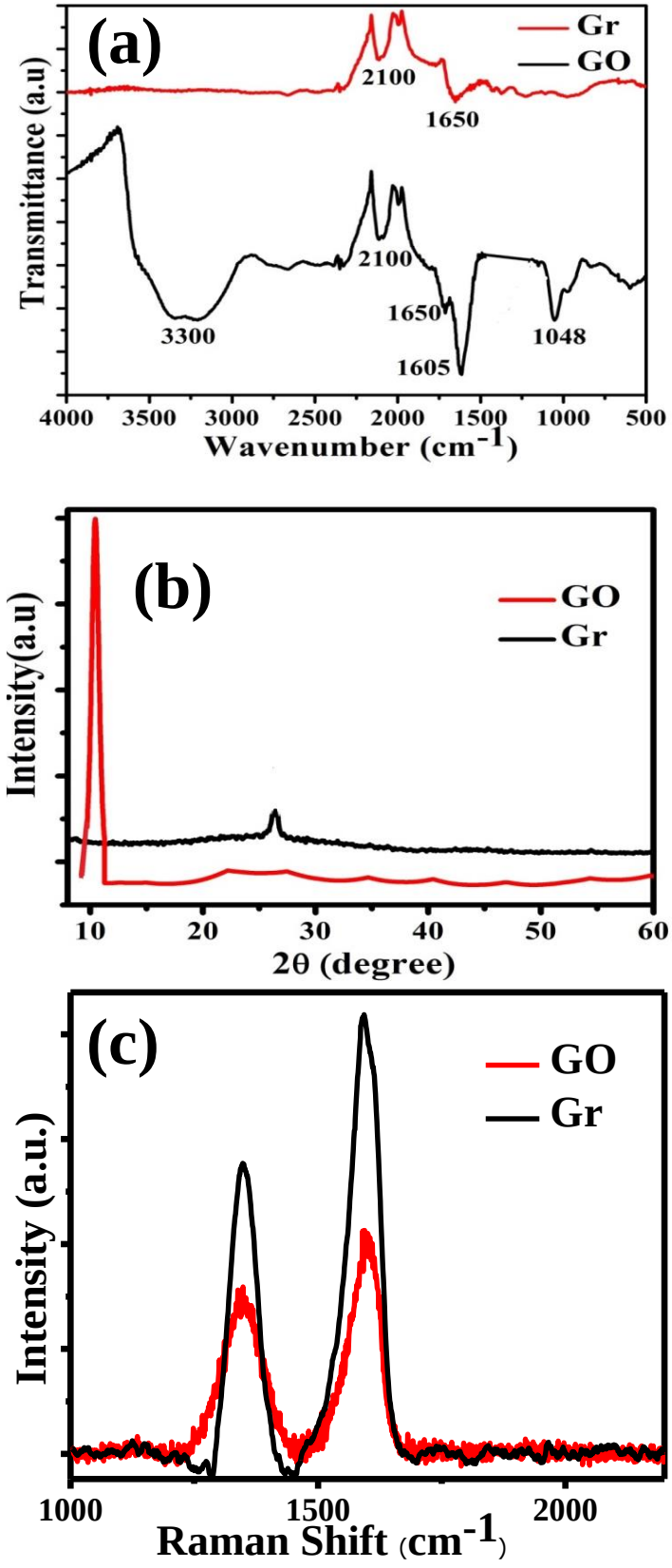

Figure 3.2.2 (a) FTIR spectra of GO and Gr and (b) XRD patterns of GO and Gr (c) Raman spectra of GO and Gr.

3.2.3 Characterization of $FAPbBr_3$/Gr heterostructures

3.2.3.1 FTIR analysis of $FAPbBr_3$ NCs and $FAPbBr_3$/Gr heterostructures

FTIR is used to study the chemical changes that occurred due the interaction of $FAPbBr_3$ NCs with Gr in $FAPbBr_3$ NCs/heterostructures. The FTIR spectra are displayed in Figure 3.2.3. In the FTIR spectra, the peaks at 1700-1750 cm^{-1} and 1200-1300 cm^{-1} correspond to the C=O stretching and C-O bending vibrations of oleic acid molecules. As well as, the C-N stretching (1020-1200 cm^{-1}), N-H stretching (3000-3300 cm^{-1}), N-H bending (1650 cm^{-1}), C-H stretching (2850-3000 cm^{-1}) vibrations, all confirm the presence of $FAPbBr_3$ and oleyl ammine.[186] In the FTIR spectrum of $FAPbBr_3$/Gr, we observe a significant reduction in the intensities and broadening of all peaks while the peak of C-H stretching vibrations (2850-3000 cm^{-1}) that arise due the oleic acid and Oleylamine capping ligand become broader that indicate the non-polar tails of capping ligands interacts with Gr. In the heterostructure of NCs/Gr, we observe a small signal at 1640 cm^{-1} that corresponds to the presence of C=C group of Gr. The hybrid spectrum of both Gr and NCs confirms the attachment of Gr with NCs.

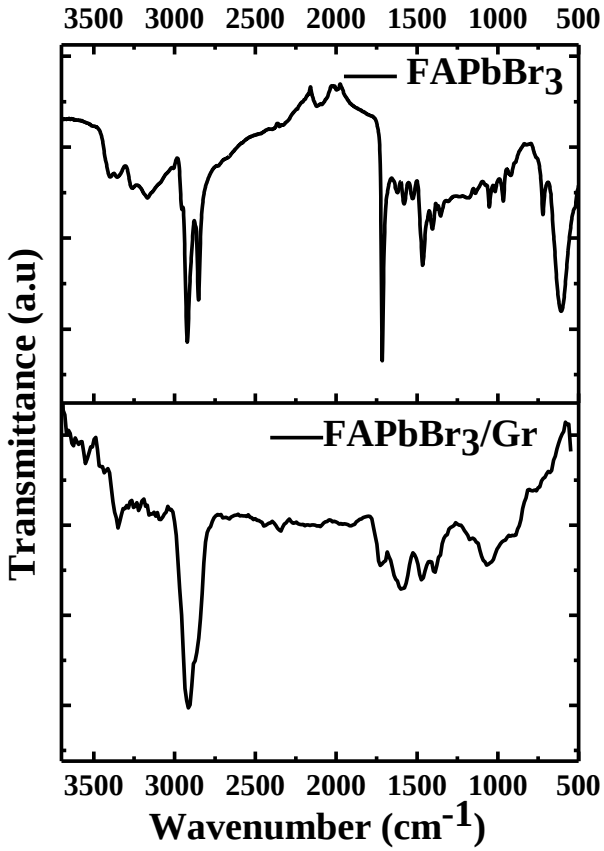

Figure 3.2.3 FTIR spectra of $FAPbBr_3$ NCs and $FAPbBr_3$ NCs/Gr heterostructure.

3.2.3.2 Powder XRD, TEM and HRTEM analysis of $FAPbBr_3$/Gr heterostructures

Figure 3.2.4(a) compares the powder XRD patterns of NCs and NCs/Gr heterostructure. It is clear from the XRD pattern of NCs/Gr heterostructure that the presence of Gr does not affect the crystal structure of NCs (there is no change in peaks position and peaks intensity), and the pattern contains the diffraction peaks of both NCs and Gr that indicates the successful formation of NCs/Gr heterostructures. The occurrence of the weak peak at the (002) plane in the powder XRD pattern of NCs/Gr heterostructure can be attributed to the small amount and low crystallinity of Gr as compared to $FAPbBr_3$ NCs. The assembly of $FAPbBr_3$ NCs with Gr can also be visualized from the TEM image (Figure 3.2.4(b)). The spherical-shaped NCs particles are embedded in the network of graphene. The high-resolution TEM (HRTEM) image of the heterostructure represents the (211) lattice planes of $FAPbBr_3$ NCs with an interplanar distance of 0.21 nm and (002) graphitic planes with a 0.32 nm interplanar distance for Gr. (Figure 3.2.4(c)).

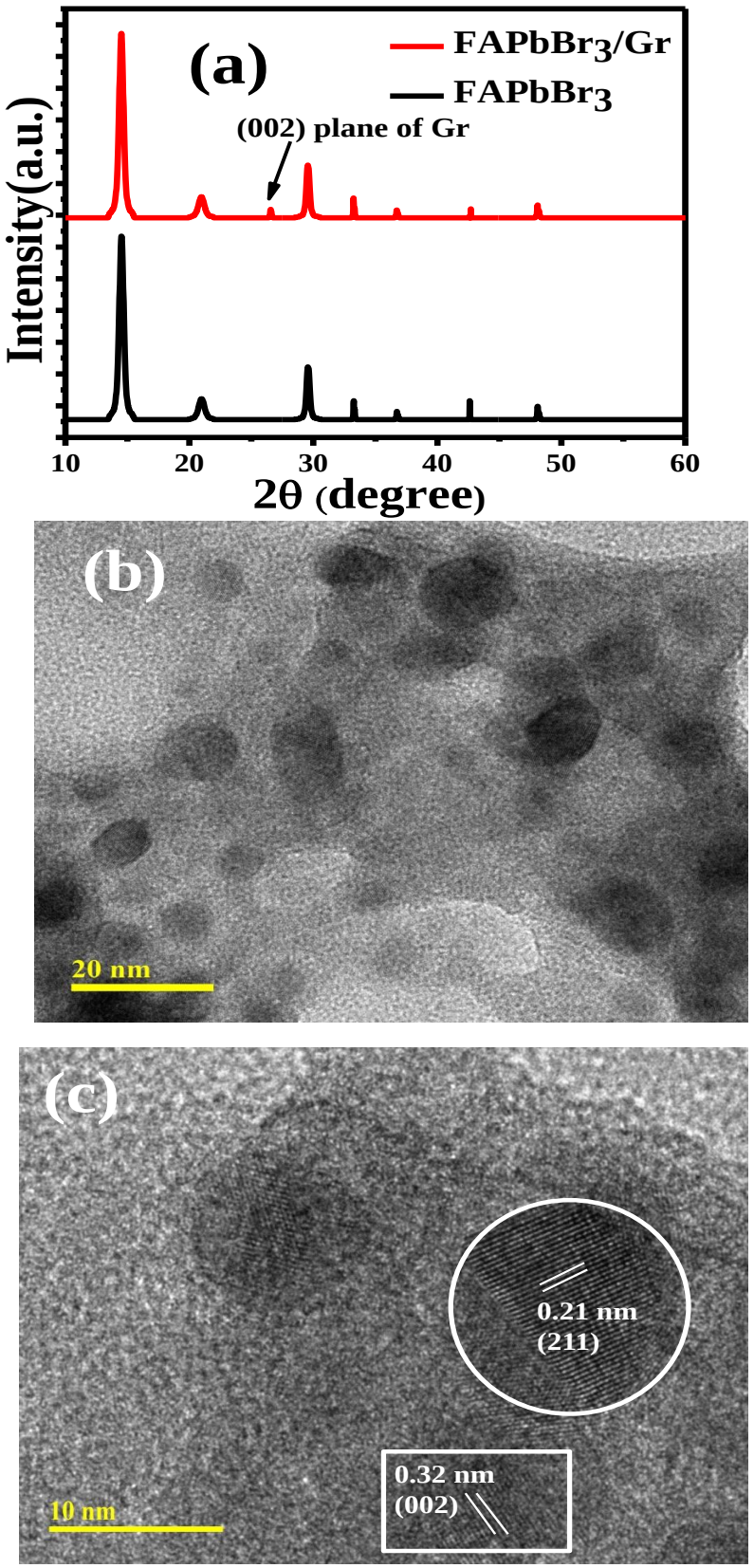

Figure 3.2.4 (a) Powder XRD patterns of $FAPbBr_3$ NCs and NCs/Gr heterostructure, (b) TEM and (c) HRTEM images of the $FAPbBr_3$ NCs/Gr heterostructure.

3.2.4 PL quenching and CT dynamics in $FAPbBr_3$ NCs/Gr heterostructures

The UV-Vis absorption and PL spectra of $FAPbBr_3$ NCs are depicted in figure 3.2.5(a). The bare $FAPbBr_3$ NCs show an absorption edge at 530 nm corresponding to a band gap of 2.33 eV.[187] The bare $FAPbBr_3$ NCs show PL peak maximum at 544 nm with a narrow full width at half maxima (FWHM of ~25 nm). The measured intense PL is attributed to excitonic transitions of $FAPbBr_3$ and agrees with the previously reported PL spectra of $FAPbBr_3$ NCs.[187, 188] The absorption spectra of $FAPbBr_3$ NCs and $FAPbBr_3$ NCs/Gr heterostructures solutions are depicted in figure 3.2.5(b). The concentration of $FAPbBr_3$ NCs remains constant while different volumes (100 μL -700 μL) of Gr solution were added to the $FAPbBr_3$ NCs solution. The absorbance retained the feature of $FAPbBr_3$ NCs with successive addition of Gr solution.

The steady-state PL of $FAPbBr_3$ NCs and the NCs/Gr were carried out to examine the charge carrier recombination and CT dynamics in bare $FAPbBr_3$ NCs and $FAPbBr_3$ NCs/Gr heterostructures. The PL spectra of $FAPbBr_3$ NCs (1 g/L) and $FAPbBr_3$ NCs/Gr heterostructures suspensions in toluene are displayed in figure 3.2.5(c). In the heterostructures with increasing amount of Gr from 100 μL to 700 μL, the PL intensity decreases, suggesting the presence of the small amount of Gr as compared to NCs, quenching the PL of NCs. The PL quenching is usually attributed to energy transfer or CT from donor to acceptor in the heterostructures. As a result of CT, the emission intensity of the donor generally decreases and that of the acceptor increases. The reduction in PL intensity of NCs as depicted in figure 3.2.5(c) suggests that the NCs work as donor in $FAPbBr_3$ NCs/Gr heterostructures. The absence of the PL signal of Gr (Figure 3.2.6) in the observed PL range limits to see the effect on PL of Gr. Due to the minimum overlap of the absorption spectrum of the acceptor (Gr) and emission spectrum of the donor ($FAPbBr_3$ NCs) (Figure 3.2.5(d)), the energy transfer is very unlikely to occur in our case, as reported previously.[185] Therefore, the photoinduced CT from photoexcited NCs to the Gr is the plausible mechanism for the PL quenching of the NCs. The decrease in PL intensity with increasing Gr content advocates enhanced charge extraction across the $FAPbBr_3$ NCs/Gr interface with the successive addition of Gr. This indicates that the photoinjected charge carriers (electron and hole) in NCs spatially separate at the interface and subsequently transferred from the NCs to the Gr. In the heterostructures comprising the small concentration of Gr, due to the high charge carrier mobility of Gr, the charges recirculate, and an accumulation of charges occur in the Gr that causes a built-in potential at the NCs/Gr interface. Hence resulting in the

slight blue shift in the PL spectrum of the donor perovskites NCs. However, when the concentration of Gr rises, the built-in potential due to charges is not significant which could cause a blue shift in the PL spectra; rather it displays a slight red shift and eventually, the PL returns to the original position. A similar blue shift in the PL of donor NCs was previously reported in $CsPbBr_3$ NCs-phosphorene, $CsPbBr_3$ nanoparticles-reduced GO and $CsPbBr_3$ NCs-carbon dot heterostructures.[189-191]

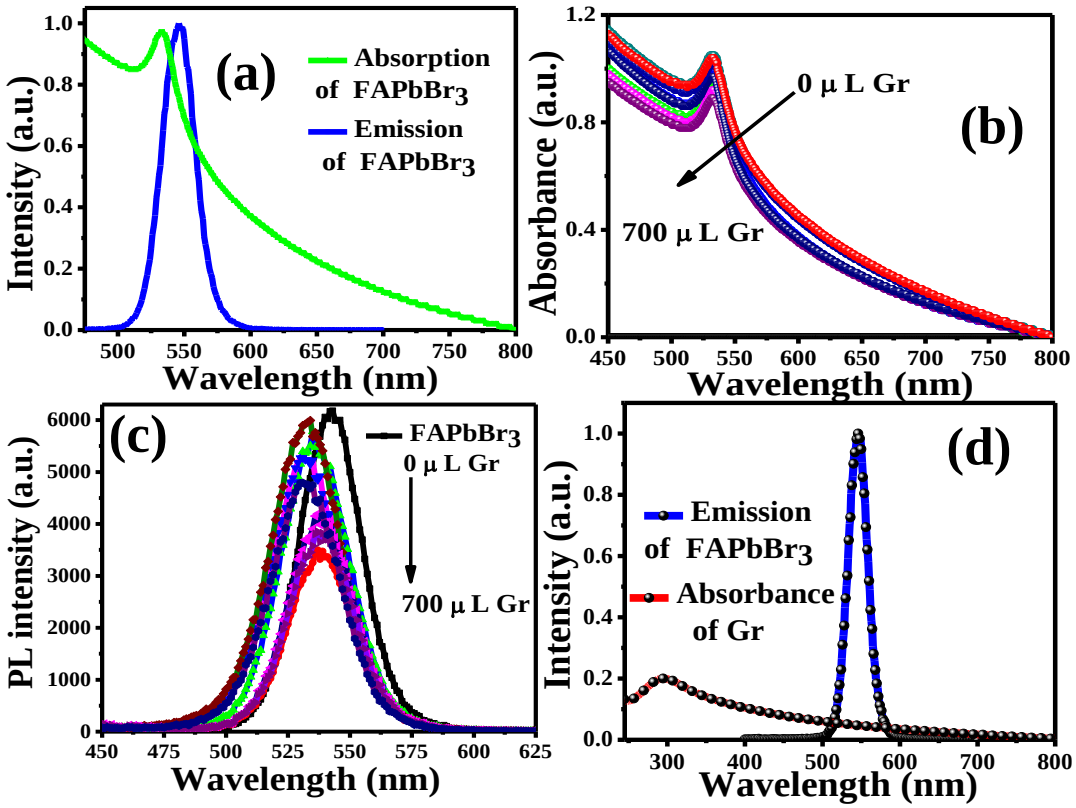

Figure 3.2.5 (a) UV-Vis absorption and PL spectra of 1 g/L solution of $FAPbBr_3$ NCs, (b) UV-Vis absorption spectra of 1 g/L solution of $FAPbBr_3$ NCs and $FAPbBr_3$ NCs/Gr heterostructures in toluene solvent with different amount of Gr, (c) PL spectra of $FAPbBr_3$ NCs and $FAPbBr_3$ NCs/Gr heterostructures in toluene solvent containing different amounts of Gr, and (d) PL spectrum of NCs in toluene solvent and UV-Vis absorption spectrum of Gr in water.

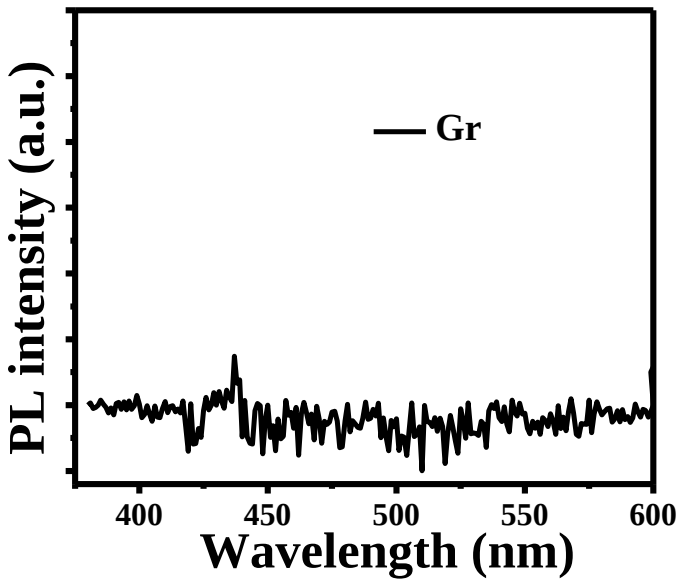

Figure 3.2.6 Steady state PL spectrum of Gr.

The main mode of PL quenching comprises static or dynamic quenching, or a combination of both dynamic and static quenching. In static quenching, the formation of a complex between the fluorophore and quencher causes the decrease in PL. While in dynamic quenching, a collision between the quencher and fluorophore is the reason for the reduction of the PL intensity. There is an equal chance of occurrence of combined dynamic and static quenching. To evaluate the operative static or dynamic PL quenching of $FAPbBr_3$ NCs, the Stern-Volmer equation[192, 193] (1) was applied.

$$\frac{F_0}{F} = 1 + K_{SV}[Q] \qquad (1)$$

Where F and F_0 represent the steady-state PL intensities of NCs in the presence and absence of Gr, respectively; [Q] symbolizes the amount of Gr; and Ksv denotes the Stern-Volmer quenching constant. A Stern-Volmer plot is displayed in figure 3.2.7(a). The deviation of the plot from linearity suggested the occurrence of both static and dynamic modes of quenching resulting a decrease in PL intensity of NCs.

To get further insight into the origin of PL quenching and to verify the CT from $FAPbBr_3$ NCs to Gr, the PL decay kinetics was studied as it is more robust than PL. The PL decay kinetics of bare $FAPbBr_3$ NCs and $FAPbBr_3$ NCs/Gr heterostructures is shown in Figure 3.2.7(b). After excitation at 306 nm the resultant kinetics were well fitted by bi-exponential decay function, equation (2).

$$A(t) = A_1 e^{(-t/\tau_1)} + A_2 e^{(-t/\tau_2)} \qquad (2)$$

Where τ_1 *and* τ_2 are the time constants of the PL decay, A_1 and A_2 are the associated weighting coefficients. The τ_1 is related to shallow trap-assisted recombination of the charge carrier, while the τ_2 can be associated with deep level trap recombination of the charge carriers. All the extracted PL decay parameters obtained from the best fits are listed in table 1. From the observed parameters the average PL lifetime of all samples was calculated by using equation (3).

$$\boldsymbol{\tau_{average} = \frac{A_1 \tau_1 + A_2 \tau_2}{A_1 + A_2}} \qquad \textbf{(3)}$$

From the calculated average PL lifetime of samples, the average lifetime of bare $FAPbBr_3$ NCs and $FAPbBr_3$ NCs/Gr heterostructures remained nearly constant, and the emission intensity continuously decreased with an increase in the concentration of Gr. This trend is observed up to the addition of 400 μL Gr but at higher concentrations of Gr, both PL intensity and PL decay lifetime decrease (from 32.99 ns to 14.48 ns). These observations suggest that the static mode of quenching is dominant with dynamic quenching as a minor process up to 400 μL Gr concentration as in static mode only PL intensity decrease as observed in our case. While static quenching shifted to dynamic mode of quenching at higher concentrations of Gr (500-700 μL) because at higher concentration of Gr, not only the PL intensity, but PL lifetime of the NCs also decreases. The rate constant for CT is estimated by using the relation given in equation (4).

$$\boldsymbol{k_{CT} = \frac{1}{\tau_{(FAPbBr_3+Gr)}} - \frac{1}{\tau_{(FAPbBr_3)}}} \qquad \textbf{(4)}$$

The estimated values of the CT rate constant (k_{CT}) are tabulated in table 3.2.2. The calculated values indicate that with an increasing amount of Gr from 100 to 700 μL, the value of k_{CT} also increases from 9.22 $\times 10^4$ to 3.8 $\times 10^7$ s^{-1}, which suggests that an efficient CT occurs from the NCs to the Gr. Similar results on CT studies between $CsPbBr_3$ and reduced graphene oxide have been reported by Pu et al.[194] and Liu et al.[191] The enhanced charge extraction in $FAPbBr_3$ NCs in the presence of Gr is attributed to the connections developed by Gr with NCs through the hydrophobic interaction of oleylamine ligand on the surface of NCs, consequently reduces the trapping of charges and hence favors the fast CT.

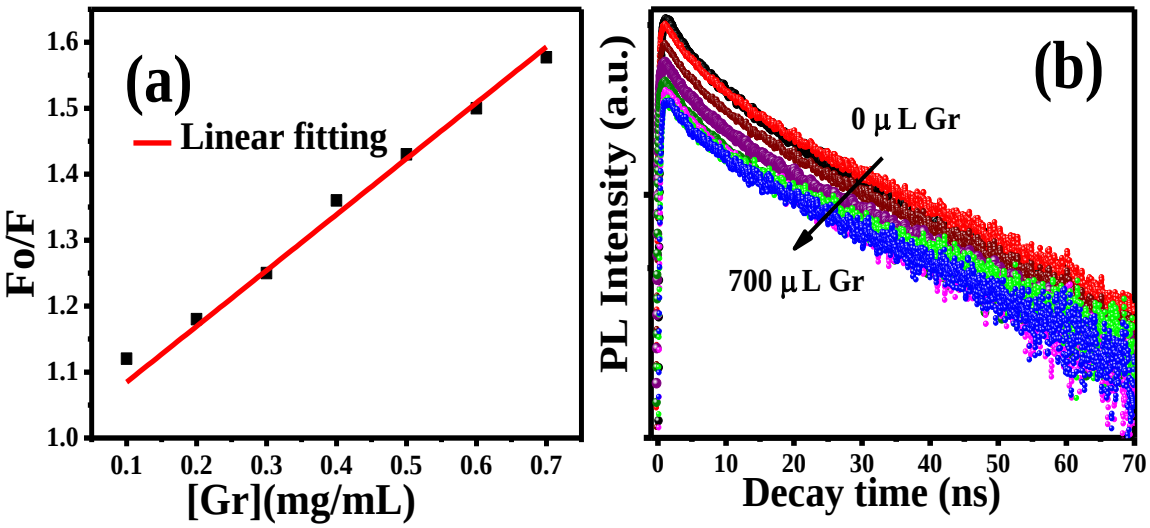

Figure 3.2.7 Stern-Volmer plot, (b) PL kinetics of 1 g/L solution of $FAPbBr_3$ NCs and $FAPbBr_3$ NCs/Gr heterostructures in toluene solvent with different amounts of Gr.

Table 3.2.2 The PL decay parameters of $FAPbBr_3$ NCs and $FAPbBr_3$ NCs/Gr heterostructures with their respective k_{CT} values.

Graphene content (µL)	A_1	τ_1 (ns)	A_2	τ_2 (ns)	Average PL time (ns)	k_{CT} (s^{-1})
0	0.34	6.24	0.66	46.77	32.99	-
100	0.36	6.203	0.64	47.90	32.89	9.22×10^4
200	0.40	6.094	0.60	49.73	32.28	6.67×10^5
300	0.35	5.201	0.65	45.21	31.21	1.720×10^6
400	0.31	5.069	0.69	40.70	29.70	3.58×10^6
500	0.44	4.16	0.56	30.16	18.72	2.3×10^7
600	0.445	3.51	0.555	26.98	16.54	3.01×10^7
700	0.43	3.09	0.47	28.00	14.48	3.8×10^7

3.2.5 Electrochemical measurements

To disentangle the CT, electron, or hole between Gr and NCs, electrochemical band edges for NCs and Gr were assessed by recording CVs in the non-aqueous environment using the three-electrode system (glassy carbon electrode as a working electrode, platinum wire as counter electrode and silver wire as a reference electrode).

The equations (5) and (6) are used to estimate the electrochemical lowest unoccupied molecular orbital (LUMO) or conduction band (CB) and highest occupied molecular orbital (HOMO) or valence band (VB) energy levels in eV unit;[190]

$$\mathbf{E\ (LUMO) = -e\ [\ E_{red}^{onset} + 4.4]} \quad \mathbf{(5)}$$

$$\mathbf{E\ (HOMO) = E\ (LUMO) - E_{0\text{-}0}} \quad \mathbf{(6)}$$

$E_{0\text{-}0}$ refers to the 0-0 energy assigned to the lowest energy transition, which can be determined from Tauc's method. The evaluated values of $E_{0\text{-}0}$ for NCs and Gr are 2.1 eV and 2.5 eV, respectively (Figure 3.2.8 (a & b)). The wide band gap in case of Gr results from the sp^2 hybridization of carbon that introduces localized states, and the presence of band tail lying in the $E_{0\text{-}0} = E_{opt}$ can be conditional. The band broadening of Gr in the low energy tail of the absorption spectrum is related to the Urbach tail (E_u) that the following relation can estimate: $\alpha = \alpha_0 \exp(h\upsilon/E_u)$. The reciprocal of the slope obtained by plotting ln α versus hυ (Figure 3.2.9 (a)) gives the value of E_u that is 1.66 eV. The energy gap (E_g) between HOMO and LUMO of Gr is estimated by using a relation $E_g = E_{opt} - E_u$. Using the aforementioned relation, the E_g of Gr is calculated to be 0.84 eV. From the onset reduction potential observed in the cyclic voltammogram of Gr (Figure 3.2.8(c)) is -0.453 eV; the value of HOMO and LUMO of Gr are estimated by the expressions given below and are consistent with the previously reported studies.[191]

$$E\ (LUMO) = -e\ [-0.453 + 4.4] = -3.947\ eV$$

$$E\ (HOMO) = [-3.947 - 0.84] = -4.79\ eV$$

Monolayer graphene has a 0 eV band gap with a Fermi level at -4.5 eV. [195, 196] The Gr flakes possess a small band gap of 0.84 eV, observed in our case. For Gr, the value of HOMO and LUMO are -4.79 eV and -3.95 eV, respectively.

The values of CB and VB band edges are estimated from the onset reduction potential (-0.615 eV) in the cyclic voltammogram of NCs (Figure 3.2.8(d)) as given below:

$$E\ (CB) = -e\ [\ -0.615 + 4.4] = -3.785\ eV$$

$$E\ (VB) = [\ -3.785 - 2.1] = -5.885\ eV$$

The loci of VB and CB edges of the NCs are -5.88 eV and -3.785 eV, respectively. The respective energy levels of the two materials forming heterostructures indicate that the band edges of the components of the heterostructures align type-I band alignment that allows the transfer of an electron from excited NCs to Gr more quickly than the transfer of hole as it is seen by the difference in their energy levels (Figure 3.2.10(a)), because the difference in the CB of NCs and LUMO orbital of Gr is minimal as compared to

the difference between the VB of the NCs and HOMO of Gr. Hence, based on differences, we concluded that the process of electron transfer is more favorable than the transfer of hole.

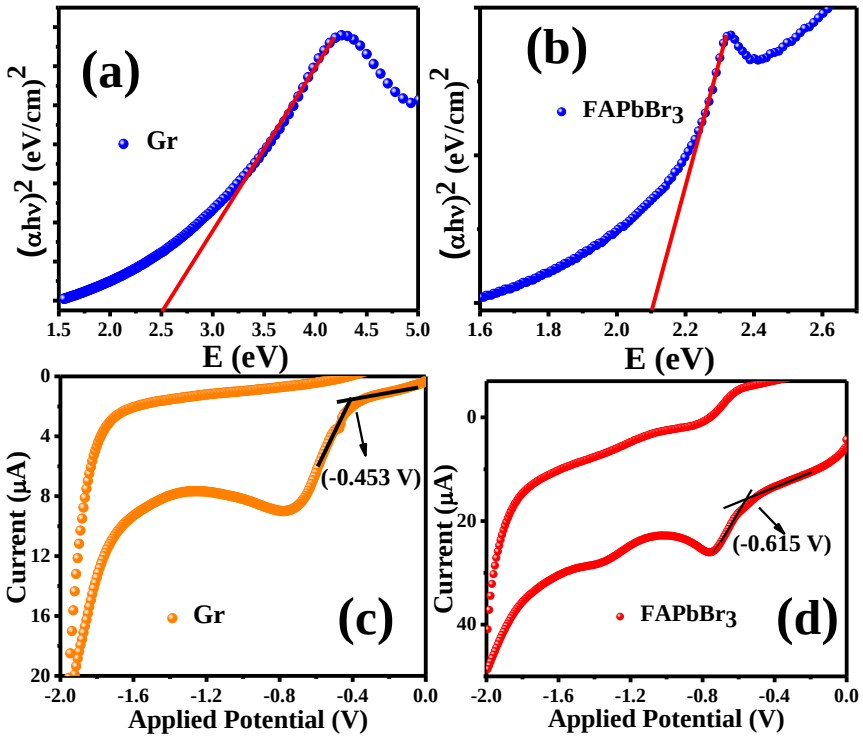

Figure 3.2.8 (a) Tauc plot of Gr. (b) Tauc plot of $FAPbBr_3$ NCs. (d) CV of Gr. (e) CV of $FAPbBr_3$ NCs with supporting electrolyte of $TBAPF_6$ (50 mM) in toluene:acetonitrile (4:1) solution.

Electrochemical impedance spectroscopy (EIS) is generally used to study the interfacial CT resistance in materials. EIS spectrum of the pristine $FAPbBr_3$ NCs and $FAPbBr_3$ NCs/Gr heterostructures are recorded, and corresponding Nyquist plots are presented in figure 3.2.9(b). By comparing the EIS spectra of the pristine $FAPbBr_3$ NCs and $FAPbBr_3$ NCs/Gr heterostructures, it is seen that curvature of the semi-circle effectively decreases in case of heterostructure, indicating that the CT resistance of heterostructures is reduced significantly than the pristine $FAPbBr_3$ NCs. The decreased CT resistance also advocates the more facile charge separation and CT in the heterostructures.

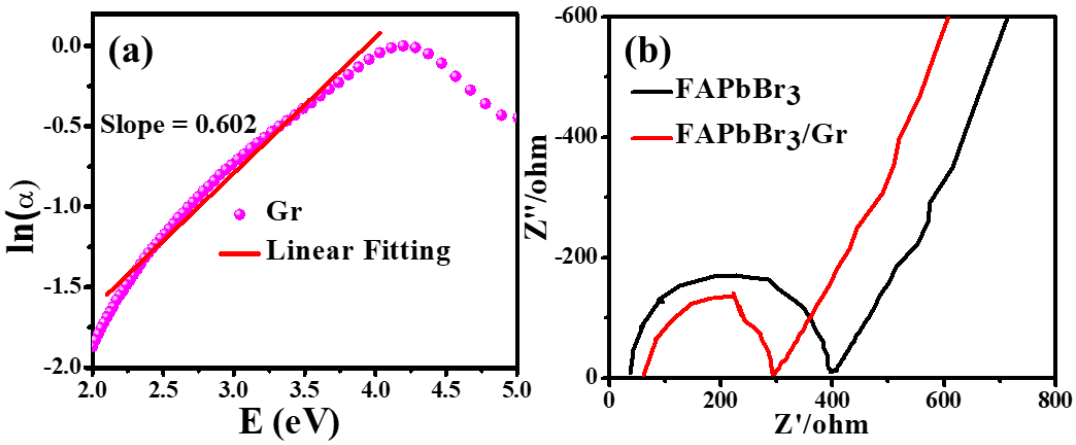

Figure 3.2.9 (a). ln α vs. hν plot of Gr, (b) Electrochemical Impedance spectroscopy (EIS) analysis of $FAPbBr_3$ NCs and $FAPbBr_3$ NCs/Gr heterostructures.

.

Figure 3.2.10(b) displays the schematic of NCs and Gr interaction and electron transfer from the VB of NCs to the HOMO of the Gr. Absorption of 306 nm photons generate excitons in perovskites NCs, and electrons and holes recombine by inter-band transitions radiatively in the lack of Gr as displayed by the PL spectrum. When Gr is mixed with NCs, a potential is established at the boundary of $FAPbBr_3$ NCs/Gr resulting to the spatial separation of charge carries at the edge, thus inhibiting the recombination of charge carriers. The charge carriers spatially separate successfully at $FAPbBr_3$ NCs/Gr interface, thus assisting the course of CT.[197] In our case, Gr establishes Van der Waals interactions with free non-polar oleyl moiety of oleylamine capping ligand that facilitate anchoring of Gr on the surface of perovskites NCs. These connections inhibit charge trapping and offer a site for charge separation and enhance the electron transfer from NCs to Gr.

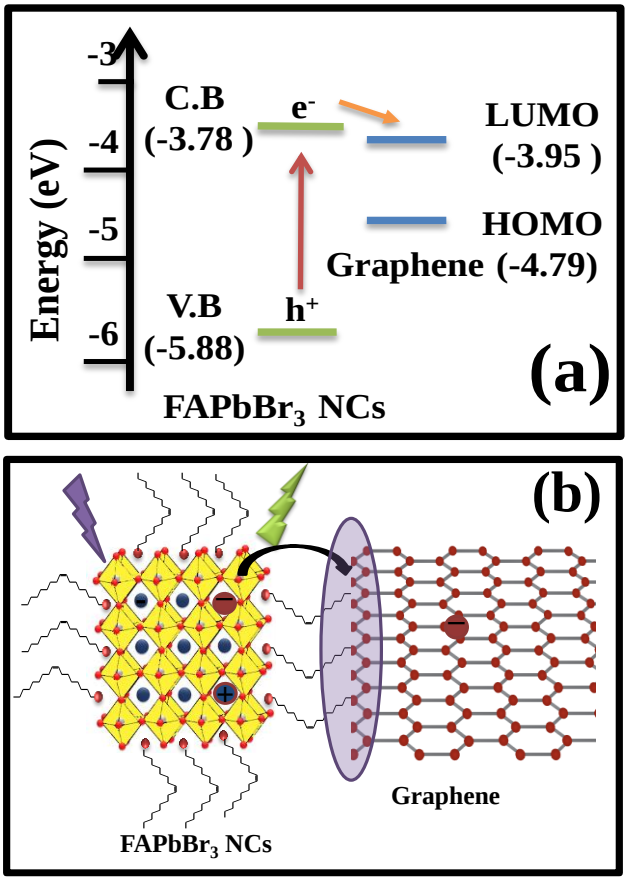

Figure 3.2.10 (a) Diagrammatic representation of band edges of NCs and Gr, (b) Schematic representation of CT dynamics in $FAPbBr_3$ NCs/Gr heterostructures.

3.2.6 Summary

The work demonstrated the synthesis and vital understanding of the electron transfer phenomenon in organic-inorganic halide NCs/Gr heterostructures. The successive introduction of graphene in NCs resulting in PL quenching of $FAPbBr_3$ NCs that was attributed to the electron transfer from the CB of the NCs to LUMO of the Gr in $FAPbBr_3$ NCs/Gr heterostructures arising because of the type I band alignment of the components of the heterostructures. The significant reduction in CT resistance made the process of electron transfer more facile, as evaluated by EIS analysis. The estimated CT rate, k_{CT} increased from 9.22×10^4 s^{-1} to 3.8×10^7 s^{-1} by the adding 100-700 µL of 1 g/L solution of Gr. This work will open further research avenues for multidimensional halide perovskite/Gr heterostructures. Such heterostructures with a designed charge transfer are becoming promising candidates for the next generation perovskites optoelectronic and solar devices.

3.3 Tuning the Charge Transfer Efficiency by Functionalizing Ligands in $FAPbBr_3$ Nanocrystals and Graphene Heterostructures

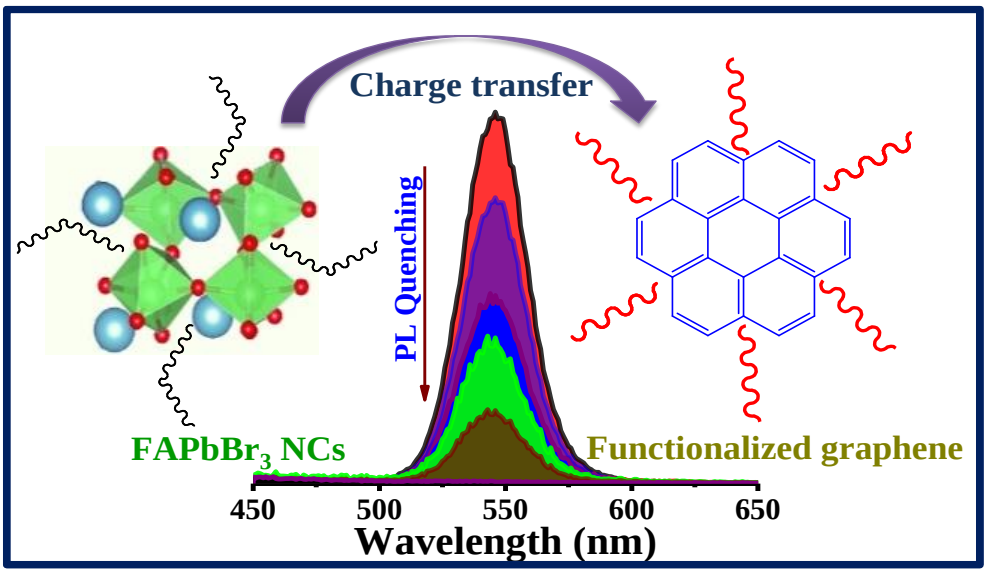

The present section describes the influence of different surface functionalities of graphene on the CT dynamics in $FAPbBr_3$ NCs attached with functionalized graphene heterostructures. The functionalized graphene i.e., graphene oxide (GO) and amino acids, i.e., alanine (GO-Ala), tyrosine (GO-Tyr), and cysteine (GO-Cys) functionalized GO are synthesized. By assembling the heterostructures of functionalized graphene with NCs, the quenching of photoluminescence (PL) of the $FAPbBr_3$ NCs has been observed. The photo-generated hole transfer from $FAPbBr_3$ to functionalized graphene is responsible for PL quenching that is supported by time-resolved photoluminescence (TRPL) and cyclic voltammetry (CV) analysis. Our studies reveal that the rate of CT and charge transfer efficiency (E_{CT}) strongly depend on the nature of the functionalizing moieties. The highest hole transfer efficiency for NCs-functionalized graphene heterostructure is observed in case of cysteine functionalized GO (88.84 %) and the lowest with the GO (38.15 %). This suggests that the cysteine functionalized graphene is the best hole acceptor amongst all the functionalized graphene. Our work offers a method to regulate the energetics and to investigate the extent of hole transfer in perovskite NCs and functionalized graphene heterostructures.

3.3.1 Characterization of functionalized graphene

The GO was synthesized by employing modified Hummer's method.[183] Amino acid including alanine, tyrosine and cysteine were selected to synthesize bio-compatible, eco-friendly surface decorated graphene. The oxidation of graphite and transformation to GO is performed by introduction of –COOH, -OH and -C-O-C- moieties between the layers of graphene. Presence of these functional moieties results in the exfoliation of graphene layers. The GO can be further modified in terms of properties by substituting these functional moieties of GO with different compounds. Amino acids are inexpensive, bio-compatible, and environment friendly as well as they also possess good nucleophilic properties. Hence, amino acids are regarded to be beneficial for the surface functionalization of graphene. As represented in figure 3.3.1, during synthesis of amino acid functionalized GO from GO, nucleophilic condensation reactions taken place between the -COOH groups of GO and $–NH_2$ groups of the amino acids. It is proposed that the surface oxygen moieties of the GO are reacting with the amino group of the amino acids, as a result of condensation reaction between them takes place and amino acid surface decorated GO are obtained. The functionalized GO is characterized by employing various techniques that are described in forthcoming paragraphs.

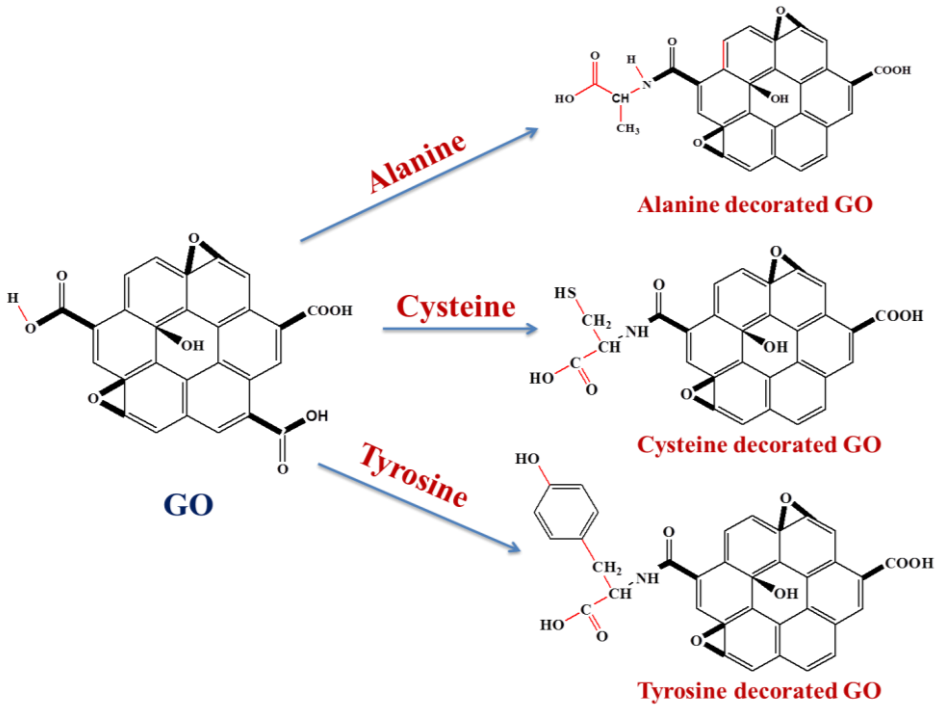

Figure 3.3.1 Schematic of surface decoration of Alanine, Tyrosine, and Cysteine (amino acid) on GO.

3.3.1.1 SEM and EDX analysis of functionalized graphene

The morphological analysis of the functionalized graphene is conducted with the help of SEM and the obtained micrographs are presented in figure 3.3.2. The functionalized graphene exists in innate sheet like morphology,[198] while aggregation is observed in the SEM micrographs of amino acid functionalized GO. The aggregation among sheets is due to the interaction developed between different polar groups connected to functionalized graphene sheets. The extent of layer aggregation varies in different prepared samples. This indicates the presence of different functional groups of amino acids on the surface of GO. The clear topographical differences among different samples can be observed. The difference in morphology of GO and amino acid functionalized GO could be due to additional functionalization of GO with different amino acids. Energy dispersive X-ray (EDX) analysis of all functionalized graphene is also performed to confirm the presence of different elements in the synthesized samples. The EDX analysis of GO confirms the presence of only C and O in GO samples, while the EDX of GO-Ala confirms the presence of C, O and N in the samples. The presence of N in amino acid functionalized GO, confirms the amino acid functionalization. In case of GO-Cys, the signal of S element is also observed along with the signals of C, O and N. Because the cysteine amino acid contains thiol (-SH) functionality in addition to amino ($-NH_2$) and carboxylic acid groups (-COOH) functionalities. The observed weight and atom percentages of the elements in different synthesized samples are given in table 3.3.1.

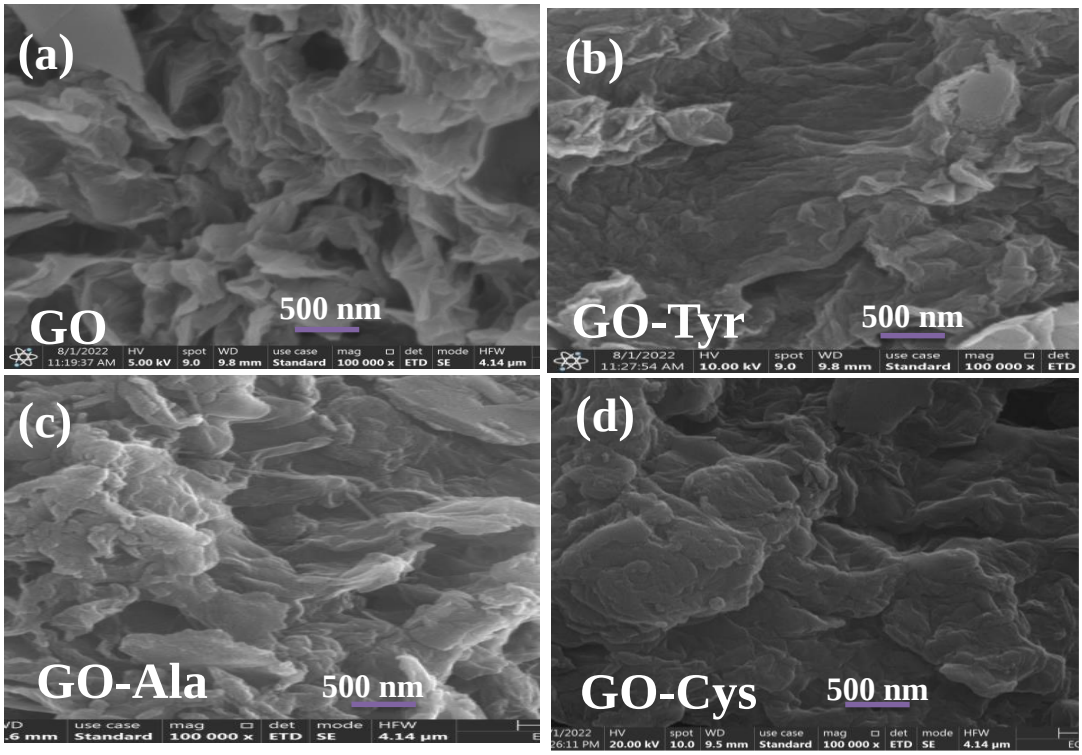

Figure 3.3.2 (a-d) SEM micrographs of surface decorated graphene (a) GO, (b) GO-Tyr, (c) GO-Ala, and GO-Cys.

Table 3.3.1 EDX analysis and percentage elemental composition of functionalized graphene.

Sample Code	C		O		N		S	
	Atom %	Weight %	Atom %	Weight %	Atom %	Weight %	Atom %	Weight %
GO	54.41	50.01	45.59	49.99	-	-	-	-
GO-Ala	65.13	59.12	33.18	27.44	7.43	7.70	-	-
GO-Tyr	56.03	50.32	41.28	35.79	8.18	8.39	-	
GO-Cys	58.47	63.63	35.10	28.67	5.15	4.19	2.78	1.28

3.3.1.2 XRD analysis of functionalized graphene

The X-ray diffraction (XRD) patterns of the functionalized graphene are presented in figure 3.3.3 (a). The XRD pattern of GO contains a diffraction peak centered at 11.41˚ assigned to the (001) diffraction plane of GO and that is attributed to the interlayer distance of 8.06 Å.[183] This peak signifies the presence of numerous oxygen containing moieties on the surface of graphene with increased interlayer spacing because of the interactions of oxygen containing moieties. The XRD patterns of all amino acid functionality graphene are clearly different from the XRD pattern of GO. The diffraction peak that is observed in the diffraction pattern of GO is not observed in the XRD patterns of amino acid functionalized GO, indicating that graphene sheets are loosely stack with each other and graphene layers are non-smectic. The diffraction peaks of amino acid non-smectic graphene oxide are shifted towards higher 2θ values indicating the high degree of reduction of GO (decrease in the number of oxygens containing moieties). A decrease of interlayer spacing is also observed due to the introduction of amino acids on to the surface of graphene. The diffraction peaks of GO-Cys, GO-Ala, and GO-Tyr are centered at 19.01˚, 26.66˚ and 29.33˚ and these are assigned to an interlayer spacing of 4.62, 3.35, and 3.04 Å, respectively. Amongst amino acid functionalized graphene, the interlayer spacing in GO-Tyr is observed to be the smallest and its diffraction plane intensity is comparatively greater. This is because, the aromatic ring of tyrosine is preferably oriented parallel to the plane of aromatic ring of graphene by π-π stacking interactions. As a result of these additional interactions and other types of intermolecular interactions, the GO-Tyr possess specifically scrolled structure, between graphene and multi-walled carbon nanotubes, which is similar to rolling a single layer of graphene as reported previously.[199] It is noteworthy the amino acid functionalized graphene oxide's XRD patterns show the graphene layers are significantly exfoliated and do not recombine by the introduction of amino acid on the surface of graphene. This can be attributed to highly random arrangement of N-containing moieties of amino acids on the surface of graphene sheets.

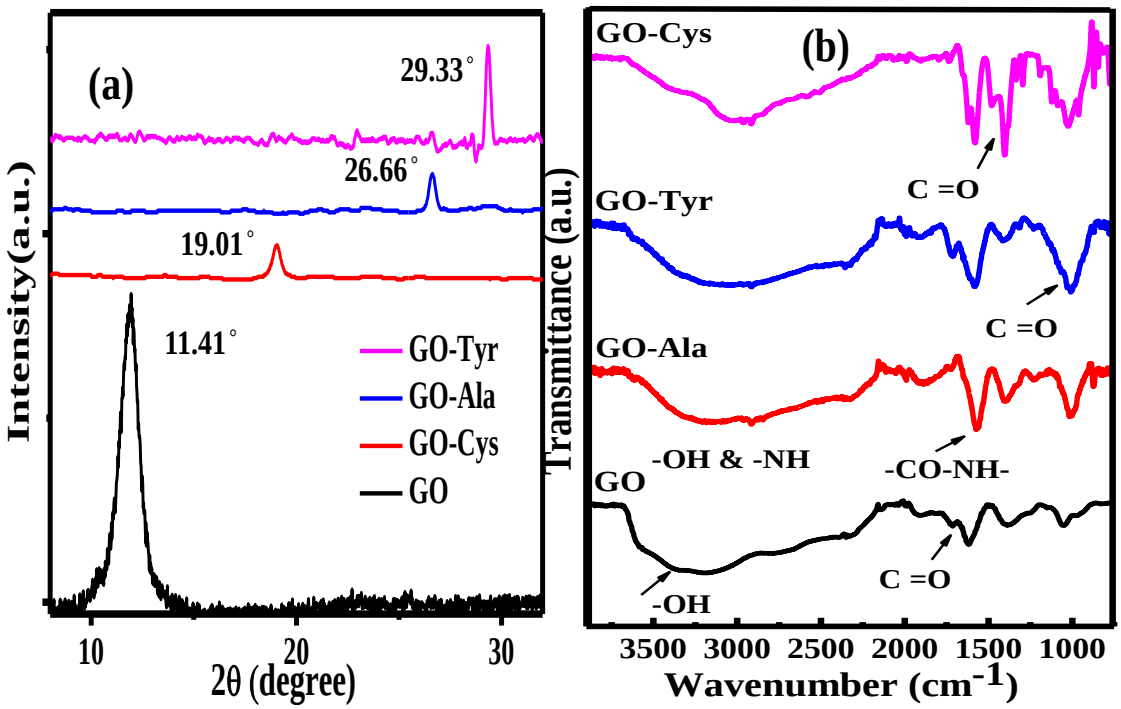

Figure 3.3.3 (a) XRD patterns of surface decorated graphene, i.e., GO, GO-Tyr, GO-Ala, and GO-Cys. (b): FTIR spectra of GO, GO-Ala, GO-Tyr, and GO-Cys.

3.3.1.3 FTIR analysis of functionalized graphene

The FTIR analysis is employed to understand the bonding interactions in GO and amino acid functionalized graphene that is displayed in figure 3.3.3(b). In the FTIR spectrum of GO displays all the relevant signals of oxygen containing functional groups, which confirms the successful transformation of graphite to GO. In the FTIR spectrum of the GO, strong absorption signals around 3300, 1721, 1600 cm^{-1} are because of the vibrational modes of –OH, C=O and C-O that are present in COOH and C–O–C (epoxy), correspondingly.[200] After amino acid functionalization of GO, the reduction in signals of the oxygen containing groups confirms the functionalization of GO. The wide and less intense peak at ~3300 cm^{-1} (indicating the loss of oxygen containing moieties) can be assigned to the N–H stretching vibration of the amine groups with less intensity and symmetric peak shape. The band of amino acid functionalization can be found at ~1580 cm^{-1} and is assigned to the in plane stretching of –NH group of amino acids. The signal of C=O stretch appearing at 1721 cm^{-1}, shifts to 1628 cm^{-1} corresponding to amide (-CO-NH-) of amino acid functionalize graphene oxide confirming the functionalization of GO with amino acids. Moreover, the band appeared at 871 cm^{-1} can be assigned to the asymmetric stretching vibrational mode of

the –NH moiety. These results suggest the successful functionalization of GO with amino acids as reported previously that the surface functionalization of graphene with amino acid is resulted by condensation reaction of –COOH groups of GO with the –NH_2 group of amino acids.[200, 201] table 3.3.2, summarizes the observed peaks in FTIR spectra of functionalized graphene.

Table 3.3.2 *Observed vibrational modes in functionalized graphene.*

Mode of Vibration	**Observed Peak (cm^{-1})**
Stretching vibrations of O-H and -NH group	3300
Stretching vibrations of C=O	1718
Bending vibrations of C=O	1017
Stretching vibration of C=O	1590
asymmetric –NH_2 stretching	871

3.3.1.4 Raman analysis of functionalized graphene

The Raman spectra of the GO and amino functionalized GO are displayed in figure 3.3.4(a). In the Raman spectrum of GO a peak centering at 1599 cm^{-1} is observed (G band) that originate from the E_{2g} phonon of the sp^2 hybridized carbon, and another peak at 1320 cm^{-1} (D band) corresponds to the breathing mode of κ-point phonons of A_{1g} symmetry. In case of GO-Tyr, GO-Ala, GO-Cys, slightly shifted G-band centering at 1594, 1596 and 1602 cm^{-1}, respectively is observed. Similarly, the D-bands of the amino acid functionalized graphene oxide are also shifted. In case of GO-Tyr, Gr-Ala, GO-Cys, the shifted D-band centering at 1317, 1313 and 1330 cm^{-1}, respectively are observed. The ratio of the intensity of these bands (I_D/I_G) specifies the quality of the product. The ration of I_D/I_G increases during the transformation of GO to amino acid functionalized GO. For instance, for GO, GO-Tyr, GO-Ala, and GO-Cys, the calculated value of I_D/I_G is 0.74, 1.32, 1.34, and 1.36, respectively. The difference in values of I_D/I_G represents that the introduction of amino acid moieties in GO, decreases the defects by the restoration of benzene ring. Because presence of amino group on the surface of graphene reduces the oxygen containing functionalities of GO and increases the number of graphene layers.[201, 202]

3.3.1.5 UV-Vis analysis of functionalized graphene

The UV-Vis absorption spectra of functionalized graphene are recorded in water and presented in figure 3.3.4(b). In the absorption spectrum of GO, two peaks are observed at 274 nm and 220 nm, which are assigned to n-π* and π-π* transitions, respectively.[203] In case of introduction of amino acid in GO, the peak position of n-π* transition does not change but GO-Ala and GO-Cys absorption peaks display reduced intensity, indicating the functionalized graphene contains less moieties that show this transition. However, the peak position of π-π* transition shifted in amino acid functionalized GO in such a way that GO-Tyr and GO-Cys show a red-shifted peak at 224 and 229 nm respectively, indicating the presence of amino acid on the surface of GO. The red shift in the absorption peak can be linked to the partial deoxygenation and restoration of electronic conjugation in the aromatic structure as reported previously.[204] While in case of GO-Ala, a slight blue shifted peak at 215 nm is observed indicating that introduction of alanine on the surface of GO reduces the number of O containing moieties due to the reestablishment of conjugated structure.[205] Hence, presence of different functional groups also tune the band gap of graphene.

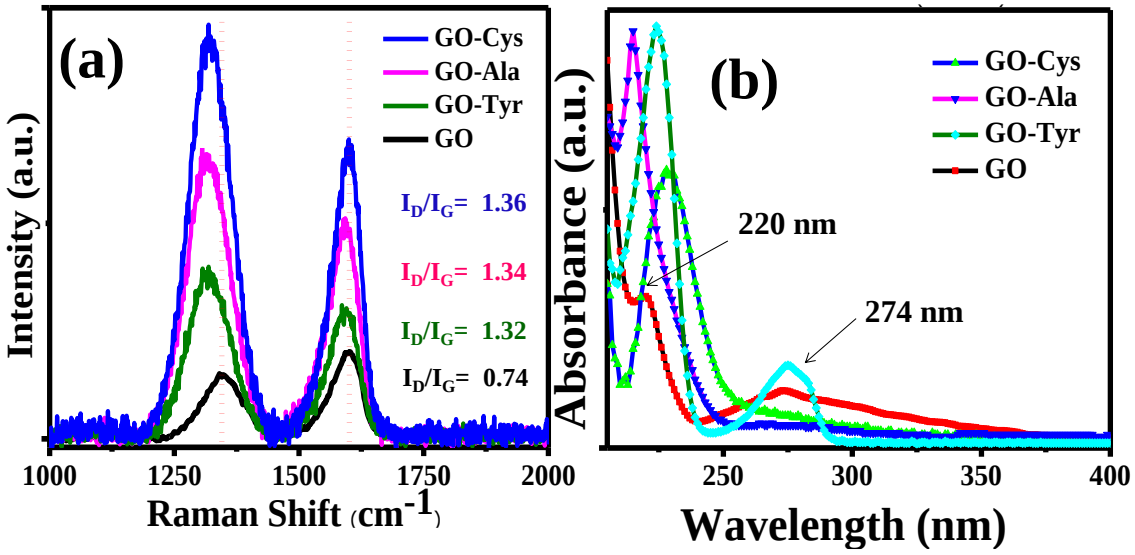

Figure 3.3.4 (a) Raman and (b) UV-Vis absorption spectra of GO, GO-Tyr, GO-Ala, and GO-Cys.

3.3.2 Characterization of $FAPbBr_3$ NCs/functionalized graphene heterostructures

3.3.2.1 TEM and HRTEM analysis of NCs/functionalized graphene heterostructures

The association of $FAPbBr_3$ NCs with functionalized graphene can also be observed in TEM and HRTEM images in figure 3.3.5. The NCs possessing spherical morphology and are embedded in the networks of functionalized graphene as visualized in the figure 3.3.4(a, c, e & g). The occurrence of the 0.24, 0.29, 0.21 nm fringe spacing corresponding to (211), (200), (220) diffraction planes of NCs and 0.81, 0.33, 0.44, 0.31 nm fringe spacing in GO, GO-Ala, GO-Cys, GO-Tyr in NCs/functionalized graphene heterostructures confirm the presence of respective component of each heterostructures.

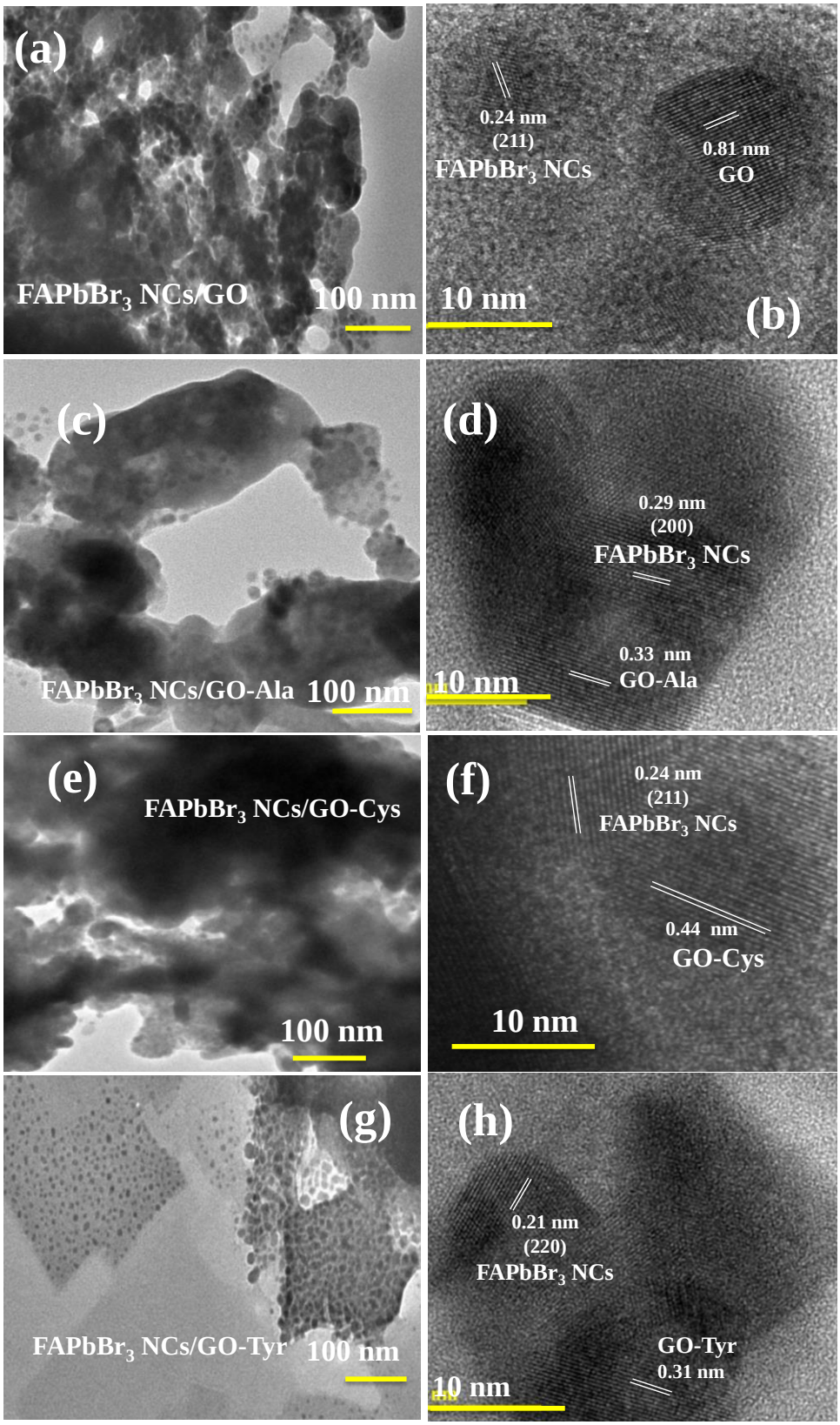

Figure 3.3.5 TEM and HRTEM images of the (a, b) $FAPbBr_3$ NCs/GO, (c, d) $FAPbBr_3$ NCs/GO-Ala, (e, f) $FAPbBr_3$ NCs/GO-Cys, and (g, h) $FAPbBr_3$ NCs/GO-Tyr heterostructures.

3.3.2.2 XRD analysis of NCs/functionalized graphene heterostructures

The XRD patterns of the $FAPbBr_3$ NCs and NCs/graphene heterostructures are displayed in figure 3.3.6(a). The XRD pattern of the NCs is well indexed with the cubic crystalline phase of $FAPbBr_3$ (JCD 87-0158).[206] There is no observable change in the peak position of XRD patterns of NCs in the presence of functionalized graphene i.e., GO, GO-Cys, GO-Tyr, and GO-Ala. However, a decrease in the peak intensity is observed suggesting the presence of functionalized graphene is imparting amorphousness and irregularity to the crystal structures of NCs. Due to the presence of slight amorphous nature, the diffraction peaks of the functionalize graphene do not appear in the XRD patterns of heterostructures.

3.3.2.3 FTIR analysis of NCs/functionalized graphene heterostructures

The chemical nature of binding interactions in the NCs/functionalized graphene heterostructures is understood by performing FTIR analysis of heterostructures, figure 3.3.6(b). In the FTIR spectra of oleylamine capped $FAPbBr_3$ NCs, the peaks at 1200-1300 cm^{-1} and 1700-1750 cm^{-1} are assigned to the C-O bending and C=O stretching mode of vibrations of oleylamine. The N-H stretching (3000-3300 cm^{-1}), the C-N stretching (1020-1200 cm^{-1}), C-H stretching (2850-3000 cm^{-1}) and N-H bending (1650 cm^{-1}) vibrations confirm the oleylamine functionalization of $FAPbBr_3$ NCs.[186] The van der Waals interactions and hydrogen bonding developed amongst different functional moieties of functionalized graphene (C=O, C−O, O−H, $-NH_2$, O-C−OH, -SH etc.) and oleylamine capped $FAPbBr_3$ NCs are responsible for the formation of heterostructures. The change in transmittance intensity of the FTIR spectra along with the widening of peak signals of the aforementioned groups confirm the formation of polar interactions in the NCs/functionalized graphene heterostructures.

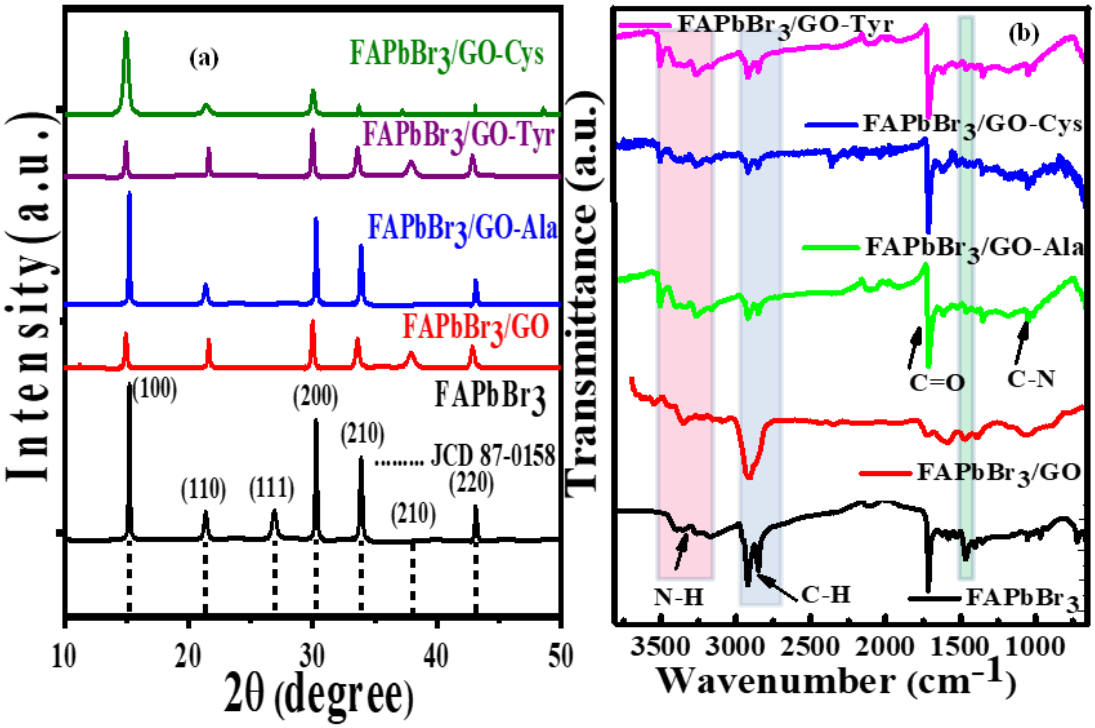

Figure 3.3.6 (a) Powder XRD patterns of $FAPbBr_3$ NCs and NCs/functionalized graphene (NCs/GO, NCs/ GO-Ala, NCs/GO-Tyr, and NCs/GO-Cys) heterostructures, (b) FTIR spectra of $FAPbBr_3$ NCs and NCs/functionalized graphene (GO, GO-Ala, GO-Cys, and GO-Tyr) heterostructures.

3.3.3 Fluorescence quenching of $FAPbBr_3$ NCs by functionalized graphene

The PL spectra of $FAPbBr_3$ NCs and $FAPbBr_3$ NCs coupled with surface decorated graphene are depicted in figure 3.3.7(a) The bare $FAPbBr_3$ NCs shows PL peak maximum at 544 nm with a narrow full width at half maxima (FWHM of ~25 nm). The measured intense PL is attributed to excitonic transitions of $FAPbBr_3$ and is in agreement with the previously reported PL spectra of $FAPbBr_3$ NCs.[206, 207] The PL spectra of GO and amino acid functionalized GO depicted no peak in the observable emission range, indicating the non-emissive nature of these systems (Figure 3.3.7(b)). The PL of $FAPbBr_3$ NCs is effectively quenched upon combining with GO, GO-Cys, GO-Tyr, and GO-Ala, respectively. In the heterojunctions, two main plausible mechanisms could be responsible for quenching of the PL, nonradiative energy transfer or CT. For energy transfer, the overlap of emission spectrum of the donor with the absorption spectrum of the acceptor is a prerequisite.[189] While, because of CT, the emission intensity of the donor decreases and that of acceptor generally increases. The effective reduction of the PL intensity of $FAPbBr_3$ NCs is observed in $FAPbBr_3$

NCs/functionalized graphene heterostructures as depicted in the Figure 7(a). While due to non-emissive nature of all functionalized graphene, no PL is observed for the functionalized graphene. From these results, it is deduced the $FAPbBr_3$ NCs act as donor and functionalized graphene are acted as acceptor in the heterostructures. As far as the energy transfer is concerned, the occurrence of energy transfer could be minimum as there is no overlap of the absorption spectra of all functionalized graphene with the emission spectrum of the $FAPbBr_3$ NCs, figure 3.3.7(c).[200] Therefore, photoexcited CT from $FAPbBr_3$ to the functionalized graphene is a plausible mechanism of PL quenching of $FAPbBr_3$ NCs. The extent of PL quenching is maximum in GO-Cys and the lowest in the case of GO. The intermolecular interactions between oleylamine functionalized NCs with different functional moieties of surface decorated graphene are responsible for effective association and the formation of the heterostructures of the NCs and the functionalized GO. In the heterostructures, the PL of the NCs is quenched due to photoexcited CT from the NCs to the GO.

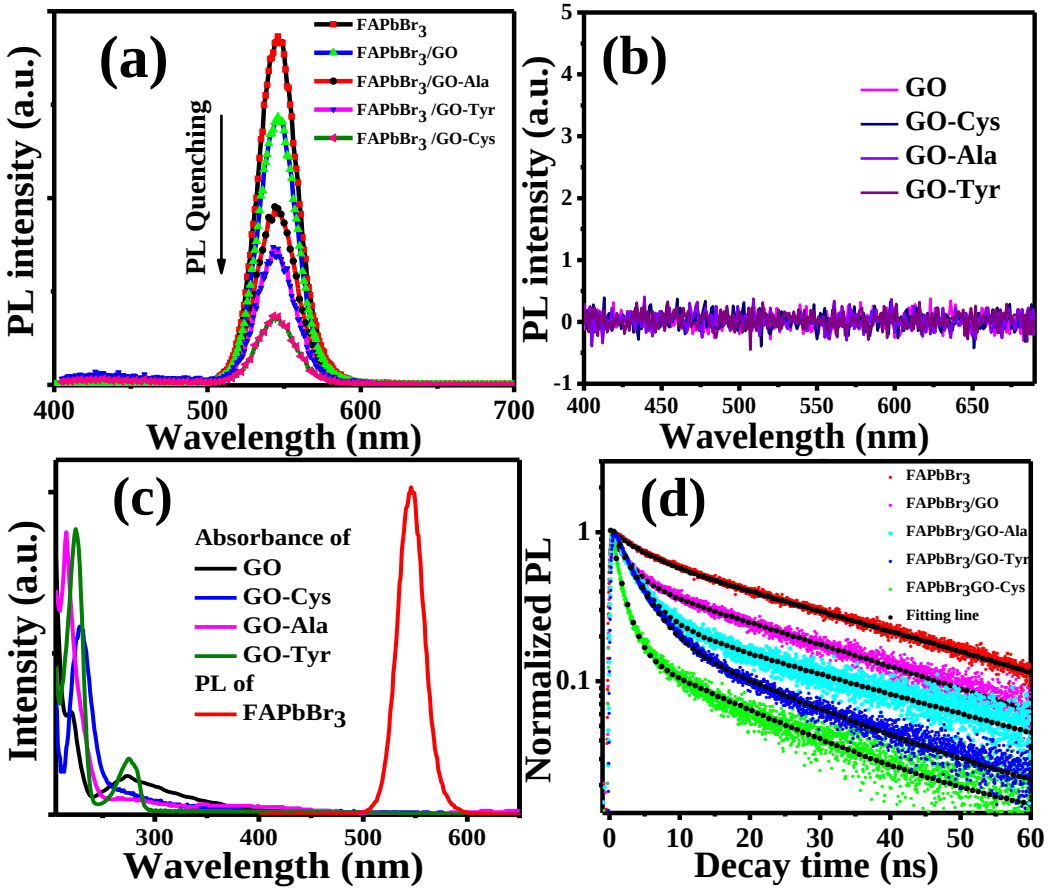

Figure 3.3.7 *(a) PL spectra of $FAPbBr_3$ NCs and $FAPbBr_3$ NCs/functionalized graphene (GO, GO-Ala, GO-Tyr, GO-Cys) heterostructures, (c) PL spectrum of $FAPbBr_3$ NCs in toluene solvent and UV-Vis absorption spectra of GO, GO-Cys, GO-*

Ala, and GO-Tyr in water, (c) PL spectra of GO, GO-Cys, GO-Ala, and GO-Tyr indicating the non-emissive nature of these compounds and (d) PL decay kinetics of $FAPbBr_3$ NCs and $FAPbBr_3$ NCs/functionalized graphene (GO, GO-Ala, GO-Tyr, GO-Cys) heterostructures.

As a control experiment, to study the direct interaction of bare amino acids with NCs, the PL studies of solution of NCs containing amino acid were also carried out and the obtained PL spectra are displayed in figure 3.3.8. The amino acids being polar in nature, were not soluble in the pure anhydrous toluene and into the solution of NCs in toluene even after a stirring of half an hour under same conditions (Figure 3.3.8(d)). There is no change in PL intensity is observed, hence eliminating the direct possibility of interaction of amino acids with NCs.

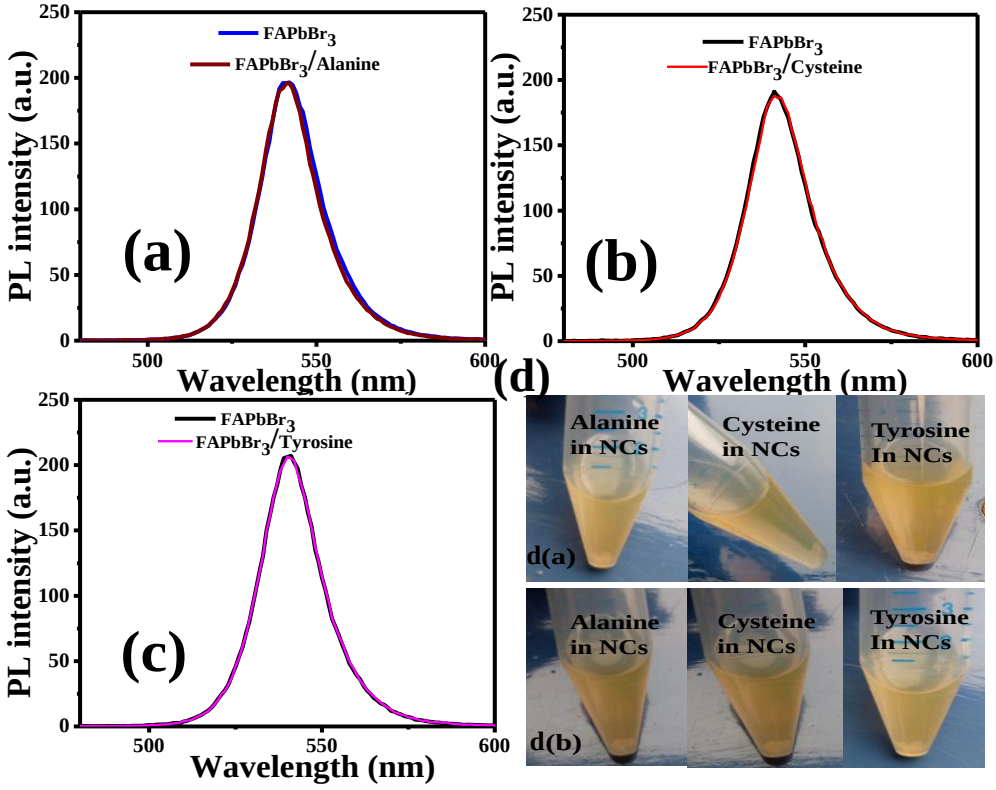

Figure 3.3.8 (a) PL spectra of different amino acids (a) Alanine, (b) Cysteine, and (c) Tyrosine in the solution of $FAPbBr_3$ NCs in toluene, (d) Different amino acids (Alanine, Cysteine, and Tyrosine) in the solution of NCs in toluene, d(a) Before stirring and d(b) After a stirring of half an hour.

The PL kinetics analysis demonstrate an outstanding trend of PL quenching of $FAPbBr_3$ NCs in relationship with different functionalized graphene in heterostructures

as depicted in Figure 3.3.7(d). The resultant PL decay kinetics after excitation at 306 nm is best fitted by bi-exponential decay function, equation (1).

$$A(t) = A_1 e^{(-t/\tau_1)} + A_2 e^{(-t/\tau_2)} \quad (1)$$

Where A_1, A_2 are the associated weighting coefficients and τ_1, τ_2 are the fast and slow time constants of each component of PL lifetime, respectively. According to the previous report,[208] τ_1 (possessing shorter PL lifetime) is related to the trap-state assisted radiative recombination, while the τ_2 (representing longer PL lifetime) can be attributed to excitonic recombination.

All the extracted PL decay parameters from the best fits are listed in table 3.3.3. From the parameters, the average PL lifetime of all samples is calculated by using the equation (2).

$$\tau_{average} = \frac{A_1 \tau_1 + A_2 \tau_2}{A_1 + A_2} \quad (2)$$

The average PL lifetime of bare $FAPbBr_3$ NCs (donor) is the longest ~ 26.81 ns that decreases to 2.99 ns for donor-acceptor heterostructures depending upon the nature of the functionalities present on the surface of graphene. Table 3.3.3 shows the PL decay lifetimes of the NCs in various heterostructures. Amongst all heterostructures, the shortest PL lifetime, 2.99 ns is demonstrated by NCs combined with GO-Cys because of the maximum PL quenching. These results lead to conclude that cysteine decorated GO is the best charge acceptor amongst other amino acids functionalized graphene. The PL decay kinetics is used to estimate various CT parameters. By using τ_{DA} (average PL lifetime of the $FAPbBr_3$ NCs in the presence of acceptor graphene) and τ_D (average PL lifetime of the donor NCs only), the CT efficiency (E_{CT}) is evaluated by using the equation (3),

$$E_{CT} = 1 - \frac{\tau_{DA}}{\tau_D} \quad (3)$$

The rate constant for CT is estimated by using the relation given in equation (4).

$$k_{CT} = \frac{1}{\tau_{(DA)}} - \frac{1}{\tau_{(D)}} \quad (4)$$

The values of E_{CT} and CT rate constant (k_{CT}) are given in Table 1. The highest charge transfer efficiency (88.84 %) is observed when the NCs are coupled with GO-Cys and the lowest 38.15 % for NCs coupled with GO and for other heterojunctions, the calculated values occur between these two limits. The comparative values of k_{CT} suggest that an increase CT rate k_{CT} is 2.30×10^7, 9.04×10^7, 1.09×10^8, 2.97×10^8 s^{-1} for NCs/GO, NCs/GO-Ana, NCs/GO-Tyr, and NCs/GO-Cys, respectively. The calculated

E_{CT} and k_{CT} values advocate the CT process is strongly influenced by the nature of the different functional moieties used for surface decoration of graphene.

Table 3.3.3 *The PL decay kinetics parameters and respective k_{CT} and E_{CT}.*

Sample	A_1	τ_1 (ns)	A_2	τ_2 (ns)	$\tau_{ave.}$ (ns)	k_{CT} (s^{-1})	E_{CT} (%)
$FAPbBr_3$	0.25	4.98	0.75	34.08	26.81	-	-
$FAPbBr_3$/GO	0.35	2.30	0.65	24.38	16.58	2.30×10^7	38.15
$FAPbBr_3$/GO-Ala	0.73	2.84	0.27	21.32	7.83	9.04×10^7	70.79
$FAPbBr_3$/GO-Tyr	0.75	3.22	0.25	17.67	6.83	1.09×10^8	74.52
$FAPbBr_3$/GO-Cys	0.84	1.24	0.16	12.26	2.99	2.97×10^8	88.84

Following pulsed excitation at 306 nm $FAPbBr_3$ NCs, electron and hole (charge carriers) pair is generated in the conduction band (CB) and the valence band (VB), respectively. In the absence of quencher, the photoexcited charge carriers recombine radiatively. While in the heterostructures, the interaction of surface decorated graphene with NCs results in the development of potential at the interface of NCs and surface decorated graphene. The development of this potential at the interface of the heterostructure of NCs/functionalized graphene inhibits the direct recombination of photoinjected charge carriers and favors the spatial separation of charge carriers as reported previously.[209] The photogenerated charge carriers effectively separate at the interface of $FAPbBr_3$ NCs/functionalized graphene heterojunctions and thus promote the CT process.

3.3.4 Electrochemical Measurements

To apprehend the type of CT, electron, or hole between NCs and functionalized graphene, the band edge positions are estimated by cyclic voltammetry (CV) and cyclic voltammograms (CVs) are presented in figure 3.3.9-3.3.10. The Electrochemical band edges are estimated by recording CVs in non-aqueous environment using three electrode system i.e., platinum wire acting as counter electrode, glassy carbon acting as a working electrode, and silver wire acting as a reference electrode. The onset oxidation (E_{Ox}) and reduction (E_{Red}) potentials are used to estimate the electrochemical lowest

unoccupied molecular orbital (LUMO) or conduction band (CB) and highest occupied molecular orbital (HOMO) or valence band (VB) in eV unit:[210]

$$\mathbf{VB\ or\ E_{HOMO} = -e\ (E_{Ox\ vs.NHE} + 4.75)\ (eV)} \quad \mathbf{(5)}$$

$$\mathbf{CB\ or\ E_{LUMO} = -\ e\ (E_{Red,\ vs.\ NHE} + 4.75)\ (eV)} \quad \mathbf{(6)}$$

$$\mathbf{E_{NHE} = E_{Ag/AgCl} + 0.197} \quad \mathbf{(7)}$$

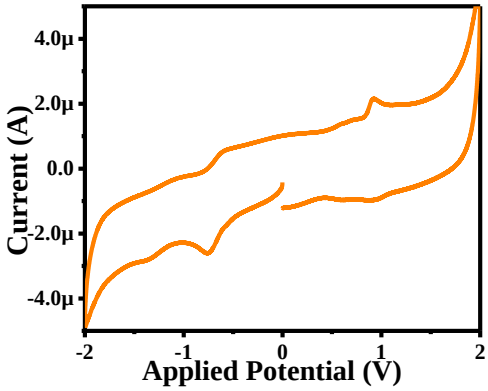

Figure 3.3.9 CV of $FAPbBr_3$ NCs with supporting electrolyte of $TBAPF_6$ (50 mM) in toluene:acetonitrile (4:1) solution.

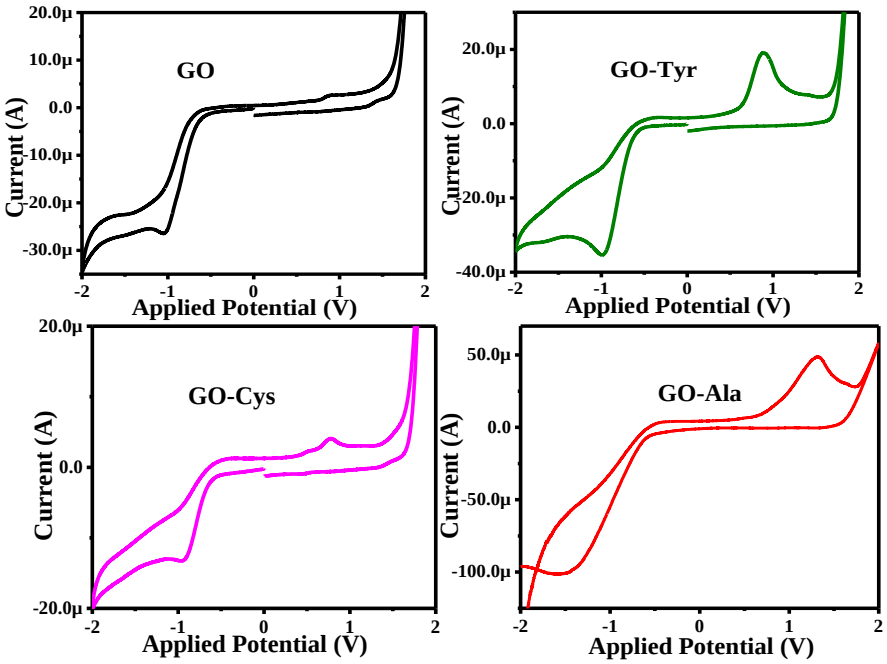

Figure 3.3.10 (a) CV of GO, (b) GO-Tyr, (c) GO-Cys, and (d) GO-Ala with supporting electrolyte of TBAPF6 (50 mM) in toluene:acetonitrile (4:1) solution.

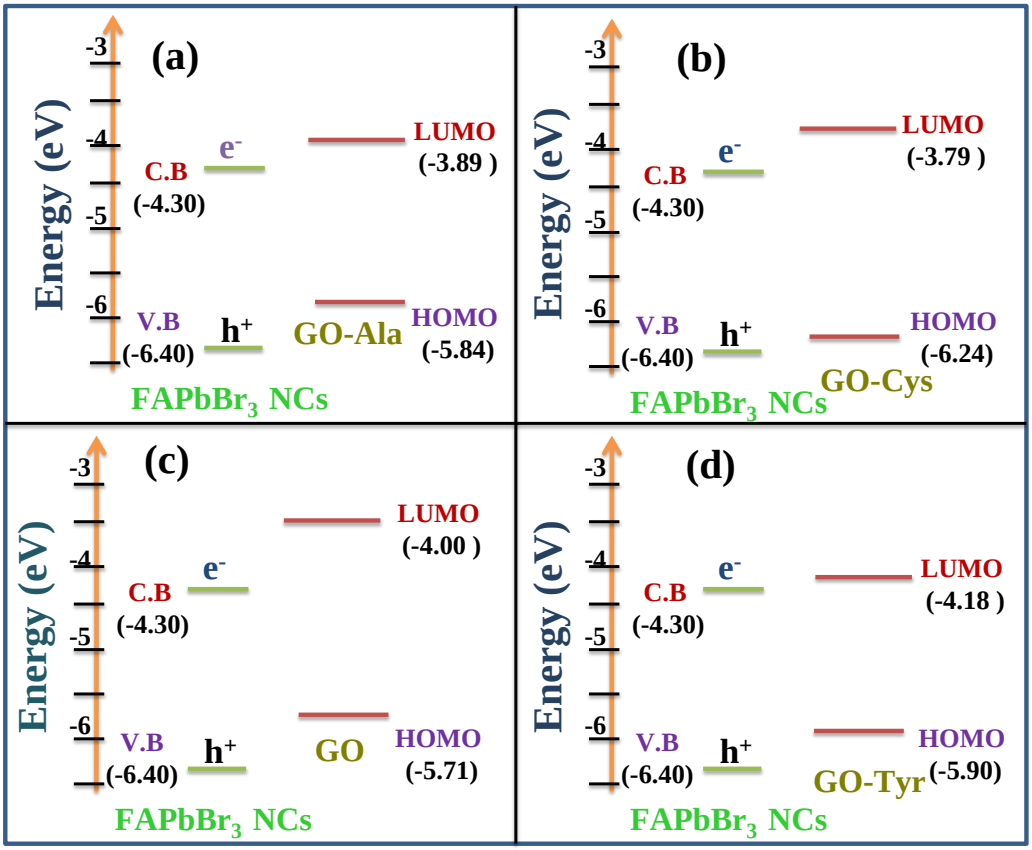

Figure 3.3.11 (a-d) Band edges estimation of $FAPbBr_3$ NCs and functionalized graphene, i.e., GO GO-Cys, GO-Ala, and GO-Tyr) by cyclic voltammetry analysis.

The positions of VB and CB of the NCs are found to be -6.40 eV and -4.30 eV, respectively. The calculated values of HOMO are -5.71, -6.24, -5.84, and -5.90 eV and LUMO levels are -4.00, -3.79, -3.89 and -4.18 eV for GO, GO-Cys, GO-Ala and GO-Tyr, respectively. From the value of HOMO and LUMO levels of functionalize graphene, it can be clearly seen that surface functionalization greatly affect the HOMO and LUMO levels of the graphene. The estimated LUMO and HOMO levels of the functionalized graphene and NCs are presented in figure 3.3.11(a-d). The respective energy levels alignment of the two materials forming heterostructures indicates that the NCs-functionalized graphene form type-II heterojunctions (possibility of electron transfer from LUMO of functionalized graphene to CB of NCs and hole transfer from VB of NCs to HOMO of the functionalized graphene). Hence, from these results, we conclude that the hole transfer from NCs to functionalized graphene is responsible for the PL quenching that is also supported by steady-state and time-resolved PL analysis. The difference between the position of VB of NCs and the HOMO level of different

surface decorated graphene also changes by variation of surface moieties on graphene. The smallest difference in the VB of NCs and HOMO of functionalize graphene is observed in case of GO-Cys (0.16 eV) and largest is found in case of GO (0.69 eV) and the difference between GO-Ala, and GO-Tyr is 0.56 and 0.5 eV, respectively. These results suggest that due to smaller energy difference between the VB of NCs and HOMO of GO-Cys, the possibility of hole transfer in $FAPbBr_3$ NCs/GO-Cys heterostructure is the easiest amongst all other heterostructures. These findings are also in agreement with the PL and TRPL studies, where a strong PL quenching and greater k_{CT} has been observed in case of $FAPbBr_3$ NCs/GO-Cys heterostructure.

3.3.5 Summary

In the present section, the CT dynamics in $FAPbBr_3$ NCs/functionalized graphene heterostructures were elaborated. Herein, various functionalized graphene i.e., GO, GO-Cys, GO-Ala and GO-Tyr, were prepared and their heterostructures were assembled with $FAPbBr_3$ NCs. The PL quenching of photoexcited $FAPbBr_3$ NCs when coupled with functionalized graphene occurred indicating the quenching ability of functionalized graphene. The PL quenching occurred due to photoexcited CT. The CT efficiency and CT rate were also evaluated by PL decay kinetics analysis. The comparative values of k_{CT} are 2.30×10^7, 9.04×10^7, 1.09×10^8, 2.97×10^8 s^{-1} for NCs/GO, NCs/GO-Ana, NCs/GO-Tyr, and NCs/GO-Cys, respectively, indicating the highest k_{CT} was observed for NCs/GO-Cys heterostructure. This led to conclude the E_{CT} and k_{CT} in NCs/surface decorated graphene heterostructures were highly dependent on the nature of functionalizing moiety. Amongst all functionalized graphene, GO-Cys possessed the highest E_{CT}, 88.84 % and the lowest with the GO, 38.15 %. These results showed that GO-Cys is the best charge acceptor amongst all other functionalized graphene samples. The CV measurements demonstrated the PL of the $FAPbBr_3$ NCs was quenched due to the photoexcited hole transfer from the NCs to the functionalized graphene. From these results we concluded that the functionalized graphene can not only act as hole acceptor material in light harvesting assemblies when combined with $FAPbBr_3$ NCs but their hole accepting ability can also be tuned by selecting a suitable surface ligand molecule. The present work elucidates the fundamental understanding of photoinduced hole transfer in perovskites NCs/functionalized graphene heterostructures that will help to understand the type of CT in multiple nanostructured heterojunctions.

3.4 Low temperature processed $FAPbBr_3$ perovskites based solar devices and their water splitting application

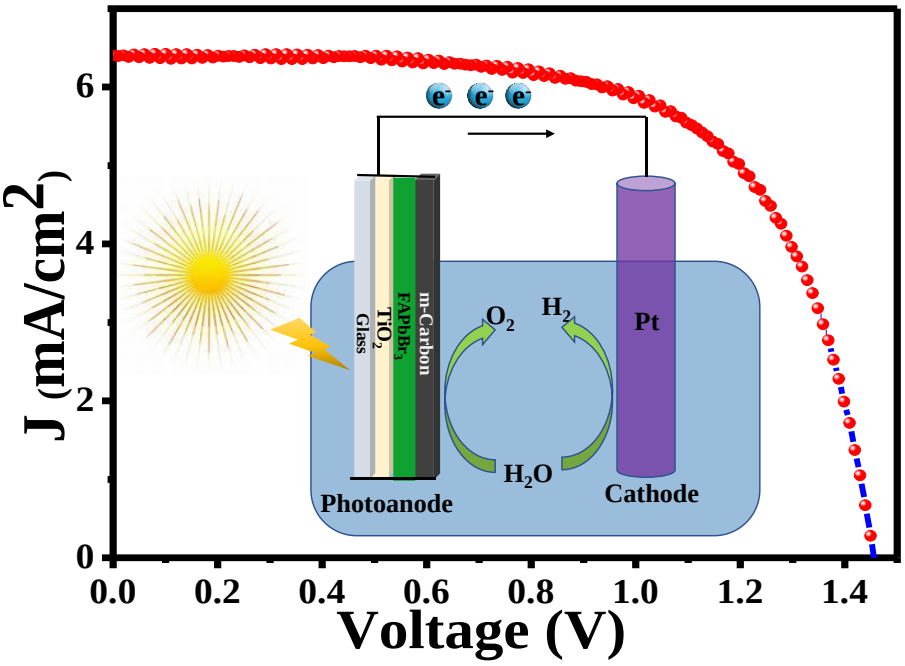

The present section describes the detail characterization of low temperature processed $FAPbBr_3$ based solar device. The FTO/TiO_2/$FAPbBr_3$/m-carbon architecture-based device is successfully fabricated and 6.11 % device power conversion efficiency with equivalence quantum efficiency (EQE) of 60 % is achieved. The graphite sheet modified with Ir-based water oxidation catalyst (WOC) protected photoanode of the fabricated device is applied to study the photoelectrochemical (PEC) water oxidation. The photoanode possessed better water oxidation properties in the presence of catalyst with low onset potential. The small amount of oxygen evolved during PEC water oxidation is also detected by oxygen sensing electrode also confirming the oxygen generation because of water splitting. Hence, the present fabricated device potentially be used for light harvesting applications.

3.4.1 Characterization of $FAPbBr_3$ perovskites based solar device

The XRD patterns of the FTO/TiO_2, $PbBr_2$, and $FAPbBr_3$ films are presented in figure 3.4.1. The XRD pattern of the perovskites is recorded after growing it on the surface of FTO/TiO_2 layers and the XRD patterns of successive layers are presented in figure 3.4.1. The XRD pattern of the $FAPbBr_3$ film is well indexed with cubic crystalline phase and matched with the standard JSPDS card no. 01-087-0158.[206] The standard diffraction peaks of the reference are also presented in the same graph for comparison. The peaks of FTO/TiO_2 in the XRD pattern of $FAPbBr_3$ are represented as diamond sign with the diffraction peaks of perovskite. The absence of $PbBr_2$ diffraction peaks in the diffraction pattern of perovskites show the complete transformation of the $PbBr_2$ into perovskites with a new crystal phase and diffraction peaks.

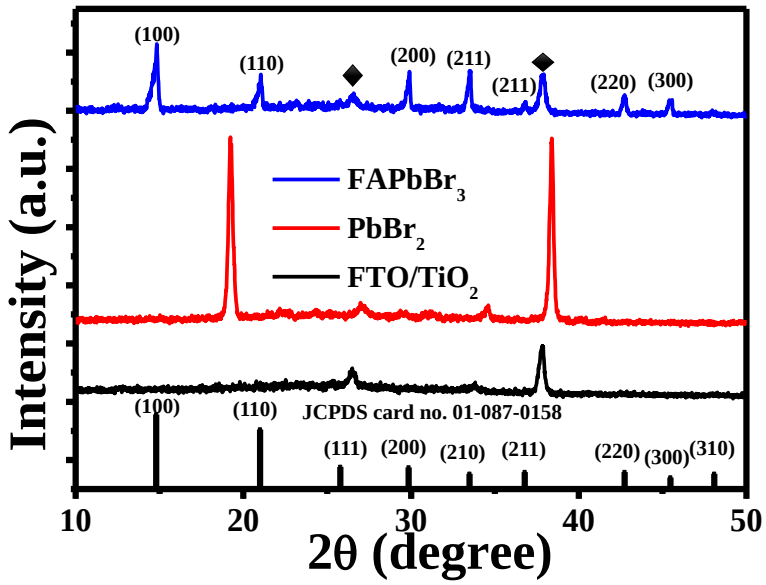

Figure 3.4.1) XRD patterns of the FTO/TiO_2, $PbBr_2$, and $FAPbBr_3$ film grown on FTO/TiO2/$PbBr_2$ substrate, The FTO/TiO_2 peaks are shown by diamond marker.

The morphology with crystallinity also plays an important role in the properties and efficiency of the solar devices. To get information about the morphology of the perovskites layer grown on the surface of the substrate FTO/TiO_2, the SEM analysis was carried out and micrographs are displayed in figure 3.4.2. The different resolution images are presented. The micrographs represented the surface coverage of perovskites on the substrate. The particles are distributed homogeneously. The particles possessed the cuboidal morphology containing cubes of different sizes. Interestingly, some

particles are possessed the distinctly large cuboidal morphology on the surface of the film. The SEM micrographs show that the perovskites particles are grown well, possessing homogeneous coverage of cuboidal particles on the surface of substrates.

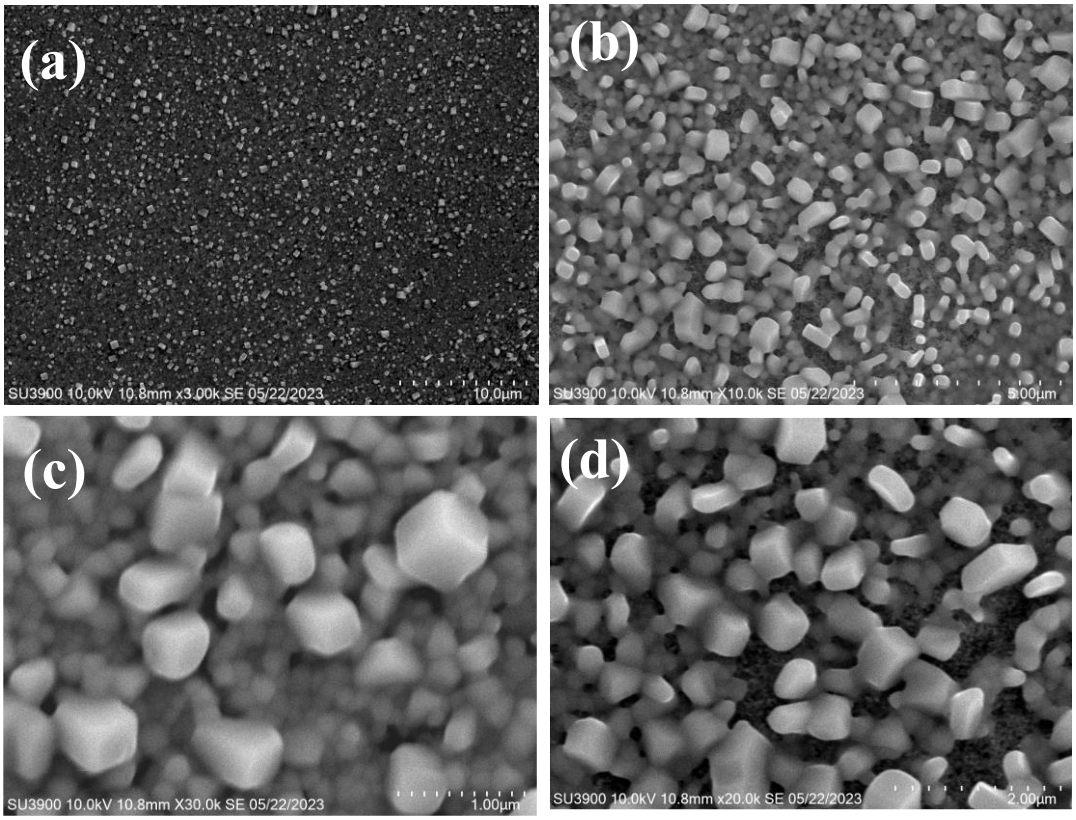

Figure 3.4.2 (a-d) SEM micrographs of $FAPbBr_3$ grown on FTO/TiO_2 substrate at different resolution.

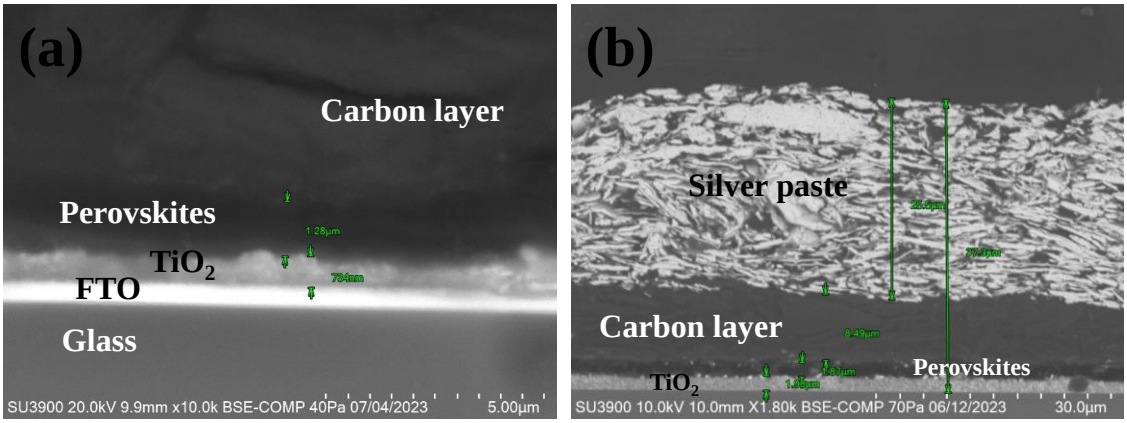

Figure 3.4.3 Cross sectional SEM micrographs of $FAPbBr_3$ based carbon device, (a) from center, and (b) from edge of device.

The planar carbon-based solar devices with an n-i-p architecture of FTO/TiO_2/$FAPbBr_3$/m-carbon were made. The absorber layer of $FAPbBr_3$ is sandwiched between electron collecting TiO_2 and hole transport layer is of commercial carbon paste consisting of graphite and carbon black. The cross-sectional SEM micrograph of the fabricated device is presented in figure 3.4.3 representing the thickness of the constituent layers. The J-V curves and EQE of the device are represented in figure 3.4.4 (a-b). The champion device achieved a PCE of 6.43 %. For comparison, the results of four devices formed together are also presented in table 3.4.1. From these results, we can conclude that an average PCE of the devices is about 6 %. For comparison with the present work, the parameters of reported devices are tabulated in table 3.4.2. The devices are produced at low temperature and using cost effective approach using carbon paste instead of using expensive hole transport layer and thermal evaporated counter electrode. Although to date the cesium lead bromide-based perovskites carbon devices utilizing multistep spin coating, are a bit stable, possessing better PCE but the perovskites' annealing temperature is high. These devices are fabricated at low annealing temperature. So, we can be the substitute of present devices possessing comparable PCE with high OCV of about 1.47 V and simple cost-effective processing method are a better substitute of expensive thermal evaporated silver or gold based $FAPbBr_3$ perovskites devices and high temperature annealed $CsPbBr_3$-carbon based devices. The device stability of devices is also monitored by measuring the JV performance at regular interval of 4 weeks. The devices are stored at room conditions. The obtained results show that the devices still possessed the same PCE after 4 weeks. The EQE of the champion device is recorded at different frequencies from 5 Hz to 600 Hz. By increasing the chopper frequency, a sudden decrease of EQE from about 65 to 55 percent is observed and by further rise in frequency the EQE is nearly become constant.

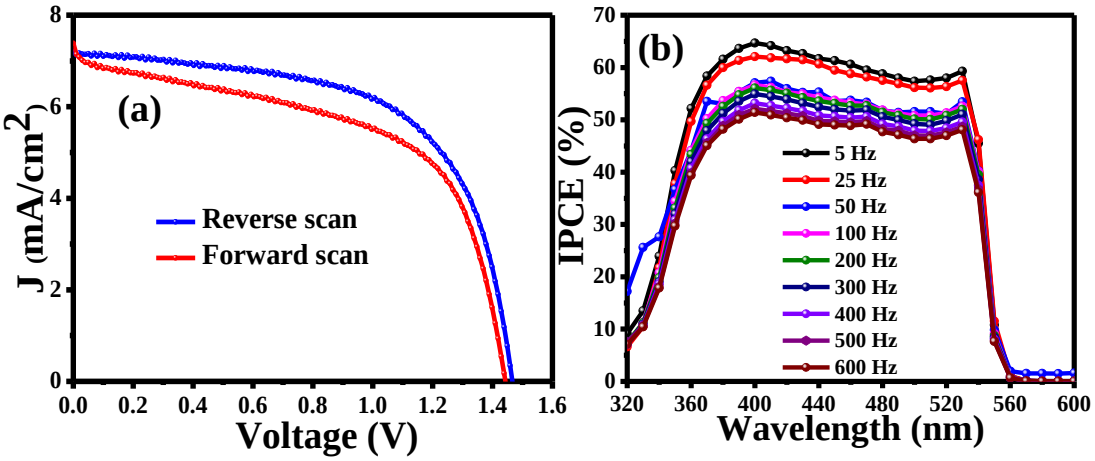

Figure 3.4.4 (a) J-V curve and (b) IPCE curves of perovskite device.

Table 3.4.1 Device characterization parameters of solar devices.

Sample	OCV (V)	J (A/cm^2)	FF	PCE (%)	Hysteresis (%)
1-Reverse scan	1.47	7.20	61	6.43	6.22
1-Forward scan	1.45	7.30	57	6.03	-
2-Reverse scan	1.47	6.91	63	6.35	3.46
2-Forward scan	1.46	7.00	60	6.13	-
3-Reverse scan	1.49	6.49	65	6.26	9.44
3-Forward Scan	1.47	6.49	60	5.72	-
4-Reverse scan	1.47	6.80	63	6.31	9.19
4-Forward scan	1.44	6.86	58	5.73	-

Table 3.4.2 A comparison of devices reported in literature with the present fabricated device.

Perovskite device architecture	**Method used to deposit film of perovskite**	**V_{OC} (V)**	**J_{SC} (mA/cm^2)**	**FF**	**PCE (%)**	**Reference**
FTO/TiO_2/$FAPbBr_3$/Spiro-MeOTAD/Au	One-step	1.32	6.30	0.69	5.70	211
FTO/NiO/$FAPbBr_3$/ZnO/ Ag	One step	1.23	9.90	0.55	6.73	212
ITO/P_3CT/$FAPbBr_3$/ PCBM/C60/BCP/Cu	Two-step	1.49	8.98	0.66	8.93	213
FTO/SnO_2/$FAPbBr_3$/spiro/ Au	Two-step	1.55	8.94	0.76	10.61	214
FTO/c-TiO_2/Li-m-TiO_2/ $FAPbBr_3$/spiro/Au	Two-step	1.53	7.30	0.71	8.20	215
FTO/c-TiO_2/m-TiO_2/ $FAPbBr_3$/spiro/Au	Two-step	1.42	6.80	0.72	7.00	216
FTO/c-TiO_2/m-TiO_2/$FAPbBr_3$/ SO7/Au	Two-step	1.50	6.90	0.69	7.10	217
FTO/NiO/$FAPbBr_3$/Mg-ZnO/ PCBM/BCP/Ag	One-step	1.44	8.92	0.71	9.06	218
This work	**Two-step**	**1.47**	**7.20**	**0.61**	**6.43**	**This work**
FTO/SnO_2/GQDs/ $CsPbBr_3$/Carbon	Two-step	1.52	7.91	0.78	9.51	219
FTO/c-TiO_2/m-TiO_2/ Sm-$CsPbBr_3$/Carbon	Two-step	1.59	7.48	0.85	10.14	220
FTO/c-TiO_2/m-TiO_2/ $CsPbBr_3$/Carbon	Two-step	1.58	7.42	82.11	9.65	221

FTO/c-TiO_2/m-TiO_2/ $CsPbBr_3$/Carbon	Two-step	1.43	7.86	0.81	6.78	222
FTO/c-TiO_2/m-TiO_2/ m-ZrO2/$CsPbBr_3$/Carbon	Two-step	1.44	7.75	73.52	8.19	223
FTO/c-TiO2/m-TiO_2/ $CsPbBr_3$/P_3HT-ZnPc/ Carbon	Two-step	1.57	7.65	83.06	10.03	224
ITO/c-TiO_2/$CsPbBr_3$/ Carbon	Mist-CVD	1.51	7.30	0.75	8.3	225
FTO/c-TiO_2/m-TiO_2/ $CsPbBr_3$/Carbon-MWCNT	Two-step	1.43	6.84	0.78	7.62	226

The absorption of perovskites is also important as it provides the information about the absorbing spectral region of the solar light. The absorption spectrum and corresponding tauc plot of the $FAPbBr_3$ film is presented in figure 3.4.6 (a-b). The perovskite shows an excitonic peak at 525 nm with a corresponding band gap of 2.2 eV.

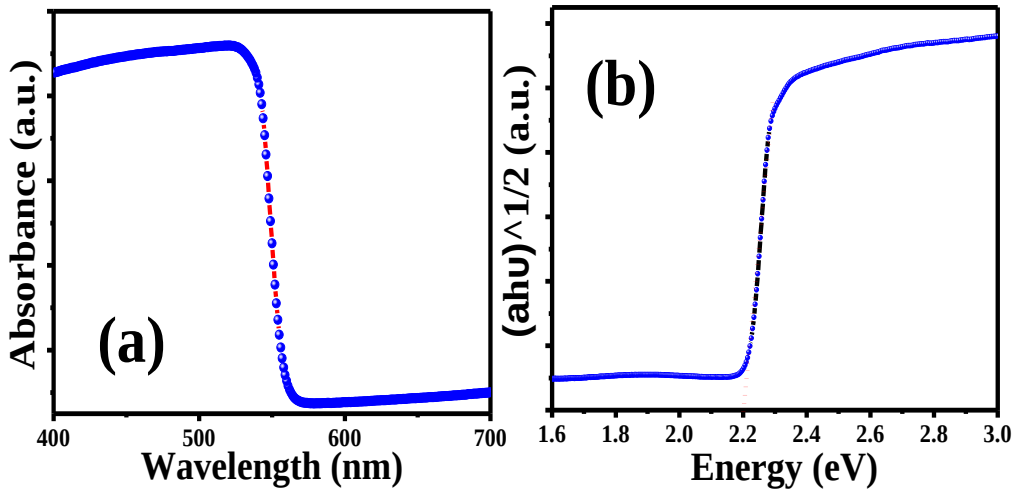

Figure 3.4.5 (a) Absorption spectrum and (b) Tauc plot of $FAPbBr_3$ film.

The PL and time resolved spectroscopy is an important tool to study the CT dynamics of the charge carrier in semiconductor materials. The PL and decay kinetics of the charge carrier are represented in figure 3.4.7 (a-b). The carrier dynamins of perovskites $FAPbBr_3$, perovskites combine with electron transport layer (ETL) (TiO_2/$FAPbBr_3$)

and perovskites sandwiched between electron and hole transport layer (TiO_2/$FAPbBr_3$/carbon) were recorded. All the samples are excited from the FTO side. The $FAPbBr_3$ perovskites film show a PL peak maximum at 558 nm. When the electron transport TiO_2 layer is also accompanied with perovskites layer, the PL of the perovskites is quenched and when perovskites layer is sandwiched between ETL and HTL, a small PL intensity is observed. The sharp decrease in PL of perovskites by combining it with HTL and ETL indicated that the charge carrier is successively transferred from perovskites to respective hole and electron transfer layers. The decay kinetics of the charge carriers are fitted by biexponential decay model. The average PL lifetime in case of $FAPbBr_3$ is 5.16 ns that is reduced to 1.84 ns when accompanying with ETL also indicating that the charge carriers are moving from perovskites to ETL. When perovskites layer is sandwiched between ETL and HTL, the decay time of the charge carriers becomes 0.89 ns, indicating the successive transfer of charge carriers to their respective layers.

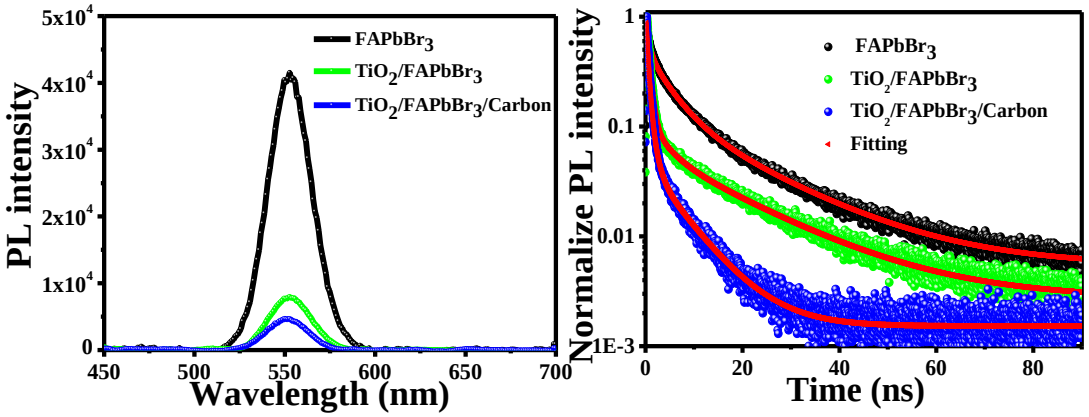

Figure 3.4.6 (a) PL spectra and (b) Decay kinetics of $FAPbBr_3$ film, TiO_2/$FAPbBr_3$ and TiO_2/$FAPbBr_3$/m-carbon.

3.4.2 Photoelectrochemical water oxidation studies

To study the photoelectrochemical (PEC) water oxidation application, the photoanodes with a configuration of TiO_2/$FAPbBr_3$/m-carbon was prepared and protected from aqueous environment to perform electrochemical studies by using 160 µm thick graphite sheet (GS-160). To assist the water splitting and promote the oxygen evolution reaction (OER), the use of water oxidation catalyst (WOC) is highly recommended.[227] For this purpose, GS-160, before applying to the photoanode, was dipped in commercially available Ir-WOC overnight to facilitate the attachment of the

catalyst with GS-160. The electrochemical experiment was carried out by using three electrode system employing TiO_2/$FAPbBr_3$/m-carbon/GS-160 as photoanode, Ag/AgCl as reference and platinum wire as counter electrode. The 0.1 M KNO_3 solution at a pH of 2.5 (pH adjusted by adding few drops of HNO_3) was used as electrolyte. The obtained electrochemical results are displayed in figure 3.4.7. The electrochemical experiment was carried in dark and in light by one sun illumination light source. From LSV and CV results displayed in figure 3.4.8.(a and c), we can infer that there is an observable difference in photoelectrochemical current in the absence and in the presence of light. In the presence of catalyst not only the photocurrent signal increases but also the onset potential for water oxidation also reduced as displayed in figure 3.4.8.(b). The step up chronoamperometry measurements were also carried out from 0 to 1.4 V with respect to RHE, where voltage was stepped up 0.2 V at every 5 minutes and displayed in figure 3.4.7 (d). This result shows that the current change at initial voltages (0 to 0.6V) is many folds then at higher voltages indicating that the reaction is performing well and gives appreciable photocurrent at lower voltage inferring that small driving force of applied voltage is sufficient to carry out a OER and gives a better current response. The open circuit potential measurement recorded at applied 0 current with and without surface modification of GS with catalyst and photo-voltage is calculated. The value of photo-voltage calculated is 1.35 V and 1.25 V in the presence and in the absence of catalyst, respectively.

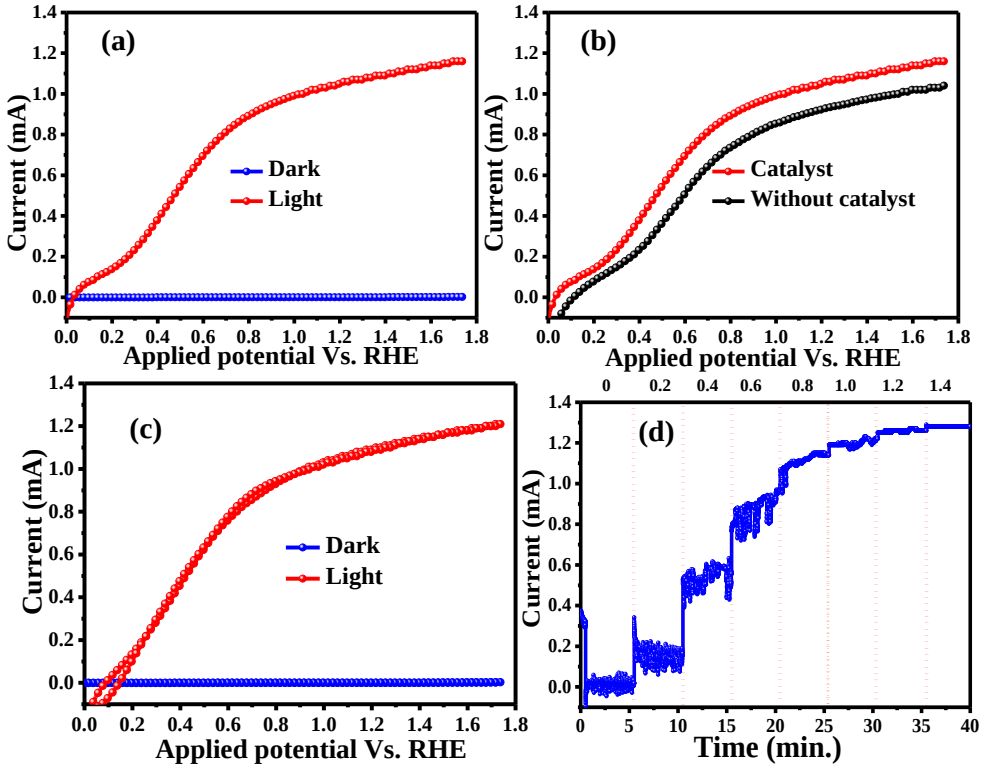

Figure 3.4.7 (a) LSV of the photo-anode in dark and light at 50 mV/s (b) LSV of photo-anode in light with and without catalyst attached to the GS-160 at 50 mV/s (c) CV of the photo-anode in dark and light at 50 mV/s. (d) Chronoamperometry measurements of photo-anodes modified with catalyst from 0 to 1.4 V with reference to RHE. (The voltage was successively increased 0.2 V every 5 minutes).

The photocurrent response of the photo-anode in electrochemical working conditions (in three electrode configurations with 0.1 M KNO_3 at pH 2.5 was also recorded and the resultant calculated EQE at a chopping frequency of 5 Hz are displayed in figure 3.4.8 (a-b). For comparison with normal solar cell and with cell working as photo-anode in three electrode configurations in electrochemical conditions, a comparative EQE spectra are presented in figure 3.4.8(a) indicating a decrease in EQE because of the changing working conditions. A decrease in EQE from 60 to 30 percent was observed. By performing the measurement at various applied potentials from -0.2 to 0.95 V Vs. Ag/AgCl, a rise in photocurrent is observed as a results EQE also increased. At smaller values of applied potentials, from -0.2 to 0.25 V, the rise in photocurrent and the resultant EQE is more observable than at higher values. This data agrees with the data of the stepped up chronoamperometry measurements indicating

that at lower applied voltages, the rise in photocurrent is more appreciable than at higher applied voltages, current in the electrochemical system.

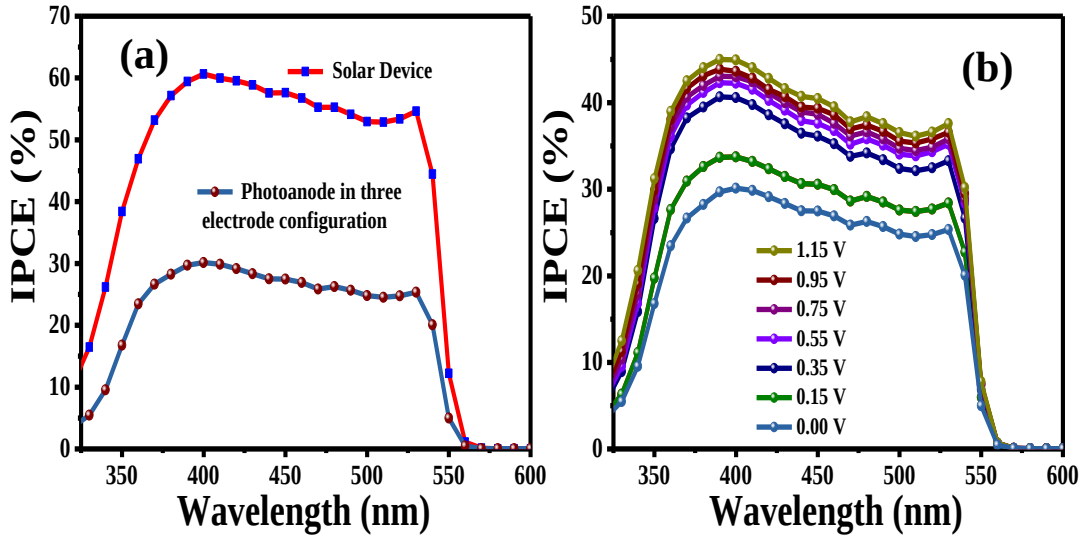

Figure 3.4.8 (a) A comparison of EQE of the TiO_2/$FAPbBr_3$/m-carbon in solar device configuration, and TiO_2/$FAPbBr_3$/m-carbon/GS-160/Ir-WOC in three electrode configurations in 0.1 MKNO_3 at 2.5 pH, (b) TiO_2/$FAPbBr_3$/m-carbon/GS-160/Ir-WOC in three electrode configurations in 0.1 MKNO_3 at 2.5 pH at various applied voltages Vs. Ag/AgCl.

To detect the amount of oxygen produced, the oxygen detection electrode was employed. The oxygen gas produced in the closed system was circulated and carried out to the detecting electrode by using nitrogen as carrier gas. The chronoamperometry at 1.23V Vs RHE was carried out for photoanode and for oxygen sensing electrochemical electrode, the chronoamperometry was conducted at -0.66 V. First the nitrogen is purged and circulated through the system to remove the air that also contains oxygen. The current signal for air containing 21 % oxygen is about 450 nA. By purging nitrogen, for 20 minutes at a flow rate of 30 cm^3/min, the current signal reduces to 0 A. The oxygen electrode is sensitive to molecular oxygen and at -0.66 V applied voltage, the reduction of the oxygen takes place, hence carrying out the oxygen reduction reaction giving a negative signal of the current. When nitrogen atmosphere is created in the electrochemical system, the current signal dropped to zero in 20 minutes after that the detector detect the small amount of oxygen produced in the electrochemical system by 1 sun light illumination of photoanode at an applied voltage of 1.23 V Vs RHE. The chronoamperometric measurement of photoanode for about 150 minutes

with consistent working is displayed in figure 3.4.10 (a) and the chronoamperometric trace of oxygen detecting electrode is displayed in figure 3.4.10 (a). Although the observed current response is about 175 nA, however it confirms the oxygen production in the electrochemical system. From the current response, the moles of oxygen generated because of water oxidation is calculated by using the Faradays laws of electrolysis. The obtained plot is presented in figure 3.4.10 (b).

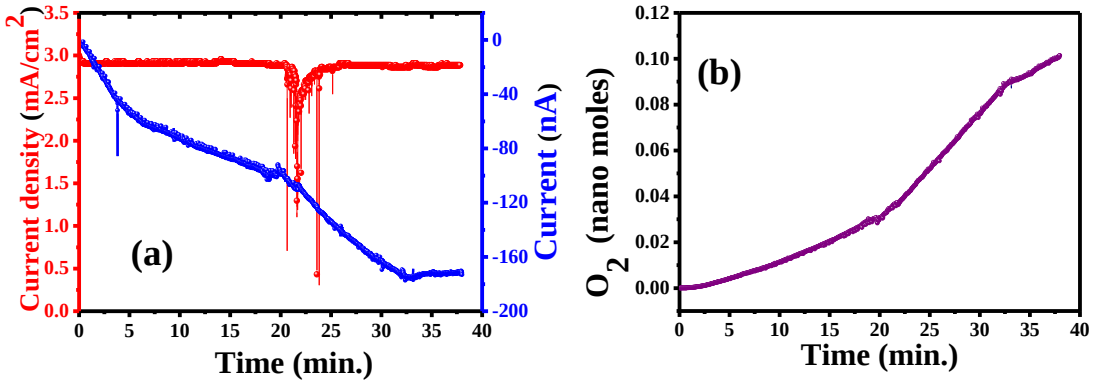

Figure 3.4.9 (a) red trace, Chronoamperometry measurement of photoanode TiO_2/FApbBr$_3$/m-carbon/GS-160/Ir-WOC recorded at an applied potential of 1.23 V Vs. RHE in 0.1 M KNO_3 at pH 2.5 under 1 sun solar irradiation (AM 1.5G, 100 mWcm^{-2}), blue trace, Chronoamperometry measurements to detect O_2 production. (The nitrogen is purged for up to 20 minutes to remove the O_2 signal coming from air after that the O_2 produced inside system is detected), and (b) Moles of oxygen generated because of water oxidation, calculated by using the Faraday's law of electrolysis.

3.4.3 Summary

The low temperature processed FAPbBr$_3$ based solar device was fabricated successfully with a device architecture of FTO/TiO_2/FAPbBr$_3$/m-carbon and 6.11 % device power conversion efficiency with equivalence quantum efficiency (EQE) of 60 % was achieved. When the graphite sheet modified with Ir-based WOC protected photo-anode of the fabricated device was studied for the photoelectrochemical (PEC) water oxidation, a better current response in the presence of catalyst with low onset potential was observed indicating that the photo-anode possessed better water oxidation properties in the presence of catalyst. The sensing of evolved oxygen as result of PEC oxidation also confirmed the oxygen generation because of water splitting. Hence, the present fabricated device can potentially be used for light-harvesting applications.

4. Conclusion

CT is an important phenomenon effecting the efficiency of optoelectronic devices. The present studies described this important phenomenon in different perovskites/graphene heterostructures. Here, the heterojunction of halide perovskites crystals with un-functionalized and functionalized graphene were studied. In the heterostructures of $CsPbBr_3$/N-Gr, PL quenching of NCs was observed due to transfer of electron from CB of the NCs to the LUMO of the N-Gr as supported by CV analysis. This work also demonstrated the synthesis and vital understanding of the electron transfer in organic-inorganic halide NCs/Gr heterostructures. The successive introduction of graphene in NCs resulting in PL quenching of $FAPbBr_3$ NCs that was attributed to the electron transfer from the CB of the NCs to LUMO of the Gr in $FAPbBr_3$ NCs/Gr heterostructures arising because of the type-I band alignment of the components of the heterostructures. The significant reduction in CT resistance made the process of electron transfer more facile, as evaluated by EIS analysis. Also, various functionalized graphene i.e., GO, GO-Cys, GO-Ala and GO-Tyr, were prepared and their heterostructures were assembled with $FAPbBr_3$ NCs. The PL quenching of photoexcited $FAPbBr_3$ NCs when coupled with functionalized graphene occurred due to photoexcited hole transfer. From these results we concluded that the functionalized graphene can not only act as hole acceptor material in light-harvesting assemblies when combined with $FAPbBr_3$ NCs but their hole accepting ability can also be tuned by selecting a suitable surface decorated molecule. Lastly, the FTO/TiO_2/$FAPbBr_3$/graphite paste based perovskite solar cell device was fabricated that possessed 6.43 % power conversion efficiency with an open circuit potential of 1.47 V and external quantum efficiency of about 65%. The FTO/TiO_2/$FAPbBr_3$/Carbon/graphite sheet/water oxidation catalyst photo-anodes was fabricated and employed to study the photoelectrochemical (PEC) water oxidation. The device showed a better performance in PEC water oxidation indicating the practicability of these devices to generate fuel by utilizing sunlight. The present work elucidates the fundamental understanding of photoinduced CT in perovskites/graphene heterostructures that will help to understand the type of CT in multiple nanostructured heterojunctions and the practical applications of such heterostructure in solar light driven energy applications.

5. Recommendations/Future perspective

The work presented here describes the utility of graphene/perovskites heterostructures as discussed above. From the performed experiments and discussed results, the following recommendations are made.

The graphene/perovskites heterostructure can effectively be used hole layer free perovskites solar cells. It also reduces the cost of expensive method used for metal evaporation.

In perovskites solar cells, an efficient hole transport layer is still a challenge that can be overcome by using cheap graphene and its derivatives.

The perovskites NCs possess tunable band gap and better environment stability due to surface passivation by ligand in comparison to bulk perovskites crystal.

Capping of perovskites provide defect passivation as well as functionalization to attach multidimensional materials with perovskites.

CVD grown graphene might be a better substitutes of expensive hole transport layer as well as metal evaporated top contact.

6. References

(1) Meyer, J. C.; Geim, A. K.; Katsnelson, M. I.; Novoselov, K. S.; Booth, T. J.; Roth, S. The structure of suspended graphene sheets. *Nature* **2007**, 446, *60*–63.

(2) Mensah, B.; Gupta, K. C.; Kim, H.; Wang, W.; Jeong, K.; Nah, C. Graphene-reinforced elastomeric nanocomposites: a review. *Polym. Test* **2018**, *68*, 160–184.

(3) Ren, S.; Rong, P.; Yu, Q. Preparations, properties, and applications of graphene in functional devices: a concise review. *Ceram. Int.* **2018**, *44*, 11940–11955.

(4) Novoselov, K. S.; Geim, A. K.; Morozov, S.V.; Jiang, D.; Zhang, Y.; Dubonos, S. V.; Grigorieva, I. V.; Firsov A. A. Electric field effect in atomically thin carbon films. *Science* **2004**, *306*, 666–669.

(5) Hiew, B. Y. Z.; Lee, L. Y.; Lee, X. J., Thangalazhy-Gopakumar, S.; Gan, S.; Lim, S. S.; Pan, G. T.; Yang, T. C-K.; Chiu, W. S.; Khiew, P. S. Review on synthesis of 3D graphene-based configurations and their adsorption performance for hazardous water pollutants. *Process Saf. Environ.* **2018**, *116*, 262–286.

(6) Dasari, B. L.; Nouri, J. M.; Brabazon, D.; Naher, S.; Graphene and derivatives – Synthesis techniques, properties, and their energy applications. *Energy* **2017**, *140*, 766–778.

(7) Zhao, L.; Yu, B.; Xue, F.; Xie, J.; Zhang, X.; Wu, R.; Wang, R.; Hu, Z.; Yang, S-T.; Luo, J. Facile hydrothermal preparation of recyclable S-doped graphene sponge for Cu^{2+} adsorption. *J. Hazard Mat.* **2015**, *286*, 449–456.

(8) Li, Z.; Zhang, W.; Li, Y.; Wang, H.; Qin, Z. Activated pyrene decorated graphene with enhanced performance for electrochemical energy storage. *Chem. Eng. J.* **2018**, *334*, 845–854.

(9) Yang, W.; Zhao, Q.; Xin, L.; Qiao, J.; Zou, J.; Shao, P.; Yu, Z.; Zhang, Q.; Wu, G. Microstructure and mechanical properties of graphene nanoplates reinforced pure Al matrix composites prepared by pressure infiltration method. *J. Alloy Compd.* **2018**, *732*, 748–758.

(10) Chowdhury, S.; Balasubramanian, R. Recent advances in the use of graphene–family nano adsorbents for removal of toxic pollutants from wastewater. *Adv. Colloid Interface* **2014**, *204*, 35–56.

(11) Geim, A. K.; Novoselov, K. S. The rise of graphene. *Nat. Mater.* **2007**, *6*, 183–191.

(12) Cardinali, M.; Valentini, L.; Fabbri, P.; Kenny.; J. M. Radiofrequency plasma assisted exfoliation and reduction of large-area graphene oxide platelets produced by a mechanical transfer process. *Chem. Phys. Lett*. **2011**, *508*, 285–288.

(13) Dikin, D. A.; Stankovich, S.; Zimney, E. J.; Piner, R. D.; Dommett, G. H. B.; Evmenenko, G.; Nguyen, S. T.; Ruoff, R. S. Preparation and characterization of graphene oxide paper. *Nature* **2007**, *448*, 457.

(14) Dreyer, D. R.; Park, S.; Bielawski, C. W.; Ruoff, R. S. The chemistry of graphene oxide. *Chem. Soc. Rev.* **2010**, *39*, 228.

(15) Park, S.; Ruoff, R. S. Making graphene on large scale. *Nat. Nanotechnol.* **2009**, *4*, 217.

(16) Allen, M. J.; Tung, V. C.; Kaner, R. B. Honey comb carbon: A review on graphene. *Chem. Rev.* **2010**, *110*, 132.

(17) Compton, O.C.; Nguyen, S. T. Graphene oxide, highly reduced graphene oxide, and graphene: versatile building blocks for carbon-based materials. *Small* **2010**, *6*, 711.

(18) Li, S. L.; Yan, X. Graphene based nano assemblies for energy conversion. *J. Phys. Chem. Lett*. **2010**, *1*, 2572.

(19) Hamilton, I. P.; Li, B. S.; Yan, X.; Li, L. S. Alignment of colloidal graphene quantum dots on polar surfaces, *Nano Lett*. **2011**, *11*, 1524.

(20) Zhou, S. Y.; Gweon, G. H.; Fedorov, A. V.; First, P. N.; De Heer, W. A.; Lee, D. H.; Guinea, F.; Neto, A. H. C.; Lanzara, A. Substrate-induced bandgap opening in epitaxial graphene. *Nat. Mater.* **2007**, *6*, 770.

(21) Chang, X. Y.; Sun, Z. H.; Yuan, Q. H.; Ding, F.; Tao, M. X.; Yan, F.; Zheng, Z. J. Ultraviolet, visible, and near infrared photoresponse properties of solution processed graphene oxide. *Adv. Mater*. **2010**, *22*, 4872.

(22) Kuila, T.; Bose, S.; Mishra, A. K.; Khanra, P.; Kim, N. H.; Lee, J. H. Chemical functionalization of graphene and its applications. *Prog. Mater. Sci.* **2012**, *57*, 1061–105.

(23) Ramezani, M.; Alibolandi, M.; Nejabat, M.; Charbgoo, F.; Taghdisi, S.M.; Abnous, K. Graphene-Based Hybrid Nanomaterials for Biomedical Applications. In *Biomedical Applications of Graphene and 2D Nanomaterials*; Nurunnabi, M., McCarthy, J.R., Eds.; Elsevier: Amsterdam, The Netherlands, **2019**; Chapter 6; 119–141.

(24) Berger, C.; Song, Z. M.; Li, X. B.; Wu, X. S.; Brown, N.; Naud, C.; Mayou, D.; Li, T. B.; Hass, J.; Marchenkov, A. N.; Conrad, E. H.; First, P. N.; De Heer, W. A. Electronic confinement, and coherence in patterned epitaxial graphene. *Science* **2006**, *312*, 1191.

(25) Emtsev, K. V.; Bostwick, A.; Horn, K.; Jobst, J.; Kellogg, G. L.; Ley, L.; McChesney, J. L.; Ohta, T.; ReshanE.; Schmid, A. K.; Waldmann, D.; Weber, B.; Seyller, T. Towards wafer-size graphene layers by atmospheric pressure graphitization of silicon carbide. *Nat. Mater.* **2009**, *8*, 203.

(26) Reina, A.; Jia, X. T.; Ho, J.; Nezich, D.; Son, H. B.; Bulovic, V.; Dresselhaus, M. S.; Kong, J. Large area, few-layer graphene films on arbitrary substrates by chemical vapor deposition. *Nano Lett*. **2009**, *9*, 30.

(27) Sun, Z. Z.; Yan, Z.; Yao, J.; Beitler, E.; Zhu, Y.; Tour, J. M. Growth of graphene from solid carbon sources. *Nature* **2010**, *468*, 549.

(28) Su, C. Y.; Lu, A. Y.; Wu, C. Y.; Li, Y. T.; Liu, K. K.; Zhang, W. J.; Lin, S. Y.; Juang, Z. Y.; Zhong, Y. L.; Chen, F. R.; Li, L. J. Direct formation of wafer scale graphene thin layers on insulating substrates by chemical vapor deposition. *Nano Lett.* **2011**, *11*, 3612.

(29) Li, X. L.; Cai, W. W.; An, J. H.; Kim, S.; Nah, J.; Yang, D. X.; Piner, R.; Velamakanni, A.; Jung, I.; Tutuc, E.; Banerjee, S. K.; Colombo, L.; Ruoff, R. L. Large-area synthesis of high-quality and uniform graphene films on copper foils. *Science* **2009**, *324*, 1312.

(30) Reina, A.; Jia, X. T.; Ho, J.; Nezich, D.; Son, H. B.; Bulovic, B.; Dresselhaus M. S.; Kong, J. Large area, few-layer graphene films on arbitrary substrates by chemical vapor deposition. *Nano Lett*. **2009**, *9*, 30.

(31) Sun, Z. Z.; Yan, Z.; Yao, J.; Beitler, E.; Zhu, Y.; Tour, J.M. Growth of graphene from solid carbon sources. *Nature* **2010**, *468*, 549.

(32) Su, C. Y.; Lu, A. Y.; C. Wu, C. Y.; Li, Y. T.; Liu, K. K.; Zhang, W. J.; Lin, S. Y.; Juang, Z. Y.; Zhong, Y. L.; Chen, F. R.; Li, L. J. Direct formation of wafer scale graphene thin layers on insulating substrates by chemical vapor deposition. *Nano Lett.* **2011**, *11*, 3612.

(33) Stankovich, S.; Dikin, D. A.; Piner, R. D.; Kohlhaas, K. A.; Kleinhammes, K. A.; Jia, Y.; Wu, Y.; Nguyen, S. T.; Ruoff, R. S. Synthesis of graphene-based nanosheets via chemical reduction of exfoliated graphite oxide. *Carbon* **2007**, *45*, 1558.

(34) Ren, W.; and Cheng, H. M. The global growth of graphene. *Nature nanotech*. **2014**, *9*, 726-730.

(35) Nirmalraj, P.N.; Lutz, T.; Kumar, S.; Duesberg, G. S.; and Boland, J. J. Nanoscale mapping of electrical resistivity and connectivity in graphene strips and networks. *Nano letters* **2011**, *11*, 16-22.

(36) Geng, X.; Niu, L.; Xing, Z.; Song, R.; Liu, G.; Sun, M.; Cheng, G.; Zhong, H.; Liu, Z. Zhang, Z.; and Sun, L. Aqueous-processable noncovalent chemically converted graphene–quantum dot composites for flexible and transparent optoelectronic films. *Adv. Mater.* **2010**, *22*, 638-642.

(37) Chang, H.; Wu, H. Graphene-based nanomaterials: synthesis, properties, optical and optoelectronic applications. *Adv. Funct. Mater*. **2012**, *13*, 1984-1997.

(38) Boukhvalov, D. W.; Katsnelson, M.I. Enhancement of chemical activity in corrugated graphene. *J. Phy. Chem. C* **2009**, *113*, 14176-14178.

(39) Neto, A.C.; Guinea, F.; Peres, N. M.; Novoselov, K. S.; Geim, A.K. The electronic properties of graphene. *Rev. Mod. Phys.* **2009**, *81*,109.

(40) Han, Z.; Kimouche, A.; Allain, A.; Arjmandi-Tash, H.; Reserbat-Plantey, A.; Pairis, S.; Reita, V.; Bendiab, N.; Coraux, J.; Bouchiat, V. Suppression of

multilayer graphene patches during CVD graphene growth on copper. *Cond. Mater.* **2012**, *1205*, 1337.

(41) Bai, J.; Liao, L.; Zhou, H.; Cheng, R.; Liu, L.; Huang, Y.; Duan, X. Top-gated chemical vapor deposition grown graphene transistors with current saturation. *Nano lett.* **2011**, *11*, 2555-2559.

(42) Liao, L.; Bai, J.; Cheng, R.; Lin, Y.C.; Jiang, S.; Huang, Y.; Duan, X.; Top-gated graphene nanoribbon transistors with ultrathin high-k dielectrics. *Nano lett.* **2010**, *10*, 1917-1921.

(43) Balog, R.; Jørgensen, B.; Nilsson, L.; Andersen, M.; Rienks, E.; Bianchi, M.; Fanetti, M.; Lægsgaard, E.; Baraldi, A.; Lizzit, S.; Sljivancanin, Z. Bandgap opening in graphene induced by patterned hydrogen adsorption. *Nature mater*. **2010**, *9*, 315-319.

(44) Xie, L.; Jiao, L.; and Dai, H. Selective etching of graphene edges by hydrogen plasma. *J. Am. Chem. Soc.* **2010**, *132*, 14751-14753.

(45) Novoselov, K. S.; Jiang, Z.; Zhang, Y.; Morozov, S. V.; Stormer, H. L.; Zeitler, U.; Maan, J. C.; Boebinger, G. S.; Kim, P.; Geim, A. K. Room temperature quantum hall effect in graphene. *Science* **2007**, *315*, 1379.

(46) Zhang, H.; Peng, C.; Yang, J.; Lv, M.; Liu, R.; He, D.; Fan, C.; Huang, Q. Uniform ultrasmall graphene oxide nanosheets with low cytotoxicity and high cellular uptake. *ACS Appl. Mater. interfaces* **2013**, *5*, 1761-1767.

(47) Hamilton, I. P.; Li, B.; Yan, X.; Li, L. S. Alignment of colloidal graphene quantum dots on polar surfaces. *Nano lett.* **2011**, *11*, 1524-1529.

(48) Li, Y.; Zhao, Y.; Cheng, H.; Hu, Y.; Shi, G.; Dai, L.; Qu, L. Nitrogen-doped graphene quantum dots with oxygen-rich functional groups. *J. Am. Chem. Soc*. **2012**, *134*, 15-18.

(49) Pan, D.; Zhang, J.; Li, Z.; Wu, M. Hydrothermal route for cutting graphene sheets into blue-luminescent graphene quantum dots. *Adv. mater.* **2010**, *22*, 734-738.

(50) Wang, F.; Zhang, Y. B.; Tian, C. S.; Girit, C.; Zettl, A.; Crommie, M.; Shen, Y. R. Gate-variable optical transitions in graphene. *Science* **2008**, *320*, 206.

(51) Lui, C. H.; Mak, K. F.; Shan, J.; Heinz, T. F. Ultrafast photoluminescence from graphene. *Phys. Rev. Lett*. **2010**, *105*, 127404.

(52) Swathi, R. S.; Sebastian, K. L. Resonance energy transfer from a dye molecule to graphene. *J. Chem. Phys.* **2008**, *129*, 054703.

(53) Fan, F. R. F.; Park, S.; Zhu, Y.; Ruoff, R.S.; Bard, A.J. Electrogenerated chemiluminescence of partially oxidized highly oriented pyrolytic graphite surfaces and of graphene oxide nanoparticles. *J. Am. Chem. Soc.* **2009**, *131*, 937.

(54) Peng, J.; Gao, W.; Gupta, B. K.; Liu, Z.; Romero-Aburto, R.; Ge, L.; Song, L.; Alemany, L.B.; Zhan, X.; Gao, G.; Vithayathil, S.A. Graphene quantum dots derived from carbon fibers. *Nano Lett*. **2012**, *12*, 844.

(55) Kumar, A.; Zhou, W. The race to replace tin-dopped indium oxide: which metal will win? *ACS Nano* **2010**, *4*, 11-14.

(56) Becerril, H.A.; Mao, J.; Liu, Z.; Stoltenberg, R.M.; Bao, Z.; Chen, Y. Evaluation of solution-processed reduced graphene oxide films as transparent conductors. *ACS Nano* **2008**, *2*, 463-470.

(57) Zhao, J.; Pei, S.; Ren, W.; Gao, L.; Cheng, H.M. Efficient preparation of large-area graphene oxide sheets for transparent conductive films. *ACS Nano* **2010**, *4*, 5245-5252.

(58) Li, X.; Magnuson, C.W.; Venugopal, A.; An, J.; Suk, J. W.; Han, B.; Borysiak, M.; Cai, W.; Velamakanni, A.; Zhu, Y.; Fu, L. Graphene films with large domain size by a two-step chemical vapor deposition process. *Nano Lett.* **2010**, *10*, 4328-4334.

(59) Mueller, T.; Xia, F.; Avouris, P. Graphene photodetectors for high-speed optical communications. *Nat. Photonics* **2010**, *4*, 297-301.

(60) Sun, D.; Divin, C.; Rioux, J.; Sipe, J. E., Berger, C.; De Heer, W.A.; First, P.N.; Norris, T.B.; Coherent control of ballistic photocurrents in multilayer epitaxial graphene using quantum interference. *Nano Lett.* **2010**, *10*, 1293-1296.

(61) Wang, X.; Zhi, L.; Müllen, K. Transparent, conductive graphene electrodes for dye-sensitized solar cells. *Nano Lett.* **2008**, *8*, 323-327.

(62) Kamat, P.V. Graphene-based nanoassemblies for energy conversion. *J. Phys. Chem. Lett.* **2011**, *2*, 242-251.

(63) Chang, H.; Liu, Y.; Zhang, H.; Li, J. Pyrenebutyrate-functionalized graphene/poly (3-octyl-thiophene) nanocomposites based photoelectrochemical cell. *J. Electroanal. Chem.* **2011**, *656*, 269-273.

(64) Liu, Z.; Liu, Q.; Huang, Y.; Ma, Y.; Yin, S.; Zhang, X.; Sun, W.; Chen, Y. Organic photovoltaic devices based on a novel acceptor material: graphene. *Adv. Mater.* **2008**, *20*, 3924-3930.

(65) Gomez De Arco, L.; Zhang, Y.; Schlenker, C.W.; Ryu, K.; Thompson, M.E.; Zhou, C. Continuous, highly flexible, and transparent graphene films by chemical vapor deposition for organic photovoltaics. *ACS Nano* **2010**, *4*, 2865-2873.

(66) Yin, Z.; Wu, S.; Zhou, X.; Huang, X.; Zhang, Q.; Boey, F.; Zhang, H.; Electrochemical deposition of ZnO nanorods on transparent reduced graphene oxide electrodes for hybrid solar cells. *Small* **2010**, *6*, 307-312.

(67) Yang, N.; Zhai, J.; Wang, D.; Chen, Y.; Jiang, L. Two-dimensional graphene bridges enhanced photoinduced charge transport in dye-sensitized solar cells. A*CS Nano* **2010**, *4*, 887-894.

(68) Tang, Y. B.; Yin, L. C.; Yang, Y.; Bo, X. H.; Cao, Y. L.; Wang, H.E.; Zhang, W. J.; Bello, I.; Lee, S. T.; Cheng, H. M.; Lee, C. S. Tunable band gaps and p-type transport properties of boron-doped graphene by controllable ion doping using reactive microwave plasma. *ACS Nano* **2012**, *6*, 1970-1978.

(69) Hong, W.; Xu, Y.; Lu, G.; Li, C.; Shi, G. Transparent graphene/PEDOT–PSS composite films as counter electrodes of dye-sensitized solar cells. *Electrochem. Commun*. **2008**, *10*, 1555-1558.

(70) Bao, Q.; Zhang, H.; Wang, Y.; Ni, Z.; Yan, Y.; Shen, Z. X.; Loh, K.P.; Tang, D.Y. Atomic-layer graphene as a saturable absorber for ultrafast pulsed lasers. *Adv. Funct. Mater.* **2009**, *19*, 3077-3083.

(71) Hasan, T.; Torrisi, F.; Sun, Z.; Popa, D.; Nicolosi, V.; Privitera, G.; Bonaccorso, F.; Ferrari, A.C. Solution-phase exfoliation of graphite for ultrafast photonics. *Physica Status Solidi* **2010**, *247*, 2953-2957.

(72) Xiang, Q.; Yu, J.; Jaroniec, M. Graphene-based semiconductor photocatalysts. *Chem. Soc. Rev.* **2012**, *41*, 782-796.

(73) An, X. Q.; Yu, J. C. Graphene-based photocatalytic composites. *RSC Adv*. **2011**, *1*, 1426-1434.

(74) Zhang, H.; Lv, X.; Li, Y.; Wang, Y.; Li, J. P25-graphene composite as a high performance photocatalyst. *ACS Nano* **2010**, *4*, 380-386.

(75) Zhang, Y.; Tang, Z. R.; Fu, X.; Xu, Y. J. TiO_2− graphene nanocomposites for gas- phase photocatalytic degradation of volatile aromatic pollutant: is TiO_2−graphene truly different from other TiO_2− carbon composite materials? *ACS nano* **2010**, *4*, 7303-7314.

(77) Yeh, T.F.; Syu, J.M.; Cheng, C.; Chang, T.H.; Teng, H. Graphite oxide as a photocatalyst for hydrogen production from water. *Adv. Funct. Mater*. **2010**, *20*, 2255-2262.

(78) Zhang, X.Y.; Li, H. P.; Cui, X. L.; Lin, Y. Graphene/TiO_2 nanocomposites: synthesis, characterization, and application in hydrogen evolution from water photocatalytic splitting. *J. Mater. Chem*. **2010**, *20*, 2801-2806.

(79) Li, Q.; Guo, B.; Yu, J.; Ran, J.; Zhang, B.; Yan, H.; Gong, J.R. Highly efficient visible-light-driven photocatalytic hydrogen production of CdS-cluster-decorated graphene nanosheets. *J. Am. Chem. Soc.* **2011**, *133*, 10878-10884.

(80) Lv, X. J.; Fu, W. F.; Chang, H. X.; Zhang, H.; Cheng, J. S.; Zhang, G. J.; Song, Y.; Hu, C.Y.; Li, J. H. Hydrogen evolution from water using semiconductor nanoparticle/graphene composite photocatalysts without noble metals. *J. Mater. Chem*. **2012**, *22*, 1539-1546.

(81) Lv, X. J.: Zhou, S. X.; Zhang, C.; Chang, H. X.; Chen, Y.; Fu, W. F. Synergetic effect of Cu and graphene as cocatalyst on TiO_2 for enhanced photocatalytic hydrogen evolution from solar water splitting. *J. Mater. Chem*. **2012**, *22*, 18542-18549.

(82) Chang, H.; Lv, X.; Zheng, Z.; Wu, H. Bioinspired solar water splitting, sensitized solar cells, and ultraviolet sensor based on semiconductor nanocrystal antenna/graphene nanoassemblies. *Proc. SPIE* **2011**, *8333*, 109-114.

(83) Zhang, J.; Yu, J.; Jaroniec, M.; Gong, J.R. Noble metal-free reduced graphene oxide-Zn_x $Cd_{1-x}S$ nanocomposite with enhanced solar photocatalytic H_2-production performance. *Nano Lett.* **2012**, *12*, 4584-4589.

(84) Ng, Y.H.; Iwase, A.; Kudo, A.; Amal, R. Reducing graphene oxide on a visible-light $BiVO_4$ photocatalyst for an enhanced photoelectrochemical water splitting. *J. Phys. Chem. Lett*. **2010**, *1*, 2607-2612.

(85) Yang, C.; Wu, Y.; Ma, Q.; Zhang, W. H. Nanocrystals of halide perovskites: Synthesis, properties, and applications. *J. Energ. Chem*. **2018**, *3*, 622-636.

(86) Mu, Y.; He, Z.; Wang, K.; Pi, X.; Zhou, S. Recent progress and future prospect on halide perovskites nanocrystals for optoelectronics and beyond. *iScience*, **2022**, *25*, 105371.

(87) Protesescu, L.; Yakunin, S.; Bodnarchuk, M. I.; Krieg, F.; Caputo, R.; Hendon, C. H.; Yang, R. X.; Walsh, A.; Kovalenko, M. V. Nanocrystals of cesium lead halide perovskites ($CsPbX_3$, X= Cl, Br, and I): novel optoelectronic materials showing bright emission with wide color gamut. *Nano Lett.* **2015**, *15*, 3692-3696

(88) Li, X.; Wu, Y.; Zhang, S.; Cai, B.; Gu, Y.; Song, J.; Zeng, H. $CsPbX_3$ quantum dots for lighting and displays room-temperature synthesis, photoluminescence superiorities, underlying origins, and white light-emitting diodes. *Adv. Funct. Mater*. **2016**, *26*, 2435-2445.

(89) Swarnkar, A.; Chulliyil, R.; Ravi, V. K.; Irfanullah, M.; Chowdhury, A.; Nag, A. Colloidal $CsPbBr_3$ perovskite nanocrystals: luminescence beyond traditional quantum dots. *Angew. Chem., Int. Ed.* **2015**, *54*, 15424-15428

(90) Ramasamy, P.; Lim, D. H.; Kim, B.; Lee, S. H.; Lee, M. S.; Lee, J. S. All-inorganic cesium lead halide perovskite nanocrystals for photodetector applications. *Chem. Commun*. **2016**, *52*, 2067-2070.

(91) Nedelcu, G.; Protesescu, L.; Yakunin, S.; Bodnarchuk, M. I.; Grotevent, M. J.; Kovalenko, M.V. Fast anion-exchange in highly luminescent nanocrystals of cesium lead halide perovskites ($CsPbX_3$, X= Cl, Br, I). *Nano Lett*. **2015**, *15*, 5635-5640

(92) Akkerman, Q.A.; D'Innocenzo, V.; Accornero, S.; Scarpellini, A.; Petrozza, A.; Prato, M.; Manna, L. Tuning the optical properties of cesium lead halide perovskite nanocrystals by anion exchange reactions. *J. Am. Chem. Soc*. **2015**, *137*, 10276-10281.

(93) Lin, J.; Gomez, L.; de Weerd, C.; Fujiwara, Y.; Gregorkiewicz, T.; Suenaga, K.; Direct observation of band structure modifications in nanocrystals of $CsPbBr_3$ perovskite. *Nano Lett*. **2016**, *16*, 7198-7202.

(94) Peedikakkandy, L.; Bhargava, P.; Composition dependent optical, structural and photoluminescence characteristics of cesium tin halide perovskites. *RSC Adv*. **2016**, *6*, 19857-19860.

(95) Xu, Y.; Chen, Q.; Zhang, C.; Wang, R.; Wu, H.; Zhang, X.; Xing, G.; Yu, W.W.; Wang, X.; Zhang, Y.; Xiao, M. Two-photon-pumped perovskite semiconductor nanocrystal lasers. *J. Am. Chem. Soc*. **2016**, *138*, 3761-3768.

(96) Wang, Y.; Li, X.; Zhao, X.; Xiao, L.; Zeng, H.; Sun, H.; Nonlinear absorption and low-threshold multiphoton pumped stimulated emission from all-inorganic perovskite nanocrystals. *Nano Lett.* **2016**, *16*, 448-453.

(97) Zhang, J.; Shum, P.P.; & Su, L. A review of geometry-confined perovskite morphologies: From synthesis to efficient optoelectronic applications. *Nano Res.* **2022**, *15*, 7402–7431.

(98) Wang, Y. P.; Li, H. C.; Huang, Y. C.; Tan, C. S. Synthesis, and applications of halide perovskite nanocrystals in optoelectronics. *Inorganics* **2023**, *11*, 39.

(99) Iftikhar, F. A.; Wali, Q.; yang, S.; Iqbal, Y.; Jose, R.; Muknir, S.; Gondal, S. A.; Khan, M. A. Structural and optoelectronic properties of hybrid halide perovskites for solar cells, *Org. Electron*. **2021**, *91*, 106077.

(100) Cun, W.; Jincai, Z.; Xinming, W.; Bixian, M.; Guoying, S.; Ping'an, P.; Jiamo, F. Preparation, characterization and photocatalytic activity of nano-sized ZnO/SnO_2 Coupled Photocatalysts. *Appl. Catal. B Environ.* **2002**, *39*, 269–279.

(101) Liu, M.; Li, F.; Sun, Z.; Ma, L.; Xu, L.; Wang, Y. Noble-metal-free Photocatalysts MoS_2–Graphene/CdS Mixed nanoparticles/nanorods Morphology with High Visible Light Efficiency for H_2 Evolution. *Chem. Commun.* **2014**, *50*, 11004–11007.

(102) Su, T.; Shao, Q.; Qin, Z.; Guo, Z.; Wu, Z. Role of Interfaces in two-dimensional photocatalyst for water splitting. *ACS Catal*. **2018**, *8*, 2253–2276.

(103) Kumar, S.; Kumar, A.; Kumar, A.; Krishnan, V. Nanoscale zinc oxide based heterojunctions as visible light active photocatalysts for hydrogen energy and environmental remediation. *Catal. Rev. - Sci. Eng*. **2020**, *62*, 346–405.

(104) Mei, A.; Li, X.; Liu, L.; Ku, Z.; Liu, T.; Rong, Y.; Xu, M.; Hu, M.; Chen, J.; Yang, Y.; Grätzel, M. A hole-conductor–free, fully printable mesoscopic perovskite solar cell with high stability. *science* **2014**, *345*, 295-298..

(105) Minemoto, T.; Murata, M. Impact of work function of back contact of perovskite solar cells without hole transport material analyzed by device simulation. *Curr. Appl. Phys*. **2014**, *14*, 1428–1433.

(106) Bogachuk, D.; Zouhair, S.; Wojciechowski, K.; Yang, B.; Babu, V.; Wagner, L.; Xu, B.; Lim, J.; Mastroianni, S.; Pettersson, H.; Hagfeldt, A. Low-temperature carbon-based electrodes in perovskite solar cells. *Energy Environ. Sci.* **2020**, *13*, 3880–3916.

(107) Don, Fathiah, M.; Ekanayake, P.; Jennings, J. R.; Nakajima, H.; and Lim. C. M. Graphite/carbon black counter electrode deposition methods to improve the efficiency and stability of hole-transport-layer-free perovskite solar cells." *ACS omega* **2022**, 7, 22830-22838.

(108) Nguyen, P.D.; Duong, T. M.; Tran, P.D. Current progress and challenges in engineering viable artificial leaf for solar water splitting. *J. Sci. Adv. Mater. Devices* **2017**, *2*, 399–417.

(109) Ye, S.; Shi, W.; Liu, Y.; Li, D.; Yin, H.; Chi, H.; Luo, Y.; Ta, N.; Fan, F.; Wang, X.; Li, C. Unassisted photoelectrochemical cell with multimediator modulation for solar water splitting exceeding 4% solar-to-hydrogen efficiency. *J. Am. Chem. Soc*. **2021**, *143*, 12499–12508.

(110) Chen, Z.; Dinh, H.N.; Miller, E.; Photoelectrochemical water splitting. *Springer*, New York, **2013**, *344*, 6-15.

(111) Minggu, L. J.; Daud, W. R. W.; Kassim, M. B. An overview of photocells and photoreactors for photoelectrochemical water splitting. *Int. J. Hydrog. Energy* **2010**, *35*, 5233-5244.

(112) Guo, Y.; Li, G.; Zhou, J.; Liu, Y. Comparison between hydrogen production by alkaline water electrolysis and hydrogen production by PEM electrolysis. *IOP Publishing., IOP Conf. Ser. Earth Environ. Sci*. **2019**, *371*, 042022.

(113) Kamat, P. V.; Pradhan, N.; Schanze, K.; Weiss, P.S.; Buriak, J. Challenges and opportunities in designing perovskite nanocrystal heterostructures *ACS Energy Lett*. **2020**, *2*, 2253–2255.

(114) Bera, S.; and Pradhan, N. Perovskite Nanocrystal heterostructures: synthesis, optical properties, and applications. *ACS Energy Lett.* **2020,** *5*, 2858–2872.

(115) Dutta, S,; Mehetor S. K.; and Pradhan, N. Metal semiconductor heterostructures for photocatalytic conversion of light energy, *J. Phys. Chem. Lett.* **2015**, *6*, 936–944.

(116) Gu, Z.; Chen, F.; Zhang, X.; Liu, Y.; Fan, C.; Wu, G.; Li, H.; Chen, H. Novel planar heterostructure perovskite solar cells with CdS nanorods array as electron transport layer. *Sol. Energy Mater. Sol. Cells* **2015**, *140*, 396–404.

(117) Gomez, C. M.; Pan, S.; Braga, H. M.; Oliveira, L. S. de; Dalpian, G. M.; Biesold-McGee, G. V.; Lin, Z.; Santos, S. F.; Souza, J. A. Possible charge-transfer-induced conductivity enhancement in TiO_2 microtubes decorated with perovskite $CsPbBr_3$ nanocrystals. *Langmuir* **2020**, *36*, 5408–5416.

(119) Soltani, R.; Puscher, B. M. D.; Katbab, A. A.; Levchuk, I., Kazerouni, N.; Gasparini, N,; Camaioni, N.; Osvet, A.; Batentschuk, M. Improved charge carrier dynamics in polymer/perovskite nanocrystal based hybrid ternary solar cells. *Phys. Chem. Chem. Phys.* **2018**, *20*, 23674–23683.

(120) Wu, K.; Liang, G.; Shang, Q.; Ren, Y.; Kong, D.; Lian, T. Ultrafast interfacial electron and hole transfer from $CsPbBr_3$ perovskites quantum dots. *J. Am.Chem. Soc*. **2015**, *137*, 12792–12795.

(121) Zhu, R.; Gao, C.; Sun, T.; Shen, L.; Sun, D.; Li, X.; Surface decoration of $CH_3NH_3PbBr_3$ nanoparticles with the chemically pbsorbed Perylenetetracarboxylic diimde. *Langmuir* **2016**, *32*, 3294–3299

(122) Nair, V. C.; Muthu, C.; Rogach, A. L.; Kohara, R.; Biju, V. Channeling exciton migration into electron transfer in formamidinium lead bromide perovskite nanocrystal/fullerene composites. *Angew. Chem. Int. Ed.* **2016**, *56*, 1214–1218.

(123) Fang, Q.; Shang, Q.; Zhao, L.; Wang, R.; Zhang, Z.; Yang, P.; Sui, X.; Qiu, X.; Liu, X.; Zhang, Q.; et al. Ultrafast charge transfer in perovskite nanowire/2D transition metal dichalcogenide heterostructures. *J. Phys. Chem. Lett*. **2018**, *9*, 1655–1662.

(124) Muduli, S.; Pandey, P.; Devatha, G.; Babar, R.; M, T.; Kothari, D. C.; Kabir, M.; Pillai, P. P.; Ogale, S. Photoluminescence quenching in self-assembled $CsPbBr_3$ quantum dots on few-layer black phosphorus sheets. *Angew. Chem.* **2018**, *130*, 7808−7812.

(125) Pan, A.; Ma, X.; Huang, S.; Wu, Y.; Jia, M.; Wangyang, P.; Liu, Y.; Shi, Y.; He, L.; Liu, Y. $CsPbBr_3$ Perovskite nanocrystal grown on mxene nanosheets for enhanced photoelectric detection and photocatalytic CO_2 reduction. *J. Phys. Chem. Lett.* **2019**, *10*, 6590−6597.

(126) Ou, M.; Tu, W.; Yin, S.; Xing, W.; Wu, S.; Wang, H.; Wan, S.; Zhong, Q.; Xu, R. Amino-assisted anchoring of $CsPbBr_3$ perovskite quantum dots on porous g-C_3N_4 for enhanced photocatalytic CO_2 reduction. *Angew. Chem.* **2018**, *130*, 13758−13762.

(127) Ravi, V. K.; Saikia, S.; Yadav, S.; Nawale, V. V.; Nag, A. $CsPbBr_3$/ZnS core/shell type nanocrystals for enhancing luminescence lifetime and water stability. *ACS Energy Lett.* **2020**, *5*, 1794−1796.

(128) Liu, X.; Zhang, X.; Li, L.; Xu, J.; Yu, S.; Gong, X.; Zhang, J.; Yin, H. Stable luminescence of $CsPbBr_3$/nCdS core/shell perovskitquantum dots with all self-passivation layer modification. *ACS appl. Mater. Interfaces* **2019**, *11*, 40923−40931.

(129) Brumberg, A.; Diroll, B. T.; Nedelcu, G.; Sykes, M. E.; Liu, Y.; Harvey, S. M.; Wasielewski, M. R.; Kovalenko, M. V.; Schaller, R. D. Material dimensionality effects on electron transfer rates between $CsPbBr_3$ and CdSe nanoparticles. *Nano Lett.* **2018**, *18*, 4771−4776.

(130) Wang, S.; Bi, C.; Portniagin, A.; Yuan, J.; Ning, J.; Xiao, X.; Zhang, X.; Li, Y. Y.; Kershaw, S. V.; Tian, J.; Rogach, A. L. $CsPbI_3$/PbSe heterostructured nanocrystals for high-efficiency solar cells. *ACS Energy Lett*. **2020**, *5*, 2401−2410.

(131) Rathore, E.; Maji, K.; Rao, D.; Saha, B.; Biswas, K. Charge transfer in the heterostructure of $CsPbBr_3$ nanocrystals with nitrogen-doped carbon dots. *J. Phys. Chem. Lett.* **2020**, *11*, 8002-8007.

(132) Worsley, M. A.; Pauzauskie, P. J.; Olson, T. Y.; Biener, J.; Satcher, J. H.; Baumann, T. F. Synthesis of graphene aerogel with high electrical conductivity. *J. Am. Chem. Soc*. **2010**, *132*, 14067−14069.

(133) Li, X.; Zhu, Y.; Cai, W.; Borysiak, M.; Han, B.; Chen, D.; Piner, R. D.; Colombo, L.; Ruoff, R. S. Transfer of large-area graphene films for high-performance transparent conductive electrodes. *Nano Lett.* **2009**, *9*, 4359−4363.

(134) Kim, K. S.; Zhao, Y.; Jang, H.; Lee, S. Y.; Kim, J. M.; Kim, K. S.; Ahn, J.-H.; Kim, P.; Choi, J.-Y.; Hong, B. H. Large-scale pattern growth of graphene films for stretchable transparent electrodes. *Nature* **2009**, *457*, 706−710.

(135) Novoselov, K. S.; Fal'ko, V. I.; Colombo, L.; Gellert, P. R.; Schwab, M. G.; Kim, K. A Roadmap for Graphene. *Nature* **2012**, *490*, 192−200.

(136) Craciun, M. F.; Khrapach, I.; Barnes, M. D.; Russo, S. J. Properties and applications of chemically functionalized graphene. *J. Phys.: Condens. Matter*. **2013**, *25*, 423201.

(137) Nguyen, P.; Berry, V. Graphene interfaced with biological cells: opportunities and challenges. *J. Phys. Chem. Lett*. **2012**, *3*, 1024−1029.

(138) Yin, Z.; Zhu, J.; He, Q.; Cao, X.; Tan, C.; Chen, H.; Yan, Q.; Zhang, H. Graphene-based materials for solar cell applications. *Adv. Energy Mater*. **2014**, *4*, 1300574.

(139) Wu, Z.; Bai, S.; Xiang, J.; Yuan, Z.; Yang, Y.; Cui, W.; Gao, X.; Liu, Z.; Jin, Y.; Sun, B. efficient planar heterojunction perovskite solar cells employing graphene oxide as hole conductor. *Nanoscale* **2014**, *6*, 10505–10510.

(140) Zhang, Q.; Zhou, Y.; Wei, Y.; Tai, M.; Nan, H.; Gu, Y.; Han, J.; Yin, X.; Li, J.; Lin, H. Improved phase stability of γ-$CsPbI_3$ perovskite nanocrystals by interface effect using iodine modified graphene oxide. *J. Mater. Chem. C* **2020**, *8*, 2569-2578.

(141) Park, Y.; Jana, A.; Myung, C. W.; Yoon, T.; Lee, G.; Kocher, C. C.; Ying, G.; Osokin, V.; Taylor, R. A.; Kim, K. S. Enhanced photoluminescence quantum yield of $MAPbBr_3$ nanocrystals by passivation using graphene. *Nano Res*. **2020**, *13*, 932–938.

(142) Pu, Y.; Liu, W.; Liu, Y.; Jiang, Q.; Li, Y.; Zhao, Z.; Yuan, G.; Zhang, Y. Enhancing effects of reduced graphene oxide on photoluminescence of $CsPbBr_3$ perovskite quantum dots. *J. Mater. Chem. C* **2020**, *8*, 7447–7453.

(143) Tang, X.; Zu, Z.; Zang, Z.; Hu, Z.; Hu, W.; Yao, Z.; Chen, W.; Li, S.; Han, S.; Zhou, M. $CsPbBr_3$/reduced graphene oxide nanocomposites and their enhanced photoelectric detection application.sens. *Actuators, B* **2017**, *245*, 435−440.

(144) Xu, Y.; Yang, M.; Chen, B.; Wang, X.; Chen, H.; Kuang, D.; Su, C. A $CsPbBr_3$ perovskite quantum dot/graphene oxide composite for photocatalytic CO_2 reduction. *J. Am. Chem. Soc.* **2017**, *139*, 5660−5663.

(145) Mishra, L.; Panigrahi, A.; Dubey, P.; Sarangi. M. K. Photo-induced charge transfer in composition-tuned halide perovskite nanocrystals with quinone and its impact on conduction current. *J. Appl. Phys.* **2022**, *132*, 195702.

(146) Biswas, S.; Akhil, S.; Kumar, N.; Palabathuni, M.; Singh, R.; Vasavi Dutt, V. J.; Mishra. N. Exploring the role of short chain acids as surface ligands in photoinduced charge transfer dynamics from $CsPbBr_3$ erovskite nanocrystals. *J. Phys. Chem. Lett.* **2023**, *14*, 1910-1917.

(147) Cohen, T. A.; Huang, Y.; Bricker, N. A.; Juhl, C. S.; Milstein, T. J.; MacKenzie, J. D.; Luscombe, C. K.; Gamelin, D. R. Modular zwitterion-functionalized poly(isopropyl methacrylate) polymers for hosting luminescent lead halide perovskite nanocrystals. *Chem. Mater.* **2021**, *33*, 3779– 3790.

(148) Jeffrey, T.; Bose, D.; Kamat. P. V. How pendant groups dictate energy and electron transfer in perovskite–rhodamine light harvesting assemblies. *J. Am. Chem. Soc.* **2023**, *145*, 4601-4612.

(149) Alam, S.; Sharma, N.; Graphene, L. K. Synthesis of graphene oxide (GO) by modified hummers method and its thermal reduction to obtain reduced graphene oxide (rGO). *Graphene* **2017**, *6*, 1-18.

(150) Park, S.; An, J.; Potts, J. R.; Velamakanni, A.; Murali, S.; Ruoff, R. S. Hydrazine-reduction of graphite- and graphene oxide. *Carbon* **2011**, *49*, 3019–3023.

(151) Mallakpour, S.; Abdolmaleki, A. Covalently functionalized graphene sheets with biocompatible natural amino acids. *Appl. Surf. Sci.* 2**014**, *307*, 533-542.

(152) Di Stasio, F.; Ramiro, I.; Bi, Y.; Christodoulou, S.; Stavrinadis, A.; Konstantatos, G. High-efficiency light-emitting diodes based on formamidinium lead bromide nanocrystals and solution processed transport layers. *Chem. Mater.* **2018**, *30*, 6231–6235.

(153) Zhu, Y.; Jia, S.; Zheng, J.; Lin, Y. Facile synthesis of nitrogen-doped graphene frameworks for enhanced performance of hole transport material-free perovskite solar cells. *J. Mater. Chem. C* **2018**, *6*, 3097-3103.

(154) Sharma, V.; Jain, Y.; Kumari, M.; Gupta, R.; Sharma, S. K.; Sachdev, K. Synthesis and characterization of graphene oxide (GO) and reduced graphene oxide (RGO) for gas sensing application. *Macromol. Symp.* **2017**, *376*, 1700006.

(155) Chen, G.-L.; Shau, S.-M.; Juang, T.-Y.; Lee, R.-H.; Chen, C.-P.; Suen, S.-Y.; Jeng, R.-J. Single-layered graphene oxide nanosheet/polyaniline hybrids fabricated through direct molecular exfoliation. *Langmuir* **2011**, *27*, 14563-14569.

(156) Lai, L.; Chen, L.; Zhan, D.; Sun, L.; Liu, J.; Lim, S. One-step synthesis of nh_2-graphene from in situ graphene-oxide reduction and its improved electrochemical properties. *Carbon* **2011**, *49*, 3250-3257.

(157) Ravi, V.; Markad, G. Band edge energies and excitonic transition probabilities of colloidal $CsPbX_3$ (X = Cl, Br, I) perovskite nanocrystals. *ACS Energy Lett.* **2016**, *1*, 665-671.

(158) Ullah, R.; Khan, S. A.; Aladresi, A. A. M.; Alharbi, S. A.; Chinnathambi, A. Ovalbumin-mediated synthesis and simultaneous functionalization of graphene with increased protein stability. Green *Chem. Lett. Rev.* **2020**, *13*, *60–67.*

(159) Chandraker, K.; Nagwanshi, R. Antibacterial properties of amino acid functionalized silver nanoparticles decorated on graphene oxide sheets. Spectrochim. *Acta Part A Mol. Biomol. Spectrosc.* **2017**, *181*, 47–54.

(160) Mallineni, S. S. K.; Shannahan, J.; Raghavendra, A. J.; Rao, A. M.; Brown, J. M.; Podila, R. Biomolecular interactions and biological responses of emerging two-dimensional materials and aromatic amino acid complexes. *ACS Appl. Mater. Interfaces* **2016**, *8*, 16604–16611.

(161) Li, M.; Zhang, X.; Dong, T.; Wang, P.; Matras-Postolek, K.; Yang, P. Evolution of morphology, phase composition, and photoluminescence of cesium lead bromine nanocrystals with temperature and precursors. *J. Phys. Chem. C* **2018**, *122*, 28968–28976.

(162) Sun, S.; D, Yuan,; Xu, Y. Wang, Denf, Z. Ligand-mediated synthesis of shape-controlled cesium lead halide perovskite nanocrystals via reprecipitation process at room temperature. *ACS Nano*. **2016**, *10*, 3648–3657.

(163) Yang, L.; Wang, T.; Min, Q.; Liu, B.; Liu, Z.; Fan, X.; Qiu, J.; Xu, X.; Yu, J.; Yu, X. High water resistance of monoclinic $CsPbBr_3$ nanocrystals derived from zero-dimensional cesium lead halide perovskites. *acs omega* 2**019**, *4*, 6084–6091.

(164) Xu, Z.; Chen, T.; Zhang, D.; Zheng, G.; Wu, J.; Yan, J.; Liu, X.; Qiu, J. Linear and nonlinear optical characteristics of $CsPbBr_3$ perovskite quantum dots-doped borosilicate glasses. *J. Eur. Ceram. Soc.* **2021**, *41*, 729–734.

(165) Javed, H.; Fatima, K.; Akhter, Z.; Nadeem, M. A.; Siddiq, M.; Iqbal, A. Fluorescence modulation of cadmium sulfide quantum dots by azobenzene photochromic switches. *Proc. R. Soc. A* **2015**, *472*, 2186.

(166) Kumar, A.; Dutta, R. K. CdS quantum dots immobilized on calcium alginate microbeads for rapid and selective detection of Hg^{2+} ions. *RSC Adv.* **2015**, *5*, 76275–76284.

(167) Yuan, B.; Li, N.; Liu, J.; Xu, F.; Li, C.; Juan, F.; Yu, H.; Li, C.; Cao, B. Improving the performances of $CsPbBr_3$ solar cells fabricated in ambient condition. *J. Mater. Sci. Mater. Electron.* **2020**, *31*, 21154–21167.

(168) Woo, J. Y.; Kim, Y.; Bae, J.; Kim, T. G.; Kim, J. W.; Lee, D. C.; Jeong, S. Highly stable cesium lead halide perovskite nanocrystals through in situ lead halide inorganic passivation. *Chem. Mater.* **2017**, *29*, 7088–7092.

(169) Mi, L.; Chang, Y.; Zhang, Y.; Xu, E.; Chemistry, Y. J. Hybrid perovskite exchange of PbS quantum dots for fast and high-detectivity visible–near-infrared photodetectors. *J. Mater. Chem. C* **2020**, *8*, 7812–7819.

(170) Tchaplyguine, M,; Mikkela, M. H.; Marsell, E,; Polley, C,; Mikkelsen, A,; Zhang, W,; Yartsev, A,; Hetherington, J. H,; Wallenberg, L. R,; Bjorneholm, O. Thioacetamide-ligand-mediated synthesis of $CsPbBr_3$–$CsPbBr_3$ homostructured nanocrystals with enhanced stability. *Phys. Chem. Chem. Phys*. **2017**, *19*, 7252–7261.

(171) Yu, H.; Xiao, P.; Tian, J.; Wang, F.; Yu, J. Phenylamine-functionalized RGO/TiO_2 photocatalysts: Spatially separated adsorption sites and tunable photocatalytic selectivity. *ACS Appl. Mater. Interfaces* **2016**, *8*, 29470–29477.

(172) Raevskaya, A. E,; Stroyuk, O. L,; Panasiuk, L. V,; Dzhagan, V. M,; Solonenko, D.I,; Schulze, S.; Zahn. D. R. T. A new route to very stable water-soluble ultra-small core/shell CdSe/CdS quantum dots. *Nano-Structures and Nano-Objects* **2018**, *13*, 146–154.

(173) Levchuk, I.; Osvet, A.; Tang, X.; Brandl, M.; Perea, J. D.; Hoegl, F.; Matt, G. J.; Hock, R.; Batentschuk, M.; Brabec, C. J. Brightly luminescent and color-tunable formamidinium lead halide perovskite $FAPbX_3$ (X = Cl, Br, I) colloidal nanocrystals. *Nano Lett.* **2017**, *17*, 2765–2770.

(174) Zhu, N.; Zheng, K.; Karki, K. J.; Abdellah, M.; Zhu, Q.; Carlson, S.; Haase, D.; Žídek, K.; Ulstrup, J.; Canton, S. E.; et al. Sandwiched confinement of quantum dots in graphene matrix for efficient electron transfer and photocurrent production. *Sci. Rep.* **2015**, *5*, 9860.

(175) Muduli, S.; Pandey, P.; Devatha, G.; Babar, R.; Kothari, D. C.; Kabir, M.; Pillai, P. P.; Ogale, S.; Muduli, S.; Babar, R.; et al. Photoluminescence quenching in self-assembled $CsPbBr_3$ quantum dots on few-layer black phosphorus sheets. *Angew. Chemie* 2**018**, *130*, 7808–7812.

(176) Zhang, C.; Zhang, H.; Wang, R.; You, D.; Wang, W.; Wang, W.; Xu, C.; Dai, J. Exciton photoluminescence of $CsPbBr_3$@SiO_2 quantum dots and its application as a phosphor material in light-emitting devices. *Opt. Mater. Express* **2020**, *10*, 1007–1017.

(177) Biswas, K.; Rathore, E.; Maji, K.; Rao, D.; Saha, B. Charge transfer in the heterostructure of $CsPbBr_3$ nanocrystals with nitrogen-doped carbon dots. *J. Phys. Chem. Lett.* **2020**, *11*, 8002–8007.

(178) Dejpasand, M.; Saievar-Iranizad, E.; A. B.-M. R. Tuning HOMO and LUMO of three region (UV, Vis and IR) photoluminescent nitrogen doped graphene quantum dots for photodegradation of methylene blue. *Mater. Res. Bull.* **2020**, *128*, 110886.

(179) Yun, J.; Fan, H.; Zhang, Y.; Huang, R.; Ren, Y.; Guo, M.; An, H.; Kang, P.; Guo, H. Enhanced optical absorption and interfacial carrier separation of

$CsPbBr_3$/Graphene Heterostructure: Experimental and theoretical insights. *ACS Appl. Mater. Interfaces* **2020**, *12*, 3086–3095.

(180) Zhang, T.; Li, H.; Yang, P.; Wei, J.; Wang, F.; Shen, H.; Li, D.; Li, F. Room-temperature synthesized formamidinium lead halide perovskite quantum dots with bright luminescence and color-tunability for efficient light emitting. *Org. Electron.* **2019**, *68*, 76–84.

(181) Levchuk, I.; Osvet, A.; Tang, X.; Brandl, M.; Perea, J. D.; Hoegl, F.; Matt, G. J.; Hock, R.; Batentschuk, M.; Brabec, C. J. Brightly luminescent and color-tunable formamidinium lead halide perovskite $FAPbX_3$ (X = Cl, Br, I) colloidal nanocrystals. *Nano Lett.* **2017**, *17*, 2765–2770.

(182) Zhang, C.; Wang, S.; Li, X.; Yuan, M.; Turyanska, L.; Yang, X. Core/shell perovskite nanocrystals: synthesis of highly efficient and environmentally stable $FAPbBr_3$ /$CsPbBr_3$ for LED applications. *Adv. Funct. Mater.* **2020**, *30*, 1910582.

(183) Sharma, V.; Jain, Y.; Kumari, M.; Gupta, R.; Sharma, S. K.; Sachdev, K. Synthesis and characterization of graphene oxide (GO) and reduced graphene oxide (RGO) for gas sensing application. *Macromol. Symp.* **2017**, *376*, 1700006.

(184) Ruiz, S.; Tamayo, J. A.; Ospina, J. D.; Porras, D. P. N.; Zapata, M. E. V.; Hernandez, J. H. M.; Valencia, C. H.; Zuluaga, F.; Tovar, C. D. G. Antimicrobial films based on nanocomposites of chitosan/poly (Vinyl Alcohol)/graphene oxide for biomedical applications. *Biomolecules* **2019**, *9*, 109/1-17.

(185) Wu, J. B.; Lin, M. L.; Cong, X.; Liu, H. N.; Tan, P. H. Raman spectroscopy of graphene based materials and its applicarions in related devices. *Chem. Soc. Rev.* **2018**, *47*, 1822–1873.

(186) Chen, H.; Fan, L.; Zhang, R.; Bao, C.; Zhao, H.; Xiang, W.; Liu, W.; Niu, G.; Guo, R.; Zhang, L.; et al. High-efficiency formamidinium lead bromide perovskite nanocrystal-based light-emitting diodes fabricated via a surface defect self-passivation strategy. *Adv. Opt. Mater.* **2020**, *8*, 1901390.

(187) Di Stasio, F.; Ramiro, I.; Bi, Y.; Christodoulou, S.; Stavrinadis, A.; Konstantatos, G. High-efficiency light-emitting diodes based on formamidinium lead bromide nanocrystals and solution processed transport layers. *Chem. Mater.* **2018**, *30*, 6231–6235.

(188) Zhang, T.; Li, H.; Yang, P.; Wei, J.; Wang, F.; Shen, H.; Li, D.; Li, F. Room-temperature synthesized formamidinium lead halide perovskite quantum dots with bright luminescence and color-tunability for efficient light emitting. *Org. Electron.* **2019**, *68*, 76–84.

(189) Muduli, S.; Pandey, P.; Devatha, G.; Babar, R.; M, T.; Kothari, D. C.; Kabir, M.; Pillai, P. P.; Ogale, S. Photoluminescence quenching in self-assembled $CsPbBr_3$ quantum dots on few-layer black phosphorus sheets. *Angew. Chem. Int. Ed.* **2018**, *57*, 7682−7686.

(190) Rathore, E.; Maji, K.; Rao, D.; Saha, B.; Biswas, K. Charge transfer in the heterostructure of $CsPbBr_3$ nanocrystals with nitrogen-doped carbon dots. *J. Phys. Chem. Lett.* **2020**, *11*, 8002-8007.

(191) Liu, X.; Xu, T.; Li, Y.; Zang, Z.; Peng, X.; Wei, H.; Zha, W.; Wang, F. Enhanced X-ray photon response in solution-synthesized $CsPbBr_3$ nanoparticles wrapped by reduced graphene oxide. *Sol. Energy Mater. Sol. Cells* **2018**, *187*, 249–254.

(192) Zhang, G.; Wang, A.; Jiang, T.; Guo, J. Interaction of the irisflorentin with bovine serum albumin: A fluorescence quenching study. *J. Mol. Struct.* **2008**, *891*, 93–97.

(193) Nan, Z.; Hao, C.; Ye, X.; Feng, Y.; Sun, R. S. Interaction of graphene oxide with bovine serum albumin : A fluorescence quenching study. *Spectrochim. Acta Mol. Biomol. Spectrosc.* **2019**, *210*, 348–354.

(194) Pu, Y.; Liu, W.; Liu, Y.; Jiang, Q.; Li, Y.; Zhao, Z.; Yuan, G.; Zhang, Y. Enhancing effects of reduced graphene oxide on photoluminescence of $CsPbBr_3$ perovskite Quantum Dots. *J. Mater. Chem. C* **2020**, *8*, 7447–7453.

(195) Zheng, F.; Xu, W. L.; Jin, H. D.; Hao, X. T.; Ghiggino, K. P. Charge transfer from poly(3-hexythiophene) to graphene oxide and reduced graphene oxide, *RSC Adv.* **2015**, *5*, 89515–89520.

(196) Guo, C. X.; Yang, H. B.; Sheng, Z. M.; Lu, Z. S.; Song, Q. L.; Li, C. M. Layer graphene/quantum dots for photovoltaic devices. *Angew. Chemie - Int. Ed.* **2010**, *49*, 3014–3017.

(197) Yun, J.; Fan, H.; Zhang, Y.; Huang, R.; Ren, Y.; Guo, M.; An, H.; Kang, P.; Guo, H. Enhanced optical absorption and interfacial carrier separation of $CsPbBr_3$/graphene heterostructure: Experimental and theoretical insights. *ACS Appl. Mater. Interfaces* **2020**, *12*, 3086–3095.

(198) Ucar, N.; Yuksek, O. I.; Mervin, O,; Elif, C.; Ayşen, O. The effect of oxidation process on on graphene oxide fiber properties. *Mater. Sci.-Pol.*, **2019**, *37*, 83-89.

(199) Mallakpour, S.; Abdolmaleki, A. Covalently functionalized graphene sheets with biocompatible natural amino acids. *Appl. Surf. Sci.* **2014**, *307*, 533-542.

(200) Chen, G.-L.; Shau, S.-M.; Juang, T.-Y.; Lee, R.-H.; Chen, C.-P.; Suen, S.-Y.; Jeng, R.-J. Single-Layered Graphene Oxide Nanosheet/Polyaniline Hybrids Fabricated through Direct Molecular Exfoliation. *Langmuir.* **2011**, *27*, 14563-14569.

(201) Chandraker, K.; Nagwanshi, R. Antibacterial Properties of Amino Acid Functionalized Silver Nanoparticles Decorated on Graphene Oxide Sheets. *Spectrochim. Acta Part A Mol. Biomol. Spectrosc.* **2017**, *181*, 47–54.

(202) Mallineni, S. S. K.; Shannahan, J.; Raghavendra, A. J.; Rao, A. M.; Brown, J. M.; Podila, R. Biomolecular Interactions and Biological Responses of

Emerging Two-Dimensional Materials and Aromatic Amino Acid Complexes. *ACS Appl. Mater. Interfaces* **2016**, *8*, 16604–16611.

(203) Ullah, R.; Khan, S. A.; Aladresi, A. A. M.; Alharbi, S. A.; Chinnathambi, A. Ovalbumin-Mediated Synthesis and Simultaneous Functionalization of Graphene with Increased Protein Stability. *Green Chem. Lett. Rev.* **2020**, *13*, 60–67.

(204) Gendy,E.; Ghany, D. M.; El Sherbini, E.F.; Allam, N.K. Adenine-functionalized spongy graphene for green and high-performance supercapacitors. *Sci. Rep.* **2017**, *7*, 43104.

(205) Bansal, P.; Panwar, A.S.; Bahadur, D. Effect of reaction temperature on structural and optical properties of reduced graphene oxide. *RGO* **2014**, *950*, 002.

(206) Di Stasio, F.; Ramiro, I.; Bi, Y.; Christodoulou, S.; Stavrinadis, A.; Konstantatos, G. High-efficiency light-emitting diodes based on formamidinium lead bromide nanocrystals and solution processed transport layers. *Chem. Mater.* **2018**, *30*, 6231–6235.

(207) Zhang, T.; Li, H.; Yang, P.; Wei, J.; Wang, F.; Shen, H.; Li, D.; Li, F. Room-temperature synthesized formamidinium lead halide perovskite quantum dots with bright luminescence and color-tunability for efficient light emitting. *Org. Electron.* **2019**, *68*, 76–84.

(208) Ghosh, G.; Jana, B.; Sain, S.; Ghosh, A.; Patra, A. Influence of shape on the carrier relaxation dynamics of $CsPbBr_3$ perovskite nanocrystals. *Phys. Chem. Chem. Phys*. **2019**, *21*, 19318-19326.

(209) Yun, J.; Fan, H.; Zhang, Y.; Huang, R.; Ren, Y.; Guo, M.; An, H.; Kang, P.; Guo, H. Enhanced optical absorption and interfacial carrier separation of $CsPbBr_3$/graphene heterostructure: Experimental and theoretical insights. *ACS Appl. Mater. Interfaces* **2020**, *12*, 3086–3095.

(210) Dejpasand, M.; Saievar-Iranizad, E.; A. B.-M. R. Tuning HOMO and LUMO of Three region (UV, Vis and IR) photoluminescent nitrogen doped graphene quantum dots for photodegradation of methylene blue. *Mater. Res. Bull.* **2020**, *128*, 110886.

(211) Das, J.; Subbiah, A.S.; Mahuli, N.; Singh, R.; Sarkar, S. K. One-step solution-processed formamidinium lead tribromide formation for better reproducible planar perovskite solar cells. *Energ Technol.* **2017**, *5*,1807-1813.

(212) Subbiah, A.S.; Mahuli, N.; Agarwal, S.; van Hest, M. F.; Sarkar, S. K. Towards all-inorganic transport layers for wide-band-gap formamidinium lead bromide-based planar photovoltaics. *Energy Technol.* **2017**, *5*,1800-1806.

(213) Li, S.; Deng, C.; Tao, L.; Lu, Z.; Zhang, W.; Song, W. Crystallization control and defect passivation via a cross-linking additive for high-performance $FAPbBr_3$ perovskite solar cells. *J. Phys. Chem. C* **2021**, *125*,12551-12559.

(214) Zhang, Y.; Liang, Y.; Wang, Y.; Guo, F.; Sun, L.; Xu, D. Planar $FAPbBr_3$ solar cells with power conversion efficiency above 10%. *ACS Energy Lett.* **2018**, *3*, 1808-1814.

(215) Arora, N.; Dar, M. I.; Abdi-Jalebi, M.; Giordano, F.; Pellet, N.; Jacopin, G.; Friend, R.H.; Zakeeruddin, S.M.; Grätzel, M. Intrinsic and extrinsic stability of formamidinium lead bromide perovskite solar cells yielding high photovoltage. *Nano lett.* **2016**, *16*, 7155-7162.

(216) Arora, N.; Dar, M.I.; Hezam, M.; Tress, W.; Jacopin, G.; Moehl, T.; Gao, P.; Aldwayyan, A.S.; Deveaud, B.; Grätzel, M.; Nazeeruddin, M. K. Photovoltaic and amplified spontaneous emission studies of high-quality formamidinium lead bromide perovskite films. *Adv. Funct. Mater.* **2016**, *26*, 2846-2854.

(217) Arora, N.; Orlandi, S.; Dar, M. I.; Aghazada, S.; Jacopin, G.; Cavazzini, M.; Mosconi, E.; Gratia, P.; De Angelis, F.; Pozzi, G.; Graetzel, M. High open-circuit voltage: Fabrication of formamidinium lead bromide perovskite solar cells using fluorene–dithiophene derivatives as hole-transporting materials. *ACS Energy Lett.* **2016**, *1*, 107-112.

(218) Hu, C.; Shivarudraiah, S. B.; Sung, H. H.; Williams, I. D.; Halpert, J. E.; Yang, S. Discovery of a new intermediate enables one-step deposition of high-quality perovskite films via solvent engineering. *Solar RRL* **2021**, *5*, 2000712.

(219) Zhao, Y.; Zhu, J.; He, B.; Tang, Q. Dimensionality control of SnO_2 films for hysteresis-free, all-inorganic $CsPbBr_3$ perovskite solar cells with efficiency exceeding 10%. *ACS Appl. Mater. Interfaces* **2012** *13*, 11058-11066.

(220) Duan, J.; Zhao, Y.; Yang, X.; Wang, Y.; He, B.; Tang, Q. Lanthanide ions doped $CsPbBr_3$ halides for HTM-free 10.14%-efficiency inorganic perovskite solar cell with an ultrahigh open-circuit voltage of 1.594 V. *Adv. Energy Mater.* **2018**, *8*, 1802346.

(221) Zhu, J.; He, B.; Gong, Z.; Ding, Y.; Zhang, W.; Li, X.; Zong, Z.; Chen, H.; Tang, Q. Grain enlargement and defect passivation with melamine additives for high efficiency and stable $CsPbBr_3$ perovskite solar cells. *Chem. Sus. Chem*. **2020**, *13*, 1834-1843.

(222) Ding, J.; Zhao, Y.; Duan, J.; He, B.; Tang, Q. Alloy-controlled work function for enhanced charge extraction in all-inorganic $CsPbBr_3$ perovskite solar cells. *Chem. Sus. Chem.* **2018**, *11*, 1432-1437.

(223) Poli, I.; Baker, J.; McGettrick, J.; De Rossi, F.; Eslava, S.; Watson, T.; Cameron, P.J. Screen printed carbon $CsPbBr_3$ solar cells with high open-circuit photovoltage. *J. Mater. Chem. A* **2018**, *6*, 18677-18686.

(224) Liu, Y.; He, B.; Duan, J.; Zhao, Y.; Ding, Y.; Tang, M.; Chen, H.; Tang, Q. Poly(3-hexylthiophene)/zinc phthalocyanine composites for advanced interface engineering of 10.03%-efficiency $CsPbBr_3$ perovskite solar cells. *J. Mater. Chem. A* **2019**, *7*, 12635-12644.

(225) Haruta, Y.; Ikenoue, T.; Miyake, M.; Hirato, T. One-step coating of full-coverage $CsPbBr_3$ thin films via mist deposition for all-inorganic perovskite solar cells. *ACS Appl. Energy Mater.* **2020**, *3*, 11523-11528.

(226) Liao, G., Zhao, Y., Duan, J., Yuan, H., Wang, Y., Yang, X., He, B. and Tang, Q., Enhanced charge extraction with all-carbon electrodes for inorganic $CsPbBr_3$ perovskite solar cells. *Dalton Trans.* **2018**, *47*,15283-15287.

(227) Poli, I.; Hintermair, U.; Regue, M.; Kumar, S.; Sackville, E.V.; Baker, J.; Watson, T.M.; Eslava, S.; Cameron, P.J. Graphite-protected $CsPbBr_3$ perovskite photoanodes functionalised with water oxidation catalyst for oxygen evolution in water. *Nat. commun.* **2019**, *10*, 2097.